Instability in dynamic fracture — Source link

Jay Fineberg, Steven P. Gross, Michael Marder, Harry L. Swinney

Institutions: University of Texas at Austin

Topics: Fracture mechanics, Critical ionization velocity, Brittleness, Instability and Fracture (geology)

Related papers:

- Dynamic Fracture Mechanics

- Instability in the propagation of fast cracks

- Local crack branching as a mechanism for instability in dynamic fracture.

- Origin of crack tip instabilities

- Instability dynamics of fracture: A computer simulation investigation.

INSTABILITY IN DYNAMIC FRACTURE

J. FINEBERG[a]**, M. MARDER**[b]

[a]*The Racah Institute of Physics, The Hebrew University of Jerusalem Jerusalem, 91904, Israel*
[b]*Center for Nonlinear Dynamics and Department of Physics, The University of Texas at Austin, Austin TX 78712, USA*

Instability in dynamic fracture

J. Fineberg[a,*,1], M. Marder[b,2]

[a] *The Racah Institute of Physics, The Hebrew University of Jerusalem, Jerusalem 91904, Israel*
[b] *Center for Nonlinear Dynamics and Department of Physics, The University of Texas at Austin, Austin TX 78712, USA*

Contents

* Corresponding author.

[1] Supported by the US, Israel Binational Science Foundation, Grant 95-00029/1.

[2] Theoretical work supported by the National Science Foundation, DMR-9531187, the US, Israel Binational Science Foundation, Grant 95-00029//1, and the Exxon Education Foundation; experimental work supported by the Texas Advanced Research Program; supercomputing supported by the Texas Advanced Computation Center, and the National Partnership for Academic Computing Infrastructure.

Abstract

The fracture of brittle amorphous materials is an especially challenging problem, because the way a large object shatters is intimately tied to details of cohesion at microscopic scales. This subject has been plagued by conceptual puzzles, and to make matters worse, experiments seemed to contradict the most firmly established theories. In this review, we will show that the theory and experiments fit within a coherent picture where dynamic instabilities of a crack tip play a crucial role. To accomplish this task, we first summarize the central results of linear elastic dynamic fracture mechanics, an elegant and powerful description of crack motion from the continuum perspective. We point out that this theory is unable to make predictions without additional input, information that must come either from experiment, or from other types of theories. We then proceed to discuss some of the most important experimental observations, and the methods that were used to obtain the them. Once the flux of energy to a crack tip passes a critical value, the crack becomes unstable, and it propagates in increasingly complicated ways. As a result, the crack cannot travel as quickly as theory had supposed, fracture surfaces become rough, it begins to branch and radiate sound, and the energy cost for crack motion increases considerably. All these phenomena are perfectly consistent with the continuum theory, but are not described by it. Therefore, we close the review with an account of theoretical and numerical work that attempts to explain the instabilities. Currently, the experimental understanding of crack tip instabilities in brittle amorphous materials is fairly detailed. We also have a detailed theoretical understanding of crack tip instabilities in crystals, reproducing qualitatively many features of the experiments, while numerical work is beginning to make the missing connections between experiment and theory. © 1999 Elsevier Science B.V. All rights reserved.

1. Introduction

1.1. Brief overview of the paper

Fracture mechanics is one of the most heavily developed branches of engineering science and applied mathematics [1–9]. It emerged from mathematical exercises in the early part of the 20th century into a closely knit collection of theoretical concepts and experimental procedures that are now widely used to ensure the safety of critical structures, ranging from airplanes to the housings of microelectronic devices. Some practitioners of this field feel that its development is essentially finished. However, a group of physicists has recently begun to work in the area, and our number appears to be growing. The first task is therefore to explain the new developments that have created excitement in this mature area, and induced physicists to work on it after an absence, with few exceptions [10], of many decades.

There are two separate lines of inquiry pulling people into fracture of brittle materials. The first is a set of puzzles about the dynamics of cracks. It is often stated that cracks do not reach the terminal velocity predicted by theory, and that they have an unexplained instability at a critical velocity. We will show that these puzzles are real, but have been difficult to solve because they are not correctly stated. The real puzzle concerns energy dissipation at the crack tip, and the answer we will present is that when energy flux to a crack tip passes a certain critical value, efficient steady motion of the tip becomes unstable to the formation of microcracks that propagate away from the main crack. As it undergoes a hierarchy of instabilities, the ability of the crack tip to absorb energy is enormously increased. The second line of inquiry is the attempt to understand how things break from an atomic level. There is a broad consensus that this problem is best met by a direct attack from molecular dynamics simulations, watching cracks move one atom at a time. However, before moving to large computer simulations, we believe it is important to study analytical results so as to understand the qualitative effect of atomic discreteness upon crack motion. With these results in hand, many laboratory experimental results become comprehensible, the relation between simulations and laboratory experiments becomes clearer, and molecular dynamics simulations can be made much more efficient.

In fact, the puzzles in fracture dynamics, at both macroscopic and atomic scales, are manifestations of the same underlying phenomena. Our purpose in this review is to explain why the conventional puzzles have arisen, how to recast them, and how to explain them. We do not pretend to provide a general overview of fracture mechanics as a whole. For example, we focus upon brittle materials, and do not deal with ductile fracture [11], although dynamic elastic–plastic fracture is very well developed [7]. We will emphasize the dynamics of cracks once they start moving, rather than the most important engineering topic, which is the matter of reliably determining the point of initiation [9]. We are not challenging conventional fracture mechanics; all our findings must be compatible with it. Instead, we are answering some questions that conventional continuum fracture mechanics does not ask.

The basic structure of this paper is

- A summary of some of the principal features of dynamic fracture mechanics.
- An explanation of why dynamic fracture mechanics appears to fail, why it does not actually do so, and why dynamic fracture mechanics is incomplete without certain crucial information about the nature of the crack tip that must be provided by computations at scales too small for continuum mechanics to follow.

1.2. Scaling arguments

1.2.1. All objects are far from mechanical equilibrium

The world is farther from equilibrium than most of us realize. Consider a piece of rock, of area A and height h. According to equilibrium principles the rock should not be able to sustain its own weight under the force of gravity if it becomes tall enough. We begin with a simple estimate of what the critical height should be. The gravitational potential energy of the rock is $\rho A h^2 g/2$ where ρ is the density. By cutting the rock into two equal blocks of height $h/2$ and setting them side by side, this energy can be reduced to $\rho A h^2 g/4$, for an energy gain of $\rho A h^2 g/4$. The cost of the cut is the cost of creating new rock surface, which characteristically costs per unit area $G = 1\,\mathrm{J/m^2}$. Taking the density to be $\rho = 2000\,\mathrm{kg/m^3}$, the critical height at which it pays to divide the rock in two is

$$h = \sqrt{4G/\rho g} \sim 1.4\,\mathrm{cm} . \tag{1}$$

So every block of stone more than 2 cm tall is unstable under its own weight. A similar estimate applies to steel or concrete. Yeats' observation that "Things fall apart" is a statement about equilibrium which fortunately takes a long time to arrive.

1.2.2. The energy barrier seems immense, but this is experimentally wrong

If most objects are out of mechanical equilibrium, the next task is to estimate the size of the barriers holding them in place. An easy way to obtain a rough value is by imagining what happens to the atoms of a solid as one pulls it uniformly at two ends. At first, the forces between the atoms increase, but eventually they reach a maximum value, and the solid falls into pieces, as shown in Fig. 1. Interatomic forces vary greatly between different elements and compounds, but the forces typically reach their maximum value when the distance between atoms increases by around 20% of their original separation. The force needed to stretch a solid slightly is (Fig. 1)
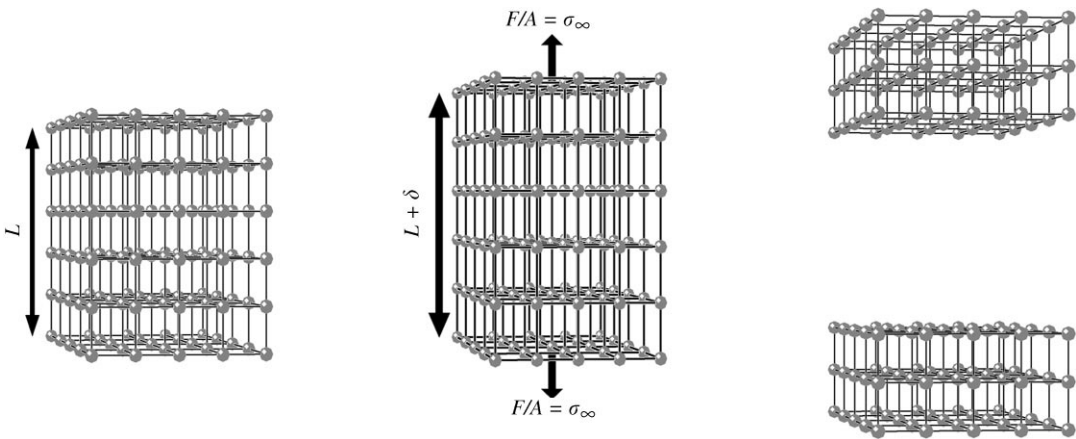
$$F = EA\delta/L , \tag{2}$$

Fig. 1. Mechanically stable configurations are often far from their lowest energy state. For example, a solid completely free of flaws would only pull apart when all bonds as long a plane snapped simultaneously, despite the fact that it would generally be energetically advantageous for the solid to be split.

Table 1
The experimental strength of a number of materials in polycrystalline or amorphous form, compared to their theoretical strength (from [12,13])

Material	Young's modulus (GPa)	Theoretical strength (GPa)	Practical strength (GPa)	Practical/theoretical strength
Iron	195–205	43–56	0.3	0.006
Copper	110–130	24–55	0.2	0.005
Titanium	110	31	0.3	0.009
Silicon	110–160	45	0.7	0.01
Glass	70	37	0.4	0.01
Plexiglas	3.6	3	0.05	0.01

where E is the material's Young's modulus, so the force per area needed to reach the breaking point is around

$$\sigma_\infty = F/A = E/5 . \tag{3}$$

As shown in Table 1, this estimate is in error by orders of magnitude. The problem does not lie in the crude estimates used to obtain the forces at which bonds separate, but in the conception of the calculation. The first scaling argument greatly underestimated the practical resistance of solid bodies to separation, while this one greatly overestimates it. The only way to uncover correct orders of magnitude is to account for the actual dynamical mode by which brittle solids fail, which is by the propagation of a crack.

1.2.3. Cracks provide the most efficient path to equilibrium

As we shall see in Section 2.3, the presence of a crack in an otherwise perfect material leads to a stress singularity at its tip. For an atomically sharp crack tip, a single crack a few microns long is sufficient to explain the large gaps between the theoretical and experimental material strengths as shown in Table 1. The theoretical strength of glass fibers, for example, can be approached by means of acid etching of the fiber surface. The etching process serves to remove any initial microscopic flaws along the glass surface. By removing its initial flaws, a 1 mm² glass fiber can lift a piano (but during the lifting process, we would not advise standing under the piano). The stress singularity that develops at the tip of a crack serves to focus the energy that is stored in the surrounding material and efficiently use it to break one bond after another. Thus, the continuous advance of the crack tip, or crack propagation, provides an efficient means to overcome the energy barrier between two equilibrium states of the system having different amounts of mechanical energy.

1.2.4. The scaling of dynamic fracture

The first analysis of rapid fracture was carried out by Mott [14], and then slightly improved by Dulaney and Brace [15]. It is a dimensional analysis which clarifies the basic physical processes, despite being wrong in many details, and consists of writing down an energy balance equation for crack motion.

Consider a crack of length $l(t)$ growing at rate $v(t)$ in a very large plate where a stress σ_∞ is applied at the far boundaries of the system, as shown in Fig. 2. When the crack extends, its faces separate, causing the plate to relax within a circular region centered on the middle of the crack and with
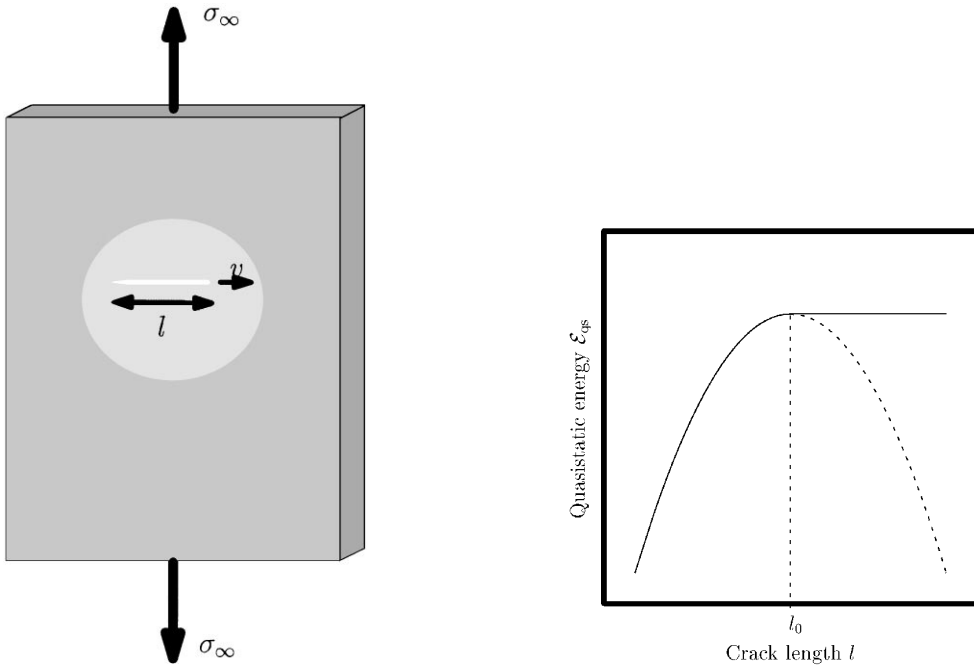
Fig. 2. As a crack of length l expands at velocity v in an infinite plate, it disturbs the surrounding medium up to a distance on the order of l.

Fig. 3. The energy of a plate with a crack as a function of its length. In the first part of its history, the crack grows quasi-statically, and its energy increases. At l_0 the crack begins to move rapidly, and energy is conserved.

diameter of order l. The kinetic energy involved in moving a region of this size is $Mv^2/2$, where M is the total mass, and v is a characteristic velocity. Since the mass of material that moves is proportional to l^2, the kinetic energy is guessed to be of the form

$$\text{KE} = C_K l^2 v^2 \ . \tag{4}$$

The region of material that moves is also the region from which elastic potential energy is being released as the crack opens. Therefore, the potential energy gained in releasing stress is guessed to be of the form

$$\text{PE} = -C_P l^2 \ . \tag{5}$$

These guesses are correct for slowly moving cracks, but fail qualitatively as the crack velocity approaches the speed of sound, in which case both kinetic and potential energies diverge. This divergence will be demonstrated later, but for the moment, let us proceed fearlessly. The final process contributing to the energy balance equation is the creation of new crack surfaces, which takes energy Γl. The *fracture energy* Γ accounts not only for the minimal energy needed to snap bonds, but also for any other dissipative processes that may be needed in order for the fracture to progress; it is often orders of magnitude greater than the thermodynamic surface energy. However,

for the moment, the only important fact is that creating new surface scales as the length l of the crack. So the total energy of the system containing a crack is given by

$$\mathcal{E} = C_K l^2 v^2 + \mathcal{E}_{qs}(l) , \tag{6}$$

with

$$\mathcal{E}_{qs}(l) = - C_P l^2 + \Gamma l . \tag{7}$$

Consider first the problem of quasi-static crack propagation. If a crack moves forward only slowly, its kinetic energy will be negligible, so only the quasi-static part of the energy, $\mathcal{E}_{qs}$, will be important. For cracks where l is sufficiently small, the linear cost of fracture energy is always greater than the quadratic gain of potential energy, and in fact such cracks would heal and travel backwards if it were not for irreversible processes, such as oxidation of the crack surface, which typically prevent it from happening. That the crack grows at all is due to additional irreversible processes, sometimes chemical attack on the crack tip, sometimes vibration or other irregular mechanical stress. It should be emphasized that the system energy $\mathcal{E}$ increases as a result of these processes. Eventually, at length l_0, the energy gained by relieving elastic stresses in the body exceeds the cost of creating new surface, and the crack becomes able to extend spontaneously. One sees that at l_0, the energy functional $\mathcal{E}_{qs}(l)$ has a quadratic maximum. The Griffith criterion for the onset of fracture is that fracture occurs when the potential energy released per unit crack extension equals the fracture energy, Γ. Thus fracture in this system will occur at the crack length l_0 where

$$d\mathcal{E}_{qs}/dl = 0 . \tag{8}$$

Using Eq. (7) we find that

$$l_0 = \Gamma/(2C_P) . \tag{9}$$

Eq. (7) now becomes

$$\mathcal{E}_{qs}(l) = \mathcal{E}_{qs}(l_0) - C_P(l - l_0)^2 . \tag{10}$$

This function is depicted in Fig. 3.

Much of engineering fracture mechanics boils down to calculating l_0, given things such as external stresses, which in the present case have all been condensed into the constant C_P. Dynamic fracture starts in the next instant, and because it is so rapid, the energy of the system is conserved, remaining at $\mathcal{E}_{qs}(l_0)$. Using Eqs. (6) and (10), with $\mathcal{E} = \mathcal{E}_{qs}(l_0)$ gives

$$v(t) = \frac{C_P}{C_K}\left(1 - \frac{l_0}{l}\right) = v_{max}\left(1 - \frac{l_0}{l}\right) . \tag{11}$$

This equation predicts that the crack will accelerate until it approaches the speed v_{max}. The maximum speed cannot be deduced from these arguments, but Stroh [16] correctly argued that v_{max} should be the Rayleigh wave speed, the speed at which sound travels over a free surface. A crack is a particularly severe distortion of a free surface, but assuming that it is legitimate to represent a crack in this way, the Rayleigh wave speed is the limiting speed to expect. This result was implicit in the calculations of Yoffe [17].

In this system, one needs only to know the length at which a crack begins to propagate in order to predict all the following dynamics. As we will see presently, Eq. (11) comes astonishingly close to

anticipating the results of a sophisticated mathematical analysis developed over 15 years. This result is especially puzzling since the forms (4) and (5) for the kinetic and potential energy are incorrect; these energies should actually diverge as the crack begins to approach the Rayleigh wave speed. The reason that the dimensional analysis succeeds anyway is that to find the crack velocity one takes the ratio of kinetic and potential energy; their divergences are of exactly the same form, and cancel out.

2. Continuum fracture mechanics

In this section we will attempt to review briefly the background, basic formalism and underlying assumptions that form the body of continuum fracture mechanics. We will first schematically describe the general "game plan" pursued within fracture mechanics. The following subsections will introduce the main "players" or concepts on which the current continuum description of dynamic fracture is based. As the work described in this review mainly deals with the dynamics of a crack in thin plates or quasi-2D media, we will first discuss the reduction of linear elasticity to two dimensions. Some basic concepts common to both static and dynamic cracks will then be discussed. These will include the creation of a singular stress field at the tip of a static crack together with criteria for the onset and growth of a moving crack. We then turn to a description of moving cracks. We will first describe the formalism used to describe a crack moving at a given velocity and, using this formalism, look at the dependence of the near tip stress fields as a function of the crack's velocity. The stage will then be set for a description of the general formalism used to determine an equation of motion for a moving crack in an infinite medium. The central result of dynamics fracture mechanics, which is obtained by equating the (velocity dependent) elastic energy flowing into the tip of a moving crack with the dissipative mechanisms absorbing it, will be described. This result provides an equation of motion for a crack moving along a straight-line trajectory. We then discuss criteria for determination of a crack's path and conclude the section by discussing a number of points that the theory cannot address.

2.1. Structure of fracture mechanics

The structure of fracture mechanics follows the basic ideas used in the scaling arguments described in the previous section. The general strategy is to solve for the displacement fields in the medium subject to both the boundary conditions and the externally applied stresses. The elastic energy transported by these fields is then matched to the amount of energy dissipated throughout the system, and an equation of motion is obtained. For a single moving crack, as in the scaling argument above, the only energy sink existing in the system is at the tip of the crack itself. Thus, an equation of motion can be obtained for a moving crack if one possesses detailed knowledge of the dissipative mechanisms in the vicinity of the tip.

2.1.1. Dissipation and the process zone

Unfortunately, the processes that lead to dissipation in the tip vicinity are far from simple. Depending on the type of material, there is a large number of complex dissipative processes ranging from dislocation formation and emission in crystalline materials to the complex unraveling and

fracture of intertangled polymer strands in amorphous polymers. At first glance, the many different (and in many cases, poorly understood) dissipative processes that are observed would appear to preclude a universal description of fracture. A way around this problem was proposed by Irwin and Orowan [18,19].

Fracture, together with the complex dissipative processes occurring in the vicinity of the tip, occurs due to intense values of the stress field that occur as one approaches the tip. As we will show shortly, if the material surrounding the tip were to remain linearly elastic until fracture, a *singularity* of the stress field would result at the mathematical point associated with the crack tip. Since a real material cannot support singular stresses, in this vicinity the assumption of linearly elastic behavior must break down and material dependent, dissipative processes must come into play. Irwin and Orowan independently proposed that the medium around the crack tip be divided into three separate regions as follows (Fig. 4).

- *The process zone*: In the region immediately surrounding the crack tip, called the process zone (or cohesive zone), all of the nonlinear dissipative processes that ultimately allow a crack to move forward, are assumed to occur. Fracture mechanics avoids any sort of detailed description of this zone, and simply posits that it will consume some energy Γ per unit area of crack extension. The size of the process zone is material dependent, ranging from nanometers in glass to microns in brittle polymers. The typical size of the process zone can be estimated by using the radius at which an assumed linear elastic stress field surrounding the crack tip would equal the yield stress of the material.
- *The universal elastic region*: Everywhere outside of the process zone the response of the material can be described by continuum linear elasticity. In the vicinity of the tip, but outside of the process zone, the stress and strain fields adopt universal singular forms which solely depend on the symmetry of the externally applied loads. In two dimensions the singular fields surrounding the process zone are entirely described by three constants, called stress intensity factors. The stress intensity factors incorporate all of the information regarding the loading of the material and are related, as we shall see, to the energy flux into the process zone. The larger the overall size of the body in which the crack lives, the larger this region becomes. In rough terms, for given values of the stress intensity factors, the size of this universal elastic region scales as $\sqrt{L}$, where L is the macroscopic scale on which forces are applied to the body. Thus the assumptions of fracture mechanics become progressively better as samples become larger and larger.
- *Outer elastic region*: Far from the crack tip, stresses and strains are described by linear elasticity. There is nothing more general to relate; details of the solution in this region depend upon the locations and strengths of the loads, and the shape of the body. In special cases, analytical solutions are available, while in general one can resort to numerical solution. At first glance, the precise linear problem that must be solved might seem inordinately complex. How can one avoid needing explicit knowledge of complicated boundary conditions on some complicated loop running outside the outer rim of the process zone? The answer is that so far as linear elasticity is concerned, viewed on macroscopic scales the process zone shrinks to a point at the crack tip, and the crack becomes a branch cut. Replacing the complicated domain in which linear elasticity actually holds with an approximate one that needs no detailed knowledge of the process zone is another approximation that becomes increasingly accurate as the dimensions of the sample, hence the size of the universal elastic region, increase. The assumption that the process zone
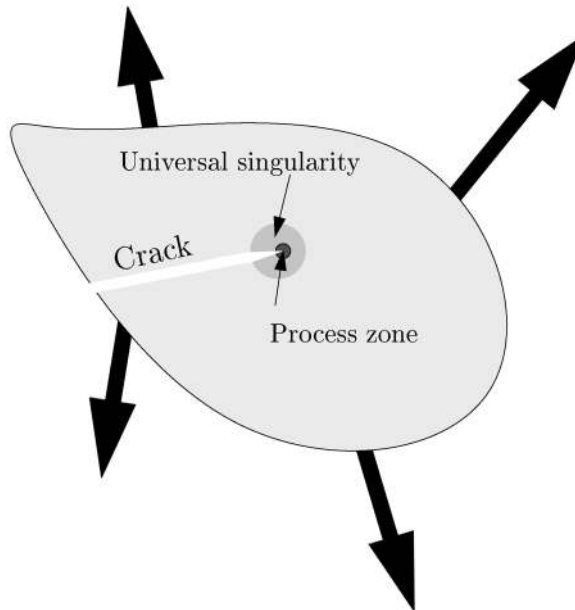
Fig. 4. Structure of fracture mechanics. The crack tip is surrounded by a region in which the physics is unknown. Outside this process zone is a region in which elastic solutions adopt a universal form.

in a material is encompassed within the universal elastic region is sometimes called the assumption of *small-scale yielding*.

The dissipative processes within the process zone determine the *fracture energy*, Γ, defined as the amount of energy required to form a unit area of fracture surface. In the simplest case, where no dissipative processes other than the direct breaking of bonds take place, Γ is a constant, depending on the bond energy. In the general case, Γ may well be a complicated function of both the crack velocity and history and differ by orders of magnitude from the *surface energy* defined as the amount of energy required to sever a unit area of atomic bonds. No general first principles description of the process zone exists, although numerous models have been proposed (see e.g. [20]).

2.1.2. Conventional fracture modes

It is conventional to focus upon three symmetrical ways of loading a solid body with a crack. These are known as *modes*, and are illustrated in Fig. 5. A generic loading situation produced by some combination of forces without any particular symmetry is referred to as *mixed mode* fracture. Understanding mixed-mode fracture is obviously of practical importance, but since our focus will be upon the physics of crack propagation rather than upon engineering applications, we will restrict attention to the special cases in which the loading has a high degree of symmetry.

The fracture mode that we will mainly deal with in this review is Mode I, where the crack faces, under tension, are displaced in a direction normal to the fracture plane. In Mode II, the motion
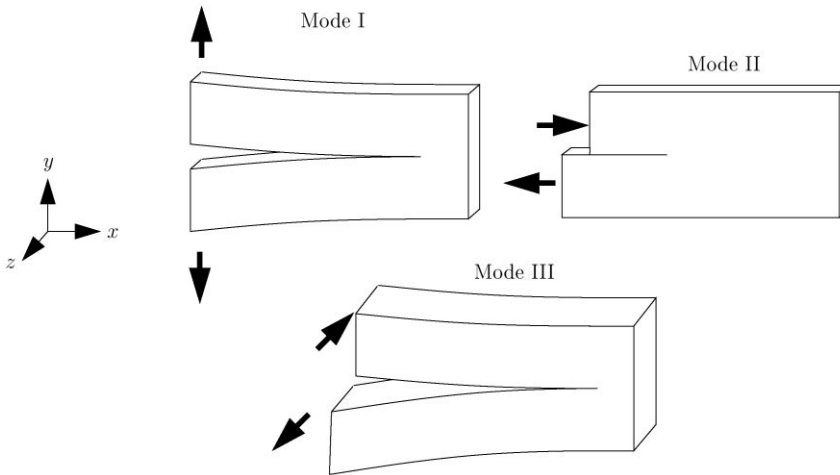
Fig. 5. Illustration of the three conventional fracture modes, which are characterized by the symmetry of the applied forces about the crack plane.

of the crack faces is that of shear along the fracture plane. Mode III fracture corresponds to an out of plane tearing motion where the direction of the stresses at the crack faces is normal to the plane of the sample. One experimental difficulty of Modes II and III is that the crack faces are not pulled away from one another. It is unavoidable that contact along the crack faces will occur. The resultant friction between the crack faces contributes to the forces acting on the crack, but is difficult to measure precisely.

For these reasons, of the three fracture modes, Mode I corresponds most closely to the conditions used in most experimental and much theoretical work. In two-dimensional isotropic materials, Mode II fracture cannot easily be observed, since slowly propagating cracks spontaneously orient themselves so as to make the Mode II component of the loading vanish near the crack tip [21], as we will discuss in Section 2.9. Mode II fracture is however observed in cases where material is strongly anisotropic. Both friction and earthquakes along a predefined fault are examples of Mode II fracture where the binding across the fracture interface is considerably weaker than the strength of the material that comprises the bulk material. Pure Mode III fracture, although experimentally difficult to achieve, is sometimes used as a model system for theoretical study since, in this case, the equations of elasticity simplify considerably. Analytical solutions, obtained in this mode, have provided considerable insight to the fracture process.

2.1.3. Universal singularities near the crack tip

As one approaches the tip of a crack in a linearly elastic material, the stress field surrounding the tip develops a square root singularity. As first noted by Irwin [22], the stress field at a point (r, θ) near the crack tip, measured in polar coordinates with the crack line corresponding to $\theta = 0$, takes the form

$$\sigma_{i,j} = K_\alpha (1/\sqrt{2\pi r}) f_{i,j}^\alpha (v, \theta) , \tag{12}$$

where v is the instantaneous crack velocity, and α is an index running through Modes I–III. For each of these three symmetrical loading configurations, $f_{i,j}^{\alpha}(v,\theta)$ in Eq. (12) is a known universal function. The coefficient, K_{α}, called the *stress intensity factor*, contains *all* of the detailed information regarding sample loading and history. K_{α} will, of course, be determined by the elastic fields that are set up throughout the medium, but the stress that locally drives the crack is that which is present at its tip. Thus, this single quantity will entirely determine the behavior of a crack, and much of the study of fracture comes down to either the calculation or measurement of this quantity. One of the main precepts of fracture mechanics in brittle materials is that the stress intensity factor provides a universal description of the fracture process. In other words, no matter what the history or the external conditions in a given system, if the stress intensity factor in any two systems has the same value, the crack tip that they describe will behave in the same way. The universal form of the stress intensity factor allows a complete description of the behavior of the tip of a crack where one need only carry out the analysis of a given problem within the universal elastic region (see Section 2.1.1).

For arbitrary loading configurations, the stress field around the crack tip is given by three stress intensity factors, K_{α}, which lead to a stress field that is a linear combination of the pure Modes:

$$\sigma_{i,j} = \sum_{\alpha=1}^{3} K_{\alpha} \frac{1}{\sqrt{2\pi r}} f_{i,j}^{\alpha}(v,\theta) . \tag{13}$$

2.1.4. The relation of the stress intensity factor to energy flux

How are the stress intensity factors related to the flow of energy into the crack tip? Since one may view a crack as a means of dissipating built-up energy in a material, the amount of energy flowing into its tip must influence its behavior. Irwin [23] showed that the stress intensity factor is related to the energy release rate, G, which is defined as the quantity of energy flowing into the crack tip per unit fracture surface formed. The relation between the two quantities has the form

$$G = \sum_{\alpha=1}^{3} \frac{1 - v^2}{E} A_{\alpha}(v) K_{\alpha}^2 , \tag{14}$$

where v is the Poisson ratio of the material and the three functions $A_{\alpha}(v)$ depend only upon the crack velocity v. This relation between the stress intensity factor and the fracture energy is accurate whenever the stress field near the tip of a crack can be accurately described by Eq. (12). The near-field approximation of the stress fields surrounding the crack tip embodied in Eq. (13) becomes increasingly more accurate as the dimensions of the sample increase.

2.2. Linear elasticity

2.2.1. Reductions to two dimensions

Most of the theoretical work that we will describe in this review is performed in 2-D (or quasi-2-D) systems. In this subsection we will perform a reduction of the full 3-D elastic description of a crack to two dimensions in three important cases; for Mode III fracture and Mode I fracture in very thin and very thick plates. The first case, Mode III fracture, is an important model system where much analytic work can be performed with the corresponding gain in intuition of qualitative

features in fracture. The second case, Mode I fracture of a thick plate, describes stress and strain conditions of importance in describing fracture in the immediate vicinity of the crack tip. The third case, Mode I fracture in thin plates, corresponds to much of the experimental work that we will describe.

Our starting point is the equation of motion for an isotropic elastic body in the continuum limit,

$$\rho\, \partial^2\boldsymbol{u}/\partial t^2 = (\lambda + \mu)\nabla(\nabla\cdot\boldsymbol{u}) + \mu\nabla^2\boldsymbol{u}\ , \tag{15}$$

originally found by Navier. Here $\boldsymbol{u}$ is a field describing the displacement of each mass point from its original location in an unstrained body and ρ is the density. The constants μ and λ are called the Lamé constants, have dimensions of energy per volume, and are typically of order $10^{10}\, \mathrm{erg/cm^3}$. We define the linear elastic strain tensor [24]

$$\varepsilon_{ij} = \frac{1}{2}\left(\frac{\partial u_i}{\partial x_j} + \frac{\partial u_j}{\partial x_i}\right)\ . \tag{16}$$

When a linear stress–strain relation exists in a homogeneous isotropic medium, the stress tensor, σ_{ij}, is defined by

$$\sigma_{ij} = \lambda\delta_{ij}\sum_k \varepsilon_{kk} + 2\mu\varepsilon_{ij}\ . \tag{17}$$

2.2.2. Mode III

The simplest analytical results are for pure Mode III, illustrated in Fig. 5. The only non-zero displacement is u_z, and it is a function of x and y alone. The only non-vanishing stresses in this case are

$$\sigma_{xz} = \mu\, \partial u_z/\partial x \tag{18}$$

and

$$\sigma_{yz} = \mu\, \partial u_z/\partial y\ . \tag{19}$$

The equation of motion for u_z is

$$\frac{1}{c^2}\frac{\partial^2 u_z}{\partial t^2} = \nabla^2 u_z\ , \tag{20}$$

where

$$c = \sqrt{\mu/\rho}\ . \tag{21}$$

Therefore, the vertical displacement u_z obeys the ordinary wave equation.

2.2.3. Mode I: plane strain

Consider a sample that is extremely thick along z (see Fig. 5), and where all applied forces are uniform in the z direction. Since all derivatives with respect to z vanish, all fields can be viewed as functions of x and y alone. This situation is called plane strain. The reduction to two dimensions is quite simple, but this geometry is rarely convenient for experiments.

2.2.4. Mode I: plane stress

A third case in which the equations of elasticity reduce to two dimensions corresponds to pulling on a thin plate in Mode I, and is called plane stress. If the scale over which stresses are varying in x and y is large compared with the thickness of the plate along z, then one might expect that the displacements in the z direction will come quickly into equilibrium with the local x and y stresses. When the material is being stretched, (think of pulling on a balloon), the plate will contract in the z direction, and when it is being compressed, the plate will thicken. Therefore, one guesses that

$$u_z = zf(u_x, u_y) \,, \tag{22}$$

and that u_x, and u_y are independent of z. One can deduce the function f by noticing that σ_{zz} must vanish on the face of the plate. This means that

$$\lambda \left\{ \frac{\partial u_x}{\partial x} + \frac{\partial u_y}{\partial y} \right\} + (\lambda + 2\mu) \frac{\partial u_z}{\partial z} = 0 \tag{23}$$

at the surface of the plate, which implies that

$$f(u_x, u_y) = \frac{\partial u_z}{\partial z} = -\frac{\lambda}{\lambda + 2\mu} \left\{ \frac{\partial u_x}{\partial x} + \frac{\partial u_y}{\partial y} \right\} . \tag{24}$$

So

$$\frac{\partial u_x}{\partial x} + \frac{\partial u_y}{\partial y} + \frac{\partial u_z}{\partial z} = \frac{2\mu}{\lambda + 2\mu} \left\{ \frac{\partial u_x}{\partial x} + \frac{\partial u_y}{\partial y} \right\} , \tag{25}$$

and one can write

$$\sigma_{\alpha\beta} = \tilde{\lambda} \delta_{\alpha\beta} \frac{\partial u_\gamma}{\partial x_\gamma} + \mu \left(\frac{\partial u_\alpha}{\partial x_\beta} + \frac{\partial u_\beta}{\partial x_\alpha} \right) , \tag{26}$$

where

$$\tilde{\lambda} = 2\mu\lambda/(\lambda + 2\mu) \,, \tag{27}$$

and α and β now range only over x and y. Therefore, a thin plate obeys the equations of two-dimensional elasticity, with an effective constant $\tilde{\lambda}$, so long as u_z is dependent upon u_x and u_y according to Eq. (24). In the following discussion, the tilde over $\tilde{\lambda}$ will usually be dropped, with the understanding that the relation to three-dimensional materials properties is given by Eq. (26). The equation of motion is still Navier's equation, Eq. (15), but restricted to two dimensions.

A few random useful facts: materials are frequently described by the Young's modulus E and Poisson ratio v. In terms of these constants,

$$\lambda = \frac{Ev}{(1 + v)(1 - 2v)} \,, \quad \tilde{\lambda} = \frac{E}{2(1 - v^2)} \,, \quad \mu = \frac{E}{2(1 + v)} \,. \tag{28}$$

The following relation will be useful in discussing two-dimensional static problems. First note that

$$\boldsymbol{V} \cdot \boldsymbol{u} = \Sigma_\alpha (\lambda + 2\mu) \sigma_{\alpha\alpha} \,. \tag{29}$$

Second, taking the divergence of Eq. (15), one finds that

$$\frac{\rho}{\lambda + 2\mu} \frac{\partial^2 \sigma_{\alpha\alpha}}{\partial t^2} = \nabla^2 \sigma_{\alpha\alpha} . \tag{30}$$

Therefore, $\nabla \cdot \boldsymbol{u}$ obeys the wave equation, with the longitudinal wave speed

$$c_l = (\lambda + 2\mu)/\rho . \tag{31}$$

Similarly, $\nabla \times \boldsymbol{u}$ also obeys the wave equation, but with the shear wave speed

$$c_{\mathrm{t}} = \sqrt{\mu/\rho} . \tag{32}$$

2.2.5. The transition from 2D to 3D

Near the tip of a crack in a plate, stresses become severe enough that the approximations leading to two-dimensional plane stress elasticity fail. Nakamura and Parks [25] have discussed the way this happens; if the thickness of the plate along z is denoted by d, then at distances from the crack tip much larger than d all fields are described by equations of plane stress. At distances from the crack tip much less than d, and away from the x–y surfaces of the plate, the fields solve the equations of plane strain.

2.3. The Inglis solution for a static crack in Mode III

Why do cracks have a profound effect on the strength of materials? As we observed in Table 1, a huge discrepancy exists between the practical and theoretical strengths of materials. The reason for the discrepancy has been understood since the first decades of this century. If one takes a plate, puts an elliptical hole in it, and pulls, then as first found by Inglis in 1913, the stresses at the narrow ends of the hole are much larger than those exerted off at infinity, as shown in Fig. 6. We see then that a crack acts as an "amplifier" of stresses, thereby causing elastic energy to be preferentially focused into its tip. Thus, the existence of a crack will lead to a large decrease in the effective strength of a material.

The ratio of maximum to applied stress is

$$\frac{\text{Maximum Stress}}{\text{Applied Stress}} = 2\frac{l}{\rho} , \tag{33}$$

where l is the length of the crack and ρ the radius of curvature at its tip. This means that if one assumes that typical solids have cracks with tips of size 1 Å, and of length 10^4Å, then one can account for the discrepancies in Table 1. We will now derive Eq. (33).

Solving even the static equations of linear elasticity is frequently a complicated and difficult affair. To simplify matters as much as possible, assume that the stresses applied to the plate coincide to the conditions of anti-plane shear stress, as shown in Fig. 5, so the only nonzero displacement is u_z. Returning to Eq. (20), one sees that the static equation of linear elasticity is now simply
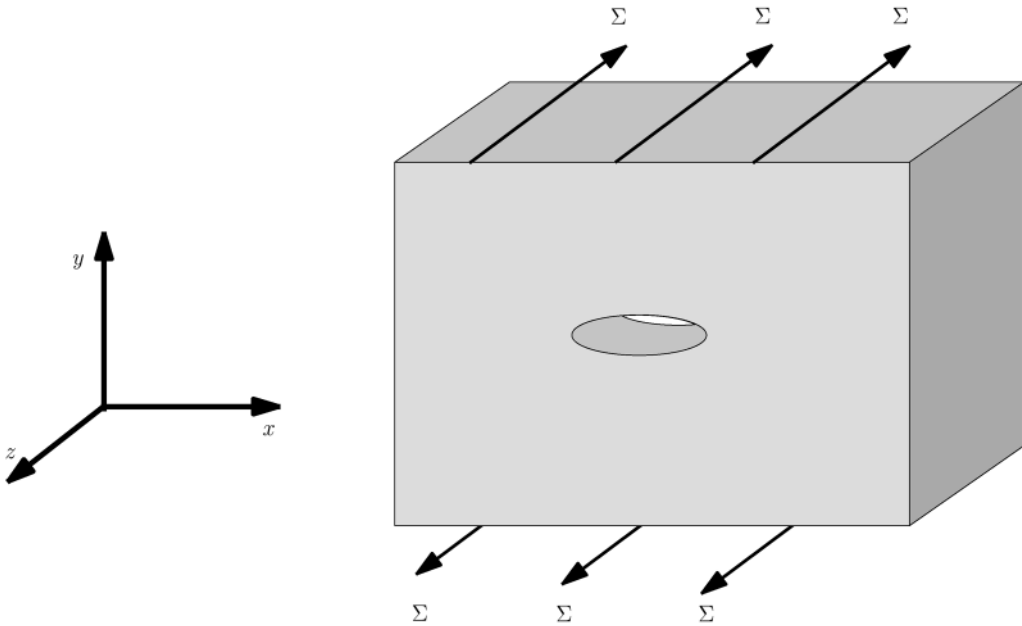
$$\nabla^2 u_z = 0 . \tag{34}$$

Fig. 6. The stresses at the tips of an elliptical hole in a solid are much greater than those applied off at infinity.

Eq. (34) is Laplace's equation, so the whole theory of complex variables can be brought to bear in order to find solutions. For the boundary problem at hand, conformal mapping is the appropriate technique. Since u_z is a solution of Laplace's equation, it can be represented by

$$u_z = \tfrac{1}{2}(\phi(\zeta) + \overline{\phi(\zeta)}) , \tag{35}$$

where ϕ is analytic, and $\zeta = x + iy$.

One can easily write down the asymptotic behavior of ϕ. Far from the hole, the displacement $u_z(x,y)$ just increases linearly with y, so

$$\phi = -i\Sigma\zeta . \tag{36}$$

In Eq. (36), the constant Σ is dimensionless, but one can think of it measuring the stress in units of the Lamé constant μ.

How does the presence of the hole affect the stress field? Because the edges of the hole are free, the stress normal to the edge must vanish. If s is a variable which parameterizes the edge of the hole, so that

$$[x(s),y(s)] \tag{37}$$

travels around the boundary of the hole as s moves along the real axis, then requiring the normal stress to vanish means that

$$\frac{\partial u_z}{\partial y}\frac{\partial x}{\partial s} - \frac{\partial u_z}{\partial x}\frac{\partial y}{\partial s} = 0 \tag{38}$$

Using the representation of u_z in Eq. (35), one finds that

$$\partial\phi/\partial s = \partial\bar\phi/\partial s \tag{39}$$

on the boundary, or since ϕ is arbitrary up to a constant,

$$\phi(\zeta) = \overline{\phi(\zeta)} \tag{40}$$

when ζ lies on the boundary.

To illustrate the use of Eq. (40), let us define ω such that

$$\zeta = l/2(\omega + m/\omega) , \tag{41}$$

When ω lies on the unit circle, in other words

$$\omega = e^{i\theta} , \tag{42}$$

with θ real, ζ traces out an elliptical boundary. When $m = 0$, the boundary is a circle of radius $l/2$, and when $m = 1$, the boundary is a cut along the real axis extending from $-l$ to $+l$. Considering ϕ as a function of ω, one has

$$\phi(\omega) = \overline{\phi(\omega)} = \bar\phi(1/\omega) , \tag{43}$$

since $\bar\omega = 1/\omega$ on the unit circle. Eq. (43) can now be analytically continued off the unit circle. Outside of the hole ϕ must be completely regular, except for the fact that it diverges as $-i\Sigma\zeta$ for large ζ. But when ζ is large, $\omega \approx \zeta$, so from Eq. (41),

$$\phi \sim -i\Sigma\omega \quad \text{as } \omega \to \infty . \tag{44}$$

Consulting Eq. (43) one is forced to conclude that

$$\bar\phi(1/\omega) \sim -i\Sigma\omega , \tag{45}$$

which means that

$$\bar\phi(\omega) \sim -i\Sigma/\omega \quad \text{as } \omega \to 0 \tag{46}$$

but has no other singularities within the unit circle.

Having determined all the possible singularities of ϕ, it is determined up to a constant. It must be given by

$$\phi(\omega) = -i\Sigma\omega + i\Sigma/\omega \tag{47}$$

and, substituting Eq. (41), we have

$$\phi(\zeta) = -i\Sigma\frac{\zeta}{l}(1 + 1 - ml^2/\zeta^2) + i\Sigma\frac{\zeta}{lm}(1 - 1 - ml^2/\zeta^2) . \tag{48}$$

The case in which $m \to 1$ is particularly interesting. The hole becomes a straight crack along $[-l,l]$. Notice that ϕ has a branch cut over exactly the same region. The displacement u_z is finite approaching the tip of the crack, but the stress

$$\sigma_{yz} = \mu \, \partial u_z/\partial y \sim 1/\sqrt{z - l} \quad \text{as } z \to l , \tag{49}$$

diverges as one approaches the tip of the crack.

2.3.1. Remarks about the singularity

Although this calculation concerns a particular case, the existence of a square root stress singularity at the tip of a crack is of general validity, in accord with Eq. (12). Giving a crack a finite radius of curvature is one way to cut off this singularity. A useful application of this idea is, for example, a common mechanic's trick to arrest the advance of a crack in a damaged engine block. To arrest the crack, the mechanic will drill a small hole at its tip. It may seem counter-intuitive at first to "fix" a hole by making a larger one, but by increasing the radius of curvature at the tip, the mechanic, in effect, is canceling the singularity in the stress field and thus considerably strengthening the engine block.

2.3.2. Static cracks in Mode I

The method of conformal mapping we described for Mode III cracks has been extended to Mode I by Muskhelishvili [26]. Matters are somewhat more complicated, since one must solve the biharmonic equation rather than Laplace's equation, and solve for two complex functions not one. Muskhelishvili alone solved enough problems with these techniques to fill several hundred pages, and hundreds of publications have since been devoted to solutions of fracture problems using these methods.

2.4. Linear elastic equations for moving solutions in Mode I fracture

Eq. (49) shows that in an elastic medium where uniform stress is applied at the boundaries, the stress field at the tip of a static crack becomes singular. We now turn to the case of a moving crack and examine the structure of the stress field at the tip of a moving Mode I crack. So as to be able to compare eventually with experiment, and because this review focuses upon crack dynamics, we carry out the analysis in the complicated case of Mode I loading.

The first step is to develop the general form of the stress and displacement fields for a moving crack. Begin with the dynamical equation for the strain field $\boldsymbol{u}$ of a steady state in a frame moving with a constant velocity v in the x direction,

$$(\lambda + \mu)\nabla(\nabla\cdot\boldsymbol{u}) + \mu\nabla^2\boldsymbol{u} = \rho v^2\,\partial^2\boldsymbol{u}/\partial x^2 \ . \tag{50}$$

Divide $\boldsymbol{u}$ into transverse and longitudinal parts so that

$$\boldsymbol{u} = \boldsymbol{u}_{\mathrm{t}} + \boldsymbol{u}_{\ell} \ , \tag{51}$$

with

$$\boldsymbol{u}_{\ell} = \nabla v_{\ell} \quad \text{and} \quad \boldsymbol{u}_{\mathrm{t}} = \left(\frac{\partial v_{\mathrm{t}}}{\partial y}, -\frac{\partial v_{\mathrm{t}}}{\partial x}\right) \ . \tag{52}$$

It follows immediately that

$$\left[(\lambda + 2\mu)\nabla^2 - \rho v^2\frac{\partial^2}{\partial x^2}\right]\boldsymbol{u}_{\ell} = -\left[\mu\nabla^2 - \rho v^2\frac{\partial^2}{\partial x^2}\right]\boldsymbol{u}_{\mathrm{t}} \equiv \boldsymbol{f}(x,y) \ . \tag{53}$$

In the end, it will be possible to set $\mathbf{f}$ to zero, but some intermediate steps are needed to see why this is legitimate. Acting on the left-hand side of Eq. (53) with the operator $[\partial/\partial y, -\partial/\partial x]$ gives zero,

while acting on u_t with $[\partial/\partial x, \partial/\partial y]$ also gives zero. Therefore

$$\frac{\partial f_y}{\partial x} - \frac{\partial f_x}{\partial y} = 0 \,, \tag{54a}$$

$$\frac{\partial f_x}{\partial y} + \frac{\partial f_y}{\partial x} = 0 \,, \tag{54b}$$

meaning that $\boldsymbol{f}$ obeys Cauchy's equations, and $f_x - if_y$ is an analytic function of $x + iy$. We then have

$$\left[\alpha^2 \frac{\partial^2}{\partial x^2} + \frac{\partial^2}{\partial y^2} \right] \nabla^2 v_\ell = 0 \,, \tag{55}$$

$$\left[\beta^2 \frac{\partial^2}{\partial x^2} + \frac{\partial^2}{\partial y^2} \right] \nabla^2 v_t = 0 \,, \tag{56}$$

where

$$\alpha^2 = 1 - \frac{\rho v^2}{\lambda + 2\mu} = 1 - \frac{v^2}{c_\ell^2} \,, \tag{57a}$$

$$\beta^2 = 1 - \frac{\rho v^2}{\mu} = 1 - \frac{v^2}{c_t^2} \,. \tag{57b}$$

Therefore, the general form of the potentials is

$$v_\ell = v_\ell^0(z) + \overline{v_\ell^0(z)} + v_\ell^1(x + i\alpha y) + \overline{v_\ell^1(x + i\alpha y)} \tag{58}$$

$$v_t = v_t^0(z) + \overline{v_t^0(z)} + v_t^1(x + i\beta y) + \overline{v_t^1(x + i\beta y)} \,, \tag{59}$$

subject to the constraint of Eq. (53), which gives a relation between v_ℓ^0 and v_t^0.

In fact, the purely harmonic pieces v_ℓ^0 and v_t^0 disappear entirely from expression (51) for $\boldsymbol{u}$. They result from the freedom one has to add a harmonic function to v_ℓ and v_t simultaneously, and can be neglected; $\boldsymbol{f}$ could have been set to zero from the beginning. Defining $\phi(z) = \partial v_\ell^1(z)/\partial z$ and $\psi(z) = \partial v_t^1(z)/\partial z$ we have for $\boldsymbol{u}$,

$$u_x = \phi(z_\alpha) + \overline{\phi(z_\alpha)} + i\beta[\psi(z_\beta) - \overline{\psi(z_\beta)}] \,, \tag{60a}$$

$$u_y = i\alpha[\phi(z_\alpha) - \overline{\phi(z_\alpha)}] - [\psi(z_\beta) + \overline{\psi(z_\beta)}] \,, \tag{60b}$$

where

$$z_\alpha = x + i\alpha y, \quad z_\beta = x + i\beta y \,. \tag{61}$$

Eq. (60) gives a general form for elastic problems which are in steady state moving at velocity v. Define also $\Phi = \partial \phi(z)/\partial z$ and $\Psi = \partial \psi(z)/\partial z$. Then the stresses are given by

$$\sigma_{xx} + \sigma_{yy} = 2(\lambda + \mu)[\Phi(z_\alpha) + \overline{\Phi(z_\alpha)}](1 - \alpha^2) \,, \tag{62a}$$

$$\sigma_{xx} - \sigma_{yy} = 2\mu\{(1 + \alpha^2)[\Phi(z_\alpha) + \overline{\Phi(z_\alpha)}] + 2i\beta[\Psi(z_\beta) - \overline{\Psi(z_\beta)}]\} \,, \tag{62b}$$

$$2\sigma_{xy} = 2\mu\{2i\alpha[\Phi(z_\alpha) - \overline{\Phi(z_\alpha)}] - (\beta^2 + 1)[\Psi(z_\beta) + \overline{\Psi(z_\beta)}]\} \,. \tag{62c}$$

It is worth writing down the stresses directly as well:

$$\sigma_{yy} = -\mu(1 + \beta^2)[\Phi(z_\alpha) + \overline{\Phi(z_\alpha)}] - 2i\beta\mu[\Psi(z_\beta) - \overline{\Psi(z_\beta)}] , \tag{62d}$$

$$\sigma_{xx} = \mu(1 + 2\alpha^2 - \beta^2)[\Phi(z_\alpha) + \overline{\Phi(z_\alpha)}] + 2i\beta\mu[\Psi(z_\beta) - \overline{\Psi(z_\beta)}] . \tag{62e}$$

The definitions of α and β in Eq. (57) have been used to simplify the expressions.

To solve a general problem, one has to find the functions ϕ and ψ which match boundary conditions. It is interesting to notice that when $v \to 0$, the right-hand side of Eq. (62a) goes to zero as well. Since one will be finding the potentials from given stresses at the boundaries, Φ must diverge as $1/v$, and the right-hand side of Eq. (62) will turn into a derivative of Φ with respect to α. The static theory has, therefore, a different structure than the dynamic theory, although the dynamic theory is, in fact, more straightforward.

2.5. Mode I, structure near the tip, stress intensity factors

As a first application of Eqs. (60)–(62), we will find the form of the stresses around the tip of a crack moving under Mode I loading. Assume the crack to lie along the negative x-axis, terminating at $x = 0$, and moving forward. The problem is assumed symmetric under reflection about the x-axis, but no other assumption is needed.

We know that in the static case, the stress fields have a square root singularity at the crack tip. We will assume the same to be true in the dynamic case also (The assumption is verified in all cases that can be worked explicitly.). Near the crack tip, we assume that

$$\phi(z) \sim (B_r + iB_i)z^{1/2} , \tag{63}$$

$$\psi(z) \sim (D_r + iD_i)z^{1/2} . \tag{64}$$

We first appeal to symmetry. Since the crack is loaded in Mode I, the displacements obey

$$u_x(-y) = u_x(y), \qquad u_y(-y) = -u(y) . \tag{65}$$

Placing Eq. (64) into Eq. (60) and using Eq. (65), we find immediately that $B_i = D_r = 0$. Thus

$$\Phi(z) \sim B_r/z^{1/2}, \quad \Psi(z) \sim iD_i/z^{1/2} . \tag{66}$$

We also observe that the square roots in Eq. (64) must be interpreted as having their cuts along the negative x-axis, corresponding to the crack. On the crack surface the stresses are relaxed. We thereby have two boundary conditions which require that σ_{xy} and σ_{yy} vanish on the surface of a crack. Upon substituting Eq. (66) into Eq. (62) we find that the condition upon σ_{yy} is satisfied identically for $x < 0$, $y = 0$. However, substituting into Eq. (62d) with $y = 0$ we find that

$$\sigma_{xy} = \mu i\{2\alpha B_r - (\beta^2 + 1)D_i\}\{1/\sqrt{x} - \overline{1/\sqrt{x}}\} . \tag{67}$$

Thus

$$D_i/B_r = 2\alpha/(\beta^2 + 1) . \tag{68}$$

This relation is enough to find the angular structure of stress fields around a crack.

Using Eq. (68) to substitute Eq. (66) into Eq. (62) we find that

$$\sigma_{xx} = \frac{K_I}{\sqrt{2\pi}D}\left[(\beta^2 + 1)(1 + 2\alpha^2 - \beta^2)\left\{\frac{1}{\sqrt{z^\alpha}} + \frac{1}{\sqrt{\bar{z}_\alpha}}\right\}\right. \tag{69a}$$

$$\left. - 4\alpha\beta\left\{\frac{1}{\sqrt{z_\beta}} + \frac{1}{\sqrt{\bar{z}_\beta}}\right\}\right], \tag{69b}$$

$$\sigma_{yy} = \frac{K_I}{2\sqrt{2\pi}D}\left[4\alpha\beta\left\{\frac{1}{\sqrt{z_\beta}} + \frac{1}{\sqrt{\bar{z}_\beta}}\right\} - (1 + \beta^2)^2\left\{\frac{1}{\sqrt{z_\alpha}} + \frac{1}{\sqrt{\bar{z}_\alpha}}\right\}\right], \tag{69c}$$

$$\sigma_{xy} = \frac{K_I}{2\sqrt{2\pi}D}2i\alpha(\beta^2 + 1)\left\{\frac{1}{\sqrt{z_\alpha}} - \frac{1}{\sqrt{\bar{z}^\alpha}} - \frac{1}{\sqrt{z_\beta}} + \frac{1}{\sqrt{\bar{z}_\beta}}\right\}, \tag{69d}$$

with

$$D = 4\alpha\beta - (1 + \beta^2)^2 . \tag{69e}$$

Different features of Eq. (69) have varying degrees of significance. The feature of greatest physical importance is the overall scale of the stress singularity, which is characterized by the Mode I stress intensity factor

$$K_I = \lim_{\substack{x \to 0^+ \\ y = 0}} \sqrt{2\pi x}\sigma_{yy} . \tag{70}$$

As we mentioned in Section 2.1.3, and will calculate in the following Subsection, the stress intensity factor is directly related to energy flux into a crack tip.

In addition, Eq. (69) carries information about the angular structure of the stress fields. This information can be used in two ways. Experimentally, it can be used to check the predictions of fracture mechanics, and to obtain measurements of the stress fields surrounding rapidly moving cracks, as we will discuss in Section 3.2. Theoretically, it can be used to make predictions about the direction of crack motion, and the conditions under which a crack will bifurcate. We discuss these uses further in Section 2.9.

It is important to note that although Eq. (69) was derived for cracks moving at a constant speed, the same expressions are valid for cracks that accelerate and decelerate, just so long as the change in crack velocity is small during the time needed for sound to travel across the region of the universal elastic singularity. A demonstration of this claim is discussed by Freund [7].

2.6. Mode I, example of specific loading

We now briefly sketch the solution of a specific case in which the fields about the crack tip can be worked out explicitly. A source in which to find problems of this type worked out in more explicit detail is Ref. [26]. Suppose that a crack is loaded by two delta-function stresses, located a distance l_0 behind the crack tip, moving with it in steady state at velocity v, and of strength $-\sigma_c$, as shown in Fig. 7. That is,

$$\lim_{y \to 0^+} \sigma_{yy}(x,y) = -\sigma_c\delta(x + l_0) \quad \text{for } x < 0 . \tag{71}$$
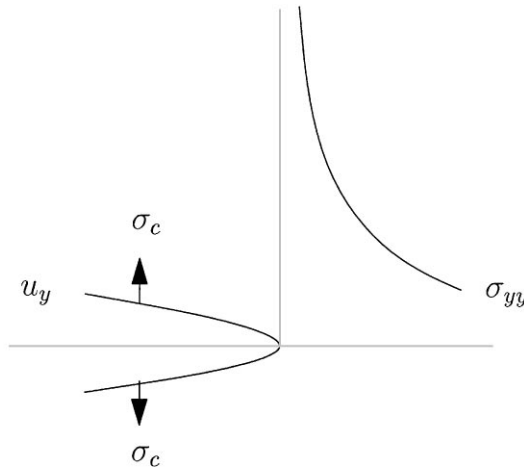
Fig. 7. A crack is loaded by the application of two delta-function stresses of strength σ_c behind the tip.

Taking the tip of the crack to sit at the origin, the stress and displacement fields are continuous and differentiable apart from a branch cut starting at the origin and running backwards along the negative x-axis. Denote by $\Phi_{\pm}(x)$ the functions

$$\Phi_{\pm}(x) \equiv \lim_{y \to 0^+} \Phi(x \pm iy) , \tag{72}$$

with $\Psi_{\pm}(x)$ defined similarly. Because of the branch cut, for $x < 0$, $\Phi_+(x) = -\Phi_-(x)$, and $\Psi_+(x) = -\Psi_-(x)$. For Mode I loading, $\sigma_{xy} = 0$ for $y \to 0^+$ and all x. From Eq. (62c)

$$2i\alpha[\Phi_+ - \bar{\Phi}_-] = (\beta^2 + 1)[\Psi_+ + \bar{\Psi}_-] , \tag{73}$$

using the fact that $\overline{\Psi(x + i\varepsilon)} = \bar{\Psi}(x - i\varepsilon)$. A bar over a function means that if one expresses the original function as a power series, one replaces all the coefficients with their complex conjugates. The function

$$F_+(x) = 2i\alpha\Psi_+(x) - (1 + \beta^2 + 1)\Psi_+(x) \tag{74}$$

is defined for all x, and can be analytically continued above the x-axis, where it is related to stresses, and must be free of singularities. Similarly, F_- must be free of singularities below the real axis. Whenever two complex functions are equal, one without singularities above the x-axis, and the other without singularities below the x-axis, the two must individually equal a constant. The constant must be zero, since all stresses die off to zero far from the crack. It follows that $F_+ = F_- = 0$, and one has finally

$$2i\Phi_+(x) = (1 + \beta^2)\Psi_+(x) \quad \text{and} \quad 2i\bar{\Phi}_-(x) = (1 + \beta^2)\bar{\Psi}_-(x) . \tag{75}$$

We now turn to the boundary condition on σ_{yy}, which from Eq. (62d) is, for $x < 0$,

$$\sigma_{yy} = -\mu(1 + \beta^2)(\Phi_+ + \bar{\Phi}_-) - 2i\beta\mu(\Psi_+ - \bar{\Psi}_-) = -\sigma_c\delta(x + l_0) . \tag{76}$$

Employing Eqs. (75) and (69), Eq. (76) becomes

$$\sigma_{yy} = -\sigma_c \delta(x + l_0) = (\mu D/2i\alpha)(\Psi_+ - \bar{\Psi}_-) . \tag{77}$$

Representing the delta function as

$$\delta(x + l_0) = \frac{i}{\pi} \frac{1}{x + l_0 + i\varepsilon} , \tag{78}$$

one can argue that the only complex function that decays properly at infinity, has a singularity no worse than a square root at the origin, and obeys Eq. (77) is

$$\Psi_+(x) = \frac{i\alpha}{D\mu\pi} \frac{\sigma_c}{x + l_0 + i\varepsilon} \sqrt{\frac{l_0}{x}} . \tag{79}$$

The function $\Psi(z)$ can now be obtained by analytical continuation of $\Psi_+(x)$. In particular, the stress σ_{yy} can easily be found for $x > 0$ from Eq. (77) and it is

$$\sigma_{yy} = \frac{1}{\pi} \sqrt{\frac{l_0}{x}} \frac{\sigma_c}{x + l_0} . \tag{80}$$

The stress intensity factor associated with this stress field is

$$K_I = \sigma_c \sqrt{2/\pi l_0} . \tag{81}$$

This result will be useful in our discussions of cohesive zone models in Section 6.1.

2.7. The J integral and the equivalence of the Irwin and Griffith points of view

What are the conditions under which a crack propagates? In the calculations above we have calculated the value of the stress fields at the tip of a moving crack, but have not addressed the conditions under which a crack will actually move. In 1920, A.A. Griffith [27] proposed that fracture occurs when the energy per unit area released by a minute extension of a crack is equal to that necessary to create new fracture surface, Γ. This idea is the final simplifying assumption of fracture mechanics. In general form, it states that the dynamics of a crack tip depend only upon the total energy flux G per unit area into the process zone. All details about the spatial structure of the stress fields are irrelevant. The energy G creates new fracture surfaces, and also is dissipated in numerous ways near the crack tip. The form the crack velocity v takes can be a general function, $v(G)$.

Conventionally, response of the crack is expressed in a different way. It is usual to write $\Gamma(v)$ to represent the energy consumed in the process zone by a crack as a function of its velocity, in which case the equation of motion for a crack is

$$G = \Gamma(v) . \tag{82}$$

Engineering fracture mechanics is mainly concerned with the conditions under which a static crack begins to move. The critical fracture energy Γ_c is the minimal energy per unit area needed for a crack to move ahead, irrespective of velocity. It is usually assumed that the velocity consuming the minimal energy is a very small one, but this assumption is not necessarily correct. One can

equivalently define a critical stress intensity factor K_{Ic} at which the crack first begins to move. The equivalence is provided by Eq. (14), which we will now derive.

In the following calculation, adopt the summation convention for repeated indices. Energy flux may be found from the time derivative of the total energy. We have

$$\frac{d}{dt}[T + U] = \frac{d}{dt}\int dx\, dy\left[\frac{\rho}{2}\dot{u}_\alpha \dot{u}_\alpha + \frac{1}{2}\frac{\partial u_\alpha}{\partial x_\beta}\sigma_{\alpha\beta}\right], \tag{83}$$

where T and U are, respectively, the total kinetic and potential energies within the entire medium. The spatial integral in Eq. (83) is taken over a region which is static in the laboratory frame. So

$$\frac{d}{dt}[T + U] = \int dx\, dy\left[\rho \ddot{u}_\alpha \dot{u}_\alpha + \frac{\partial \dot{u}_\alpha}{\partial x_\beta}\sigma_{\alpha\beta}\right], \tag{84}$$

where the symmetry of the stress tensor under interchange of indices is used for the last term. Using the equation of motion

$$\rho \ddot{u}_\alpha = (\partial/\partial x_\beta)\sigma_{\alpha\beta}, \tag{85}$$

we have

$$\int dx\, dy\left[\frac{\partial}{\partial x_\beta}\sigma_{\alpha\beta}\dot{u}_\alpha + \frac{\partial \dot{u}_\alpha}{\partial x_\beta}\sigma_{\alpha\beta}\right] \tag{86}$$

$$= \int dx\, dy\, \frac{\partial}{\partial x_\beta}[\sigma_{\alpha\beta}\dot{u}_\alpha] \tag{87}$$

$$= \int_{\partial S} \dot{u}_\alpha \sigma_{\alpha\beta} n_\beta, \tag{88}$$

where the integral is now over the boundary, ∂S, of the system, and $\hat{n}$ is an outward unit normal. As we see from Eq. (88), energy is transported by a flux vector $\boldsymbol{j}$ whose components are

$$j_\alpha = \sigma_{\alpha\beta}\dot{u}_\beta. \tag{89}$$

The total energy flux J per unit time into the crack tip is called the J integral. A convenient contour for the integration is indicated in Fig. 8. For a crack loaded in pure Mode I, using the asymptotic forms, Eq. (69), for σ_{yy} and the corresponding expressions for u_y from Eq. (69a), one finds that J is

$$J = v(1 - \beta^2)\frac{\alpha}{2\mu}\frac{1}{4\alpha\beta - (1 + \beta^2)^2}K_I^2, \tag{90}$$

where K_I is the stress intensity factor defined by Eq. (70), with a subscript I to emphasize that the result is specific to Mode I loading. Thus, the energy release rate G in the case of pure Mode I loading is

$$G = J/v = (1 - \beta^2)\frac{\alpha}{2\mu}\frac{1}{4\alpha\beta - (1 + \beta^2)^2}K_I^2 \equiv \frac{1 - v^2}{E}A_I(v)K_I^2. \tag{91a}$$
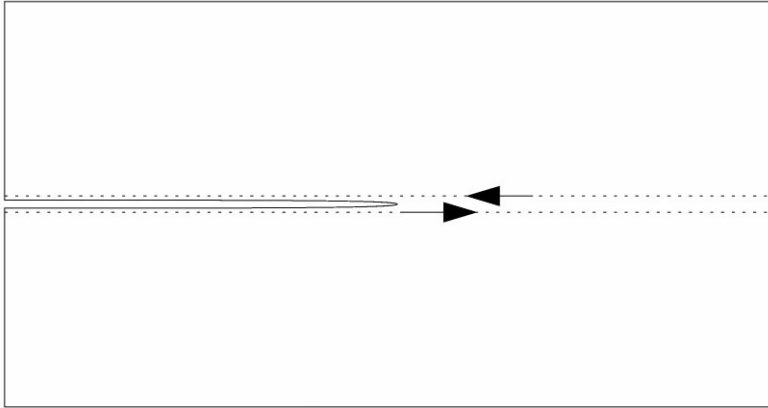
Fig. 8. The energy flowing to a crack tip can be computed by integrating the energy flux across a contour that surrounds it. The most convenient contour is depicted by the dotted line in this diagram; it runs along the *x*-axis just below the crack, closes at infinity, and runs back along the axis just above the crack. This contour is easier to handle analytically than one that has a vertical segment at some distance to the right of the crack tip.

The corresponding result for pure Mode II loading is

$$G = (1 - \beta^2)\frac{\beta}{2\mu}\frac{1}{4\alpha\beta - (1 + \beta^2)^2}K_{\text{II}}^2 \equiv \frac{1 - v^2}{E}A_{\text{II}}(v)K_{\text{II}}^2 \;, \tag{91b}$$

while for Mode III loading it is

$$G = vK_{\text{III}}^2/2\alpha\mu \;. \tag{91c}$$

It is valuable to look at the quasistatic limit of Eq. (91) where $v \to 0$. In this limit each of the functions $A_\alpha(v) \to 1$ and Eq. (91a), for example, becomes

$$G_{v\to 0} = ((1 - v^2)/E)K_{\text{I}}^2 \;. \tag{92}$$

In the general case of mixed mode fracture, the energy release is given by linear combinations of Eq. (91), as in Eq. (14).

2.7.1. Significance and limitations

The functions $A_\alpha(v)$, in Eq. (91), are universal function in the sense that they are independent of most details of the system's loading or geometric configuration. They do depend upon the instantaneous velocity of the crack. Eq. (91) is of great significance in the study of fracture. Assuming that there is no energy sink in the system other than at the tip of the crack, it relates the total flow of energy from the entire elastic medium to the tip of the crack. Setting the flow equal to the energy dissipated in the process zone determines an equation of motion for the crack. It is important to emphasize assumptions that were tacitly made in the derivation of this relation. The first is that near field descriptions of stress and displacement fields given by Eq. (69), Eq. (60) is valid. If, for example, the process zone is on the order of 1 mm in a sample whose dimensions are a few centimeters, the value of the stress field on the contour ∂S used in Eq. (88) will not be approximated well by the asymptotic forms of the stress and displacement fields, invalidating Eq. (91).

In obtaining an equation of motion for a crack, an additional ingredient is missing. Energy balance carries no information about a crack's *path*. We have assumed that the crack travels in a straight line. We will return to this issue in Section 2.9. The rules determining paths of slowly moving cracks are known, but for rapidly moving cracks, the problem is largely unsolved.

2.8. The general equation for the motion of a crack in an infinite plate

2.8.1. General formalism

An equation of motion for a crack now comes down to the calculation of either the energy release rate, G or, equivalently, the dynamic stress intensity factor, K. We will now show how to find a general expression for K as a function of the loading history of a crack, its length, and its velocity. This general expression will then be used to derive an equation of motion for a moving crack in a number of important situations. The calculation, due to Eshelby [28], Freund [7], Kostrov [29,30], and Willis [31] is somewhat limited. It applies only to a perfectly straight semi-infinite crack in an infinite plate, with loads applied to the crack faces. Given these restrictions the calculation is exact, and holds with remarkable generality. The calculation is somewhat heavy going, and in the end reproduces the scaling result of Eq. (11) with almost no modification, as a special case. Our presentation most closely follows Willis [31].

Because this calculation is performed in the context of linear elasticity, it must be posed as a boundary-value problem. The most general problem to which a solution has been found is

1. The crack is a semi-infinite branch cut running along a straight line an in an infinite isotropic two-dimensional elastic plate.
2. The velocity of the crack $v(t)$ is not required to be constant. The position of the tip is $l(t) = \int^t dt'\, v(t')$. In the boundary-value problem, $l(t)$ and $v(t)$ are assumed to be known. The only restriction is that $v(t)$ must be less than relevant sound speeds at all times.
3. External stresses σ_{ext} are permitted only along the crack line; They are allowed arbitrary time and space dependence otherwise. The most faithful experimental realizations of this restriction load cracks by placing wedges between the crack faces.
4. The calculation is carried out in the three symmetric loading modes, I, II and III. The symbols u, σ, and c will denote a displacement, a stress, and a sound speed in each case, as shown in Table 2. In all cases, $u(x,t) = 0$ for $x > l(t)$, by symmetry.
5. The end result of the calculation is the energy flux G as a function of the position $l(t)$ of the crack, of the instantaneous velocity $v(t)$, and as a functional of the load $\sigma_{ext}(x,t)$.

Table 2
See Fig. 5 for a definition of the coordinatesystem. c_R is the Rayleigh wave speed, determined by the zero of D in Eq. (69e), usually around 90% of the transverse wave speed c_t

	Mode I	Mode II	Mode III
u denotes	$u_y(x, y = 0^+, t)$	$u_x(x, y = 0^+, t)$	$u_z(x, y = 0^+, t)$
σ denotes	$\sigma_{yy}(x, y = 0^+, t)$	$\sigma_{yx}(x, y = 0^+, t)$	$\sigma_{yz}(x, y = 0^+, t)$
c denotes	c_R	c_R	c_t

The strategy is to look for a Green function, $\mathscr{G}$ operating on the displacement field such that:

$$\mathscr{G}*u \equiv \int dx'\, dt'\, \mathscr{G}(x - x', t - t') u(x', t') = \sigma(x,t) . \tag{93}$$

The fracture problem is soluble if the Green function $\mathscr{G}$ has a special form. Writing

$$\mathscr{G}(k,\omega) = \int dx'\, dt'\, e^{ikx' - i\omega t'} \mathscr{G}(x', t') , \tag{94}$$

the special form requires that $\mathscr{G}$ be decomposed as

$$\mathscr{G}(k,\omega) \equiv \mathscr{G}^-(k,\omega)/\mathscr{G}^+(k,\omega) . \tag{95}$$

Upon transforming back to real space, the two functions $\mathscr{G}^\pm$ need to have the properties that $\mathscr{G}^+(x,t)$ vanishes for $x < c_R t$, and $\mathscr{G}^-(x,t)$ vanishes for $x > -c_R t$, where c_R is the Rayleigh wave speed. That is, $\mathscr{G}^+$ is nonzero only for x so large that a pulse beginning at the origin at $t = 0$ could never reach it in the forward direction, and $\mathscr{G}^-$ is defined similarly. In fact, for the cases to be discussed below

$$\mathscr{G}^+ \propto \delta(x - c_R t) \quad \text{and} \quad \mathscr{G}^- \propto \delta(x + c_R t) . \tag{96}$$

It is far from immediately obvious that $\mathscr{G}$ can be decomposed in this way, or even that a function $\mathscr{G}$ must exist to satisfy Eq. (93), but for the moment we simply assume these facts and examine their consequences.

Decompose σ into two functions

$$\sigma = \sigma^+ + \sigma^- , \tag{97}$$

and let us define

$$u = u^- , \tag{98}$$

where σ^+ vanishes for $x < l(t)$, σ^- vanishes for $x > l(t)$, and u^- vanishes for $x > l(t)$. Thus, σ^- corresponds to the known function which describes the stresses along the crack faces and σ^+ is an, as yet unknown, function. The function u^-, on the other hand, is an unknown function along the crack faces and vanishes ahead of the crack tip.

Using Eqs. (93) and (95), we can write

$$\mathscr{G}*u = \sigma \tag{99}$$

$$\Rightarrow \mathscr{G}(k,\omega)u(k,\omega) = \sigma(k,\omega) \tag{100}$$

$$\Rightarrow \mathscr{G}^-(k,\omega)u(k,\omega) = \mathscr{G}^+(k,\omega)\sigma(k,\omega) \tag{101}$$

$$\rightarrow \mathscr{G}^+*\sigma = \mathscr{G}^-*u . \tag{102}$$

From Eq. (102) one can solve formally for the stress and strain fields as follows. We first show that for $x < l(t)$ $\mathscr{G}^+*\sigma^+ = 0$. Consider $x > l(t)$. Because σ^+ is zero behind the crack

$$\mathscr{G}^+*u^+ = \int dx'dt'\mathscr{G}^+(x - x', t - t')\sigma^+(x', t') \tag{103}$$

is certainly zero whenever $x' < l(t')$. The only chance for the integrand to be nonzero is for $x' > l(t')$. In this case

$$x' - x > l(t') - l(t) = \dot{l}(t^\star)(t' - t) ,\tag{104}$$

where $t^\star$ is some time between t and t'. However, this means that

$$x - x' < (t - t')[c_R] ,\tag{105}$$

since c_R is the largest value the crack velocity can have. Eq. (105) is precisely the condition for $\mathscr{G}^+(x - x', t - t')$ to vanish. The conclusion is that

$$\int dx' dt' \mathscr{G}^+(x - x', t - t')\sigma^+(x', t') = 0 \quad \text{for } x < l(t) .\tag{106}$$

An identical argument shows that

$$\int dx' \, dt' \mathscr{G}^-(x - x', t - t')u^-(x', t') = 0 \quad \text{for } x > l(t) .\tag{107}$$

Defining

$$H(x,t) = \theta(x - l(t)) ,\tag{108}$$

where θ is a Heaviside step function, one can deduce from Eq. (102) that

$$\mathscr{G}^+ *\sigma^+ = -[\mathscr{G}^+ *\sigma^-]H(x,t) ,\tag{109}$$

which has now been shown to be true both for $x > l(t)$, and for $x < l(t)$. But Eq. (109) can be inverted to give

$$\sigma^+ = -\mathscr{G}^{+-1}*\{[\mathscr{G}^+ *\sigma^-]H\} .\tag{110}$$

Since σ^- is a known stress to the rear of the crack tip, Eq. (110) provides a formal solution in terms of the decomposed Green function. The most interesting thing to pull from this formal expression is the stress intensity factor

$$K = \lim_{\varepsilon \to 0_+} \sqrt{2\pi\varepsilon}\, \sigma(\varepsilon + l,t) ,\tag{111}$$

which means identifying the terms that lead to a divergence of the form $1/\sqrt{\varepsilon}$ as $x = l(t) + \varepsilon$ approaches $l(t)$ from above.

The detailed analysis to follow will demonstrate that $\mathscr{G}^{+-1}$ has a singularity for $\varepsilon \to 0$ going as $1/\sqrt{\varepsilon^3}$, while $\mathscr{G}^+ *\sigma^+$ is finite. Therefore, in searching for the singularity in Eq. (110), $\mathscr{G}^+ *\sigma^+$ can be evaluated at $x = l(t)$ and pulled outside the convolution as a multiplicative factor. The stress intensity factor can therefore be written

$$K = \tilde{K}(l(t))\cdot \mathscr{K}(v) ,\tag{112a}$$

where

$$\tilde{K}(l) \equiv -[\sqrt{2}\mathscr{G}^+ *\sigma^-]_{(l,t)}\tag{112b}$$

and

$$\mathscr{K}(v) \equiv \lim_{\varepsilon \to 0_+} \{\sqrt{\pi\varepsilon}\, \mathscr{G}^{+\,-1} * H\}_{(l+\varepsilon,t)} . \tag{112c}$$

The stress intensity factor is therefore the product of two terms. The first, $\tilde{K}(l,\sigma)$ is the stress intensity factor that would emerge at the tip of a static crack sitting at l for all times, subjected to the load $\sigma^-(t)$. $\tilde{K}$ does not depend upon crack velocity at all. The second term, $\mathscr{K}$ turns out to depend only upon instantaneous velocity v of the crack, but is otherwise completely unaware of the crack's history.

2.8.2. Application to Mode III

We shall now apply the general result (112) to the particular case of anti-plane shear, and recover the result first found by Kostrov [29] and Eshelby [28]. Along the way it will be possible to verify the various claims about the structure of the Green function $\mathscr{G}$. By calculating the stress intensity factor, we will, using Eq. (91), equate the energy release rate to the fracture energy thereby obtaining the equation of motion for a Mode III crack. The qualitative features of the resulting equation of motion are, as we shall see, applicable to Mode I.

The starting point is Eq. (20), the wave equation for u_z. Fourier transforming in both space and time by

$$\int dx\, dt\, e^{ikx + i\omega t} \tag{113}$$

one has that

$$\partial^2 u_z / \partial y^2 = [k^2 - \omega^2/c^2 - 2ib\omega]u_z , \tag{114}$$

where a tiny amount of damping, b, has been added to take care of some convergence problems that will arise later. Only the solutions that decay as a function of y are allowed in an infinite plate, so Eq. (114) is solved by

$$u_z(k,y,\omega) = e^{-y\sqrt{k^2 - \omega^2/c^2 - 2ib\omega}} u(k,\omega) . \tag{115}$$

Right on the x-axis, taking $u = u_z(y = 0)$ and $\sigma = \sigma_{yz}(y = 0)$, one has that

$$\mathscr{G}(k,\omega) = \sigma/u = -\mu\sqrt{k^2 - \omega^2/c^2 - 2ib\omega} . \tag{116}$$

Decompose $\mathscr{G}$ as

$$\mathscr{G} = \mathscr{G}^- / \mathscr{G}^+ \tag{117}$$

with

$$\mathscr{G}^- = -\mu\sqrt{ik - i\omega/c + b} \tag{118}$$

and

$$\mathscr{G}^+ = 1/\sqrt{-ik - i\omega/c + b} . \tag{119}$$

To verify that this decomposition satisfies the conditions of the preceding section, find

$$\mathscr{G}^+(x,t) = \int \frac{dk\,d\omega}{2\pi\,2\pi} \frac{e^{-ikx-i\omega t}}{\sqrt{-ik-i\omega/c+b}} \tag{120}$$

$$= \int \frac{dp\,d\omega}{2\pi\,2\pi} \frac{e^{-ipx-i\omega(t-x/c)}}{\sqrt{-ip+b}}, \tag{121}$$

with $p = k + \omega/c$

$$= \delta(t-x/c) \int \frac{dp}{2\pi} \frac{e^{-ipx}}{\sqrt{-ip+b}}. \tag{122}$$

When $x < 0$, one must close the contour in the upper half plane, and as the branch cut is in the lower half plane one gets zero. When $x > 0$, deform the contour to surround the branch cut, and get

$$\int_0^\infty \frac{dp}{2\pi} \frac{2e^{-px}}{\sqrt{p+b}} = \frac{1}{\sqrt{\pi x}}. \tag{123}$$

Therefore

$$\mathscr{G}^+(x,t) = \delta(t-x/c)\theta(x)/\sqrt{\pi x}. \tag{124}$$

To find $\mathscr{G}^{+\,-1}$ one must do

$$\mathscr{G}^{+\,-1}(x,t) = \int \frac{dk\,d\omega}{2\pi\,2\pi} e^{-ikx-i\omega t} \sqrt{-ik-i\omega/c+b} \tag{125}$$

$$= \delta(t-x/c) \int \frac{dp}{2\pi} e^{-ipx} \sqrt{-ip+b}. \tag{126}$$

One cannot legitimately deform the contour to perform this integral, but can instead write that

$$\int \frac{dp}{2\pi} e^{-ipx} \sqrt{-ip+b} = \frac{\partial}{\partial x} \int \frac{dp}{2\pi} \frac{e^{-ipx}}{\sqrt{-ip+b}}, \tag{127}$$

obtaining in this way

$$\mathscr{G}^{+\,-1}(x,t) = \delta(t-x/c) \frac{\partial}{\partial x} \left[\frac{\theta(x)}{\sqrt{\pi x}} \right]. \tag{128}$$

Having now calculated $\mathscr{G}^{+\,-1}(x,t)$, we are now in a position to find the stress intensity factor, $K(l,t)$, by using the general relation Eq. (112a). Using the expression for $\mathscr{G}^{+\,-1}$ derived in Eq. (128), the velocity dependent, singular integral, Eq. (112), becomes

$$\mathscr{K}(v) = \sqrt{\pi\varepsilon} \int dx_1\,dt_1\,\delta(t_1-x/c) \left[\frac{\partial}{\partial x_1} \frac{\theta(x_1)}{\sqrt{\pi x_1}} \right] \theta(l(t)+\varepsilon - x_1 - l(t-t_1)) \tag{129}$$

$$= \sqrt{\pi \varepsilon} \int \frac{dx_1}{\sqrt{\pi}} \left[\frac{\partial}{\partial x_1} \frac{\theta(x_1)}{\sqrt{x_1}} \right] \theta(\varepsilon/[1 - v/c] - x_1) , \tag{130}$$

since only very small x_1 are important

$$= \sqrt{\pi \varepsilon} \int \frac{dx_1}{\sqrt{\pi}} \frac{\theta(x_1)}{\sqrt{x_1}} \delta(\varepsilon/[1 - v/c] - x_1) \tag{131}$$

$$= \sqrt{1 - v/c} . \tag{132}$$

We will now use the expression obtained for $\mathcal{G}^+$ (Eq. (124)) to calculate the expression for $\tilde{K}(l(t))$ in Eq. (112a):

$$\tilde{K} = -\sqrt{2} \int dx_1 \, dt_1 \delta(t_1 - x_1/c) \frac{\theta(x_1)}{\sqrt{\pi x_1}} \sigma^-(l(t) - x_1, t - t_1) \tag{133}$$

$$= -\sqrt{2} \int dx_1 \frac{\theta(x_1)}{\sqrt{\pi x_1}} \sigma^-(l(t) - x_1, t - x_1/c) . \tag{134}$$

This is as far as one can take matters without an explicit expression for σ^-. However, for the particular case where σ^- is time independent and

$$\sigma(x) = \sigma_0 \theta(x) , \tag{135}$$

one gets

$$\tilde{K} = -\sigma_0(4/\sqrt{2\pi})\sqrt{l} . \tag{136}$$

The reason for the minus sign is that stresses ahead of the crack tip always counteract those on applied on the crack faces.

Notice that Eq. (132) reduces to unity when $v \to 0$. This means that in the case of time-independent loading, $\tilde{K}$ is indeed the stress intensity factor one would have had if the crack had been located unmoving at l for all time. For the moving crack, we have

$$K = \sqrt{1 - v/c} \, \tilde{K}(l(t)) . \tag{137}$$

One computes the stress singularity that would have developed if one had a static crack of the present length, $l(t)$, and multiplies by a function of the instantaneous velocity. It should be stressed that all details of the history of the crack motion are irrelevant, and only the velocity and loading configuration are needed to find the stress fields sufficiently close to the tip. As a consequence, one can use Eq. (91c) to determine the energy flow to the tip of the crack. It is

$$J = v(1 - v/c)\tilde{K}^2/2\alpha\mu . \tag{138}$$

Finally, one can present the equation of motion for the crack. The rate at which energy enters the tip of the crack must be equal to $v\Gamma(v)$. There is nothing to prevent the fracture energy Γ from being a function of velocity, but the notions of local equilibrium which have prevailed until now strongly suggest that it should not depend upon anything else. So one must have

$$\Gamma(v) = (1 - v/c)\tilde{K}^2(l)/2\alpha\mu , \tag{139}$$

which by writing out α and $\tilde{K}$ may be rewritten as

$$\mu \Gamma \pi / 4 l \sigma_0^2 = \sqrt{(1 - v/c)/(1 + v/c)} \tag{140}$$

or defining

$$l_0 = \mu \Gamma \pi / 4 \sigma_0^2 \tag{141}$$

as

$$l_0/l = \sqrt{(1 - v/c)/(1 + v/c)} \;. \tag{142}$$

2.8.3. Application to Mode I

The same analysis may be carried out for thin plates under tension. Everything proceeds as before, except that it is not possible to display simple analytical expressions, although there are excellent approximations that can be put in simple form. We will just record the final result, discussed in more detail by Freund [7], that gives the energy flux to the tip of the crack. The result we quote is for plane stress, which is characterized by a Lamé constant $\tilde{\lambda}$ defined by Eq. (27). After computing $\mathcal{K}(v)$, and multiplying by the function $A_I(v)$ from Eq. (91), Freund finds that the energy flux per unit length extension of the crack is to a good approximation

$$G(v) = \Gamma(v) = \frac{(1 - v/c_R)\tilde{K}^2(l)}{2\tilde{\lambda}} \tag{143}$$

$$\Rightarrow \frac{E \Gamma(v)}{(1 - v^2)\tilde{K}^2(l)} = 1 - \frac{v}{c_R} \;, \tag{144}$$

where c_R is the Rayleigh wave speed (the speed at which the function D given in Eq. (69c) vanishes), $\tilde{K}$ is still given by Eq. (134), using σ_{yy} on the x-axis for σ. In the case of time-independent loading described by Eq. (135) one gets

$$l_0/l = 1 - v/c_R \;, \tag{145}$$

with

$$l_0 = \pi \Gamma \tilde{\lambda} / 4 \sigma_0^2 \tag{146}$$

or

$$v = c_R(1 - l_0/l) \;. \tag{147}$$

Surprisingly enough, the elaborate analysis above reproduces the result of the simplest scaling arguments, Eq. (11). Placing the result in the form of Eq. (147) is a bit misleading, since it hides the possibility that Γ and hence l_0 can depend strongly upon the crack velocity v. Large apparent discrepancies between theory and experiment have been due to nothing more than assuming that l_0 could be treated as a constant. We will discuss this subject more in Section 4.1.

2.8.4. Practical considerations

We now briefly discuss some of the considerations implied by Eq. (143) in the design of experiments. We discuss three experimental geometries; one where presumptions of the theory are

met well, a second where they are satisfied in an approximate fashion, and a third where they clearly fail.

1. A thin plate has a crack running half-way through, and driven by wedging action in the middle. For times less than that needed for sound to travel from the point of loading to system boundaries and back to the tip of the crack, all the assumptions of the theory are obeyed.

2. A thin plate has a long crack as before, but now uniform static stresses σ_∞ are applied at the outer boundaries, while the faces of the crack are stress-free. This problem is equivalent to one in which the upper and lower outer boundaries are stress-free, but uniform stresses $-\sigma_\infty$ are applied along the crack faces. The reason for the equivalence is that an uncracked plate under uniform tension σ_∞ is a solution of the equations of elasticity, so this trivial static solution can be subtracted from the first problem, to obtain the second equivalent one. Unfortunately, in this new problem, stresses are being applied to the crack faces all the way back to the left-hand boundary of the sample. The problem needs to be mapped onto one where stresses are applied to the faces of a semi-infinite crack in an infinite plate, and the correspondence is only approximate.

3. Finally, consider a semi-infinite crack in an infinitely long strip, shown in Figs. 9 and 10. The strip is loaded by displacing each of its boundaries at $y = \pm W/2$ by a constant amount δ. Far behind the crack tip as $x \to -\infty$ all the stresses within the strip have been relieved by the crack. Far ahead of the crack tip, as $x \to +\infty$, the medium is unaffected by the crack with the
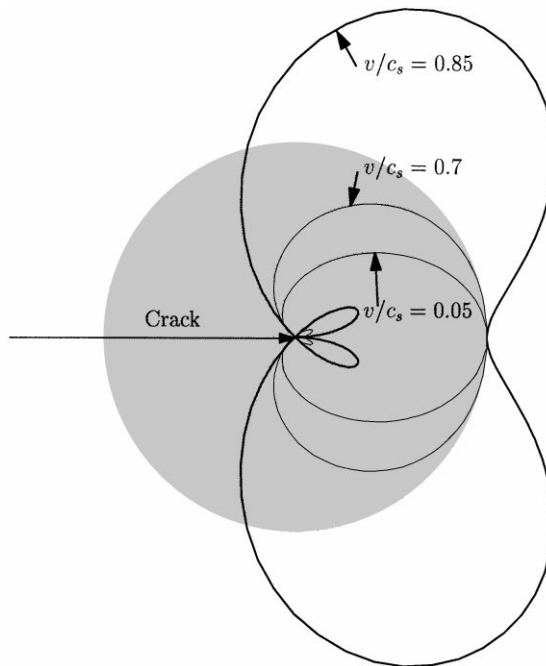
Fig. 9. Stress $\sigma_{\theta\theta}$ in a polar plot for various values of v/c_s. For v/c_s, the maximum tensile stress clearly lies ahead of the crack at $\theta = 0$. For $v/c_s = 0.7$, the maximum has moved away from $\theta = 0$, but the change is so slight it is scarcely visible, while by $v/c_s = 0.85$ the maximum tensile stress is clearly far off the axis. The small inner loops near the crack tip result from compressive stresses near $\theta = \pi$.

Fig. 10. Some typical experimental loading configurations.

stress field linear in y. Thus, the energy per unit extension far ahead of the crack has a constant value of
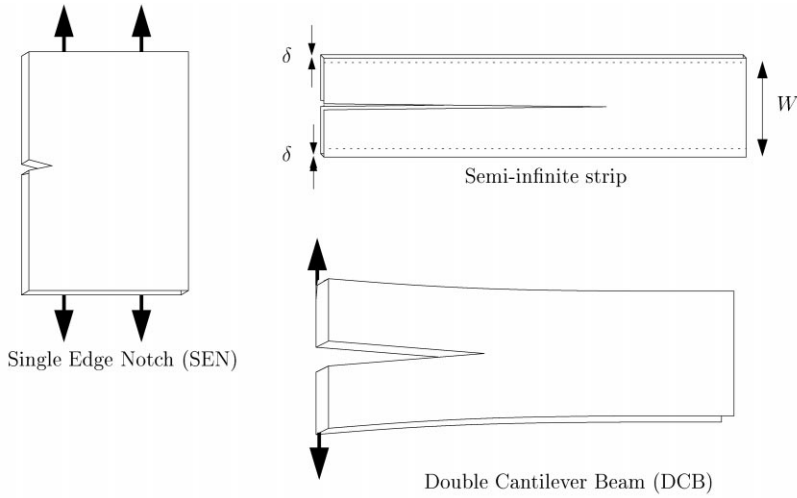
$$2E\delta^2/W(1-v^2) \, , \tag{148}$$

where E and v are, respectively, Young's modulus and Poisson ratio of the material. The translational invariance of the system along x suggests that the crack should ultimately propagate at a constant velocity v, for a given extension δ. Balancing energy as usual,

$$G = \Gamma = 2E\delta^2/W(1-v^2) \, . \tag{149}$$

Now assume that it is still valid to use Eq. (143). The stress intensity factor $\tilde{K}$ of a static crack in a strip loaded with constant displacements δ cannot depend upon where the crack is located, so $\tilde{K}$ is a constant, and Eq. (143) would predict

$$G = \Gamma = \frac{(1-v^2)\tilde{K}^2}{E}(1 - v/c_{\mathrm{R}}) \, . \tag{150}$$

The velocity dependence on the right-hand side of Eq. (150) contradicts Eq. (149), and is simply wrong. The reason for the failure of Eq. (143) in this case is that the assumption that the crack tip does not feel the presence of the system's boundaries is obviously not valid. The translational invariance of the system is in fact, crucially dependent on the presence of its vertical boundaries. Energy is continuously reflected back into the system as the amount of kinetic energy reaches a steady state. In contrast, the kinetic energy within a system of infinite extent increases indefinitely as ever farther reaches of material learn about the moving crack, while elastic waves carrying the information propagate outward.

2.9. Crack paths

We now briefly discuss the path chosen by a moving crack. Energy balance provides an equation of motion for the tip of a crack only when the crack path or propagation direction is assumed. Although criteria for a crack's path have been established for a slowly moving cracks, no such criterion has been proven to exist for a crack moving at high speeds.

2.9.1. Quasistatic crack paths

A slow crack is one whose velocity v is much less than the Rayleigh wave speed c_R. The path followed by such cracks obeys the "the principle of local symmetry", first proposed by Goldstein and Salganik [32]. This criterion states that a crack extends so as to set the component of Mode II loading to zero. One consequence is that if a stationary crack is loaded in such a way as to experience Mode II loading, upon extension it forms a sharp kink and moves at a new angle. A simple explanation for this rule is that it means the crack is moving perpendicular to the direction in which tensile stresses are the greatest. Cotterell and Rice [21] have shown that a crack obeying this principle of local symmetry is also choosing a direction so as to maximize the energy release rate. The distance over which a crack needs to move so as to set K_{II} to zero is on the order of the size of the process zone; Hodgdon and Sethna [33] show how to arrive at this conclusion using little more than symmetry principles.

Cotterell and Rice also demonstrated that the condition $K_{II} = 0$ has the following consequences for crack motion. Consider an initially straight crack, propagating along the x-axis. The stress field components σ_{xx} and σ_{yy} have the following form:

$$\sigma_{xx} = (K_I/(2\pi r)^{1/2}) + T + \mathcal{O}(r^{1/2}) , \tag{151a}$$

$$\sigma_{yy} = (K_I/(2\pi r)^{1/2}) + \mathcal{O}(r^{1/2}) . \tag{151b}$$

The constant stress T is parallel to the crack at its tip. Cotterell and Rice showed that if $T > 0$, any small fluctuations from straightness cause the the crack to diverge from the x direction, while if $T < 0$ the crack is stable and continues to propagate along the x-axis. They also discuss experimental verification of this prediction.

Yuse and Sano [34] and Ronsin et al. [35] have conducted experiments by slowly pulling a glass plate from a hot region to a cold one across a constant thermal gradient. The velocity of the crack, driven by the stresses induced by the nonuniform thermal expansion of the material, follows that of the glass plate. At a critical pulling velocity, the crack's path deviates from straight-line propagation and transverse oscillations develop. This instability is completely consistent with the principle of local symmetry [36,37]; the crack deviates from straightness when T in Eq. (151) rises above 0. Adda-Bedia and Pomeau and Ben-Amar [38] have extended the analysis to calculate the wavelength of the ensuing oscillations.

Hodgdon and Sethna [33] have generalized the principle of local symmetry to three dimensions. They show that an equation of motion for a crack line involves, in principle, nine different constants. It would be interesting for an experimental study to follow upon their work and try to measure the many constants they have described, but we are not aware of such experiments. Larralde and Ball [39,40] analyzed what such equations would imply for a corrugated crack, and

found that the corrugations should decay exponentially. They also performed some simple experiments and verified the predictions.

Thus, the principle of local symmetry is consistent with all experimental tests that have been performed so far on slowly moving cracks. Nevertheless, it does not rest upon a particularly solid foundation. There is no basic principle from which it follows that a crack must extend perpendicular to the maximum tensile stress, or that it must maximize energy release.

2.9.2. Dynamic crack paths

The absence of a rigorous basis on which to decide which direction a crack will move becomes particularly perplexing in the case of rapid fracture. A variety of path selection criteria for rapid fracture has been proposed in the literature. They can be divided into two types, those proposing that a crack propagate in the direction of a maximal stress and those that are based on a maximum dissipation of energy. In contrast to the case of quasistatic fracture, these criteria are not equivalent, and none of them is broadly supported by experiment.

2.9.3. Yoffe instability

Yoffe [17] proposed that one check the stability of a rapidly moving crack by returning to the dynamic stress fields recorded in Eq. (69), approaching the tip of the crack along a line at angle θ to the x-axis, and computing the stress perpendicular to that line. One wants to choose

$$z_\alpha = r \cos\theta + ri\alpha \sin\theta, \quad z_\beta = r \cos\theta + ri\beta \sin\theta , \tag{152}$$

and to evaluate the stress

$$\sigma_{\theta\theta} = [\cos^2\theta]\sigma_{yy} + [\sin^2\theta]\sigma_{xx} - [\sin(2\theta)]\sigma_{xy} . \tag{153}$$

Below a velocity of about $0.61c_s$, depending upon the Poisson ratio, the maximal tensile stress occurs for $\theta = 0$. Yoffe noticed that above this critical velocity, the tensile stress $\sigma_{\theta\theta}$ develops a maximum in a direction $\theta > 0$. Above this velocity, the angle of maximum tensile stress smoothly increases until finally it develops a maximum at about $\pm 60°$ relative to the x-axis. Thus, above the critical velocity a crack might be expected to propagate off-axis. The physical reason for this spontaneous breaking of the axial symmetry of the problem stems from purely kinetic effects. In an elastic medium information is conveyed at the sound speeds. The stress field at the tip of a rapidly moving crack is analogous to the electric field surrounding a point charge moving at relativistic velocities. The stress field then experiences a Lorentz contraction in the direction of propagation as the crack's velocity approaches the sound speed. As a result, symmetric lobes around the x-axis of maximal tensile stress are formed above a critical velocity.

Yoffe's critical velocity was first considered to provide a criterion for crack branching until it was noted, experimentally, that large-scale branching occurs in a variety of materials at velocities much less than this one. In addition, branching angles of order 10–15° instead of the 60° angle predicted by Yoffe are generally observed.

2.9.4. Other crack branching criteria

To address the failure of the Yoffe criterion as a prediction for crack branching, a number of other criteria have been proposed [7,41]. The form of the stress field at the boundary of the process zone around the crack tip has been used to derive criteria for the branching angle of a crack

[42,43]. Criteria of this sort are based on the determination of the direction in which the local energy density, evaluated at the edge of the process zone, is maximal. The underlying assumption for this criterion, which was originally suggested by Sih [44], is that crack propagation occurs in the radial direction along which the local energy density possesses a stationary value. Variants of this criterion have yielded branching angles consistent with those experimentally measured. On the other hand, these same criteria predict critical velocities for crack branching that are nearly identical to the one that is predicted by the Yoffe criterion. The most recent addition to this class of criteria was proposed by Adda-Bedia et al. [45]. They propose that one draw contours of constant principal stress, and look for points where these contours are perpendicular to lines drawn from the crack tip. The crack may choose to travel along such lines. According to this criterion, there are two critical speeds, a first at which the crack must choose between three possible directions, and a second at which it must choose between five possible directions. This proposal is perfectly reasonable, but there is no argument or experimental test that has shown it is to be preferred to other proposals. One rationale for all these models is the idea that microscopic voids ahead of the crack would tend to initiate growth near the edge of the process zone. Their direction would then be governed by the form of the stress field at the process zone edge.

The actual branching angles predicted by the various branching criteria are not substantially different than those trajectories determined by the following "static" condition. Let us look at the stress field formed ahead of a single moving crack. From this field one can compute [46,47] the trajectories that satisfy the quasi-static $K_{II} = 0$ condition. If one now looks at the angle determined by this trajectory at a distance r_c from the crack tip, where r_c is the typical size of the process zone, one also obtains relatively good quantitative agreement with observed branching angles.

2.9.5. Questions fracture mechanics cannot answer

Throughout the last section we have endeavored to provide an overview of continuum fracture mechanics. In general, we have seen that by balancing the energy flowing into the vicinity of a crack's tip with that required to create new surface we can predict the motion of a straight, smooth crack. Fracture mechanics predicts both the strength and functional form of the near-field stresses. These can be measured and, as we will show, agree well with the predicted values in a variety of situations. What then don't we know?

1. What are the ingredients of the fracture energy in brittle materials? How should it be expected to vary with crack velocity?
2. What sorts of processes are happening in the process zone?
3. When a rapidly moving crack follows a macroscopically curvy path, what determines its direction of motion?
4. What are the conditions under which a crack bifurcates into two macroscopic cracks?
5. Fracture surfaces can go through transitions from smooth to rough appearance. Why?

In the final sections of this paper, we will describe a dynamic instability that occurs at a critical energy flux to a smooth, initially straight crack. We will demonstrate that this instability and its resulting development may address many of the questions above, and thus present seemingly disparate phenomena as a single coherent picture of fracture.

3. Experimental methods in dynamic fracture

In this section, we will briefly review some of the main experimental methods used in the study of dynamic fracture. Depending on both the specific problem being investigated and on the experimental resources at hand, experimental methods vary greatly. In a given experiment stress is applied via externally controlled boundary conditions and the resulting behavior of the crack is observed. Some of the quantities that can be measured as the crack progresses are the crack's position and velocity, the instantaneous stress field at its tip, and the acoustic emissions resulting from its motion. On completion of an experiment, the resulting fracture surface can be measured and correlated with any of these dynamical measurements. Below, we will touch on typical ways by which the various quantities can be measured.

3.1. Application of stress

3.1.1. Static stress application

The externally imposed stress distribution determines the stresses in the immediate vicinity of the tip (or, equivalently, the stress intensity factor) and hence drive a crack. There are two general types of loading that are typical in fracture experiments, static and dynamic.

In experiments using static loading either the boundary conditions or applied stresses are constant throughout the duration of an experiment. Static loading conditions essentially imprint an initial static stress distribution into the sample. Depending on the loading and boundary conditions that are chosen, the stress intensity factor (or stored energy density) along the prospective path of a crack can increase, resulting in a continuously accelerating crack, or decrease, leading to a decelerating or possibly arrested crack. Some examples of some common loading configurations used are shown in Fig. 10 where "single edge notched" (SEN) "double cantilever beam" (DCB), and "infinite strip" loading configurations are shown. The "single edge notched" configuration is sometimes used to approximate crack propagation in a semi-infinite system. When the loading is performed via the application of constant stress at the vertical boundaries of the sample, for a large enough sample $K_I \propto \sigma \sqrt{l}$ and therefore the energy release rate, $G \propto \sigma^2 l$, becomes a linearly increasing function of the crack length. This configuration could be used, for example to study the behavior of an accelerating crack.

In the "infinite strip" configuration, loading of the sample is performed by displacing the vertical boundaries by a constant amount. In this configuration, G is constant for a crack that is sufficiently far from the horizontal boundaries of the sample. This loading would be amenable to the study of a crack moving in "steady-state", where the energy release rate, controlled by the initial displacement of the boundaries, is constant.

In the DCB configuration, when a *constant separation* of the crack faces is imposed at $l = 0$, $G \propto 1/l^4$ is a decreasing function of l and could be used to cause crack arrest. How can one use configurations like the DCB to study *dynamic* fracture? An initially imposed seed crack of length $l = l_{initial}$ would propagate the moment that G exceeds the limit imposed by the Griffith condition (8). Under ideal conditions, the crack should propagate for an infinitesimal distance and immediately come to a stop, since in this configuration G is a decreasing function of l. The Griffith criterion, however, assumes that the initial crack is as sharp as possible. However, initial seed cracks prepared in the laboratory by cutting rarely prepare a tip that is as conducive as possible to

fracture. One can think of the initially created seed crack having a finite radius at its tip thereby blunting the stress singularity. A blunt crack tip allows a substantially higher energy density to be imposed in the system prior to fracture than that allowed by a "sharp" crack. This excess elastic energy can then drive the crack beyond the constraints imposed by an initially sharp crack. In the case of the DCB configuration with constant separation imposed, the excess energy stored in the sample prior to fracture initiation can cause a crack to propagate well into the sample before crack arrest occurs.

Blunting of the singularity around a crack tip can also arise dynamically. This can be caused in the tip region by mechanisms such as nonlinear material deformation around the tip [9], by plastic flow induced by the large stress build-up, or from crack-tip shielding that results from the formation of either micro-cracks or minute bridges across the crack faces in the near vicinity of the tip [20].

The DCB configuration can also be used to generate an accelerating crack by imposing the condition of constant stress instead of constant separation at the crack faces. Under these conditions, the (quasi-static) energy release rate will increase quadratically with the crack length [20] as

$$G = 12P^2l^2/Ew^2d^3 \tag{154}$$

where P is the stress applied at opposite points on the crack faces at the edge of the sample, and w and d are, respectively, the thickness and half-width of the sample.

3.1.2. Fracture initiation

Due to the stress singularity at the tip of a crack as the radius of the crack at its tip approaches zero, fracture initiation for static loading configurations is strongly dependent on the initial crack tip radius and therefore on the preparation of the initial crack. The stress build-up preceding fracture initiation can be used to advantage to load a system with an initial energy density prior to the onset of fracture. Unfortunately, unless one is extremely careful, experimental reproducibility of the stress at fracture initiation is difficult. In Plexiglas we can achieve a reproducible stress at fracture initiation by first bringing the system to the desired stress and then either waiting several minutes for the material to fracture as a result of noise-induced perturbations or by "sharpening" the initial crack by gentle application of a razor blade at its tip, once the desired initial conditions have been reached. These tricks do not work so well in more brittle materials, such as ceramics.

3.1.3. Dynamic stress application

In some applications (e.g. the study of crack initiation before the material surrounding the crack tip has had time to react to the applied stress) very high loading rates are desirable. A common way to achieve this is by loading an initially seeded sample by collision with a guided projectile. In this way loading rates as high as $\dot{K}_I \sim 10^9 \, \mathrm{MPa}\sqrt{\mathrm{ms}^{-1}}$ [48] have been achieved. An alternative way to produce high rate loading has been achieved by means of sending a very large current through a folded conducting strip, inserted between the two faces of an initial crack. In this configuration magnetic repulsion between adjacent parts of the strip is induced by the current. This method enables direct loading of the crack faces. A high loading rate can be produced by the discharge of a capacitor-inductor bank through the strips. This method has been used to produce a pressure pulse with a step function profile on the crack faces having loading rates on the order of

$\dot{K}_{\mathrm{I}} \sim 10^5\,\mathrm{MPa}\sqrt{\mathrm{ms}^{-1}}$ [49] in experiments designed to investigate the response of a moving crack to rapidly changing stresses.

3.2. Direct measurement of the stress intensity factor

Optical methods can be used for a direct measurement of the stress intensity factor and energy release rate. Two common methods are the "shadow-spot" or "method of caustics" and photoelasticity.

The method of caustics was originally derived by Manogg [50] with significant contributions by Theocaris [51] and Kalthoff [52] in transparent materials and by Rosakis [53] in opaque materials. The method, applicable in thin quasi-2D plates, utilizes the deflection of an incident collimated beam of light as it either passes through (transparent materials) or is reflected by (opaque materials) the material surrounding the tip of a crack. Due to Poisson contraction generated by the high tensile stresses near the tip, the initially flat faces of a plate will deform inwardly. This deformation of the medium creates a lensing effect and diverts light away from the crack tip. The diverted rays will form a three dimensional surface in space in which no light propagates. When this light is imaged on a screen, a shadow ("shadow-spot") will be observed. The shadowed region will be bounded by a caustic surface or a region of high luminescence formed by the locus of the diverted rays. From the shape of the caustic surface, which can be recorded by a high speed camera, the "instantaneous" value of the stress intensity factor may be derived. The method works well with the caveat that the derivation of the stress intensity factor is based on the assumption that the angular structure of the stresses is given by Eq. (69). In the immediate vicinity of the tip, this assumption must break down as the yield stress of the material is approached. Thus, care must be taken that the curve on the material that maps onto the caustic is well away from the process zone surrounding the crack tip [54].

Photoelasticity coupled with high-speed photography can also be used to measure the stress distribution, hence the stress intensity factor, induced by a moving crack [55]. This technique is based on the birefringence induced in most materials under an imposed stress. Birefringence causes the rotation of the plane of polarization light moving through the material. The induced polarization must depend upon features of the stress tensor which are rotationally invariant, and therefore can depend only upon the two principal stresses, which are the elements in a reference frame where the stress tensor is diagonalized. In addition, there should be no rotation of polarization when the material is stretched uniformly in all directions, in which case the two principal stresses are equal. So the angular rotation of the plane of polarization must be of the form

$$C(\sigma_1 - \sigma_2)\,, \tag{155}$$

where σ_1 and σ_2 are the principal stresses at every point (eigenvalues of the stress tensor), and C is a constant that must be determined experimentally. Whenever stresses of a two-dimensional problem are calculated analytically, the results can be placed into Eq. (155), and compared with experimental fringe patterns obtained by viewing a reflected or transmitted beam of incident polarized light through a polarizer. The observed intensity is dependent on the phase difference picked up while traversing the material and hence provides a quantitative measure of the local value of the stress field. As in the method of caustics, quantitative interpretation of these measurements is limited to the region outside of the plastic zone. In transparent materials the

application of this method is straightforward. Photoelastic methods have also been extended to opaque materials by the use of birefringent coatings which, when sufficiently thin, mirror the stress field at the surface of the underlying material [56]. Surveys of experimental results obtained by the methods of caustics and photoelasticity can be found in [52] and [57], respectively.

3.2.1. Direct measurement of energy

A direct measure of the energy release rate as a function of the velocity of a moving crack can be obtained by constraining a crack to propagate along a long and narrow strip as shown in Fig. 10. This method has the advantage that it relies solely on symmetry considerations and therefore does not require additional assumptions regarding, for example, the size or properties of the process zone, as we discussed in Section 2.8.4.

A series of experiments using a long strip geometry and varying the value of δ, will result in a direct measure of $G(v)$. In experiments performed in polymethylmethacrylate (PMMA) [58] steady-state mean velocities were indeed attained once the crack length surpassed roughly half the strip height, and the measurements of $G(v)$ obtained agreed well with results previously obtained in PMMA by means of the methods of caustics [59].

3.3. Crack velocity measurements

In dynamic fracture, the tip of a crack will generally accelerate to velocities on the order of the sound speed in the sample. As the duration of a typical experiment is of order $\sim 100\,\mu s$, relatively high-speed measurement techniques are necessary. Common methods, based on either high-speed photography, resistance measurements, or the interaction of a moving crack with ultrasonic waves are briefly reviewed below.

3.3.1. Optical methods

The most straightforward method of velocity measurement is based on high-speed photography of a moving crack. This method may be used in conjunction with instantaneous measurements of the stress intensity factor by means of the method of caustics or photoelasticity. High-speed photography has some major drawbacks as a velocity measurement method. Although the frame rates of high speed cameras are typically between 200 kHz and 10 MHz, these cameras are capable of photographing only a limited number of frames (~ 30). Thus, by this method one can either provide measurements of the *mean* velocity (averaged over the interval between frames) at a few points, or, at the highest photographic rates, provide a detailed measurement of the crack velocity over a short ($\sim 3\,\mu s$) interval. An additional shortcoming of this method is that its precision is limited by the accuracy at which the *location* of the crack tip can be determined from a photograph. In the method of caustics, for example, the location of the crack tip falls within the rather large area of the (asymmetric) shadow-spot.

These problems can partially be offset by using a streak camera [60]. In this mode, film is pulled past the camera's aperture at high speed. The sample is illuminated from behind so that, at a given instant, only the light passing through the crack will be photographed. Since a crack can be made to essentially propagate along a straight line, the exposed film provides a continuous record of its length as a function of time. The intrinsic resolution of the measurement depends on the velocity of the film and the resolution of the high-speed film used. The final resolution obtained is also

dependent both on the post-processing performed on the film in order to extract the velocity measurement, and the stability of the film's travel velocity. The same type of measurement has also been performed by high-speed measurement of the total beam intensity that penetrates the sample [61]. Assuming that the crack does not change its shape, this intensity is linearly dependent on the crack's length.

3.3.2. Resistive measurements

The velocity of a rapidly moving crack can also be measured without the use of a high-speed camera. A simple way to do this is to adhere a grid of thin electrically conductive strips to a sample prior to fracture. As a crack propagates, the crack faces and therefore the conducting strips, will separate. If, for example, the strips are connected in parallel to a current source, measurement of the total electric resistance of the grid with time will provide a jump at each instant that the crack tip traverses the end of a strip. In this way the precise location of the crack tip at a number of discrete times is obtained. The thickness of the strips used must be at least an order of magnitude less than the crack face separation in order to be certain that the crack tip is not significantly ahead of the fracture of the strip. For small samples of materials such as glass, where, at fracture, the total extension of the sample can be less than $\sim 1\,\mu m$, the thickness of the resistive coating should be on the order of 200–300 Å to ensure precise measurement. The disadvantage of the conductive strip method is that the discrete measurements inherent in the method can only provide a measure of the mean velocity between strips. This method can be extended to the use of a continuous coating in place of discrete strips. The advantage of using a continuous coating is, of course, that the location of the crack tip is obtained as quickly as the voltage drop across the coating can be digitized. The change in the resistance of the coating as a function of the crack length can be either measured or calculated for any given sample geometry and electrode placement. This method has been used in experiments where the samples themselves were highly conducting with either DC excitation [62] or with skin effect conduction using RF fields [63]. In experiments on nonconducting materials a conductive coating must be used. In polymers and glass a 30 nm thick evaporated aluminum coating was successfully used [64,65] to measure the crack velocity to a precision of better than 20 m/s with a spatial resolution of order 0.5 mm. Using this method, the precision of the measurement is only limited by the background noise and the uniformity of the coating. With an evaporated coating, precise velocity measurements are actually obtained only near the sample faces. When the sample is effectively two dimensional, this does not present a limitation. This property can actually be used to advantage when one wants to correlate the instantaneous velocity with localized features formed on the fracture surface.

3.3.3. Ultrasonic measurements

A velocity measurement method called "stress wave fractography" was developed by Kerkhoff [66] and used in early studies of brittle fracture. In this method, a running crack is perturbed by an ultrasonic wave generated from a sample boundary in a direction orthogonal to the direction of crack propagation. The interaction of the sound with the crack tip causes it to be deflected periodically as it traverses the sample. The trace of this deflection is imprinted on to the resulting fracture surface. Since the temporal frequency of the modulation is that of the ultrasonic driving, measurement of the distance between neighboring surface modulations yields a nearly continuous measurement of the instantaneous velocity of the crack tip. This method has been used both in

glass and brittle polymers. Its precision is only limited by the ultrasonic frequency used (typically in the MHz range) and the precision of the surface measurement. A disadvantage of this method relative to other techniques is that the method is a perturbative one, since the deflection of the crack is accomplished by altering the stress field at the crack tip. Thus, externally induced oscillations can potentially mask intrinsic, time dependent effects.

3.4. Measurements of heat generation and the temperature rise near a crack

As fracture occurs, a moving crack transforms the elastic energy stored in the elastic field of a material to either kinetic energy, the breaking of bonds or to heat. Two basic types of measurements have been performed to measure the heat that is generated by a crack. The most straightforward method has been to place small temperature sensors at a given distance from the path of a crack and measure the temperature rise in the material as a function of time after fracture has occurred. Since the time scale of fracture is orders of magnitude shorter (~ 100–$300\,\mu s$) than the typical thermal diffusion times within the material, the problem can be approximated by assuming that an instantaneous planar heat source is created along the fracture plane. Assuming that the radiative losses are negligible over the period of measurement, the measured temperature variation with time at a single point can be fit to the solution of the heat conduction equation. Measurements of this sort were performed in Polymethylmethacrylate (PMMA) by Doll [67] in glass by Weichert [68] and in steel by Zimmerman et al. [69]. The precision of these measurements varied between 6 and 20%. In addition to the heat radiated from a moving crack, it is possible, with the assumption of a black-body radiation spectrum, to estimate of the temperature rise in the vicinity of the crack tip by the use of IR detectors. Such experiments have been conducted by Fuller et al. [70] in careful experiments on cracks propagating in PMMA and polystyrene (PS) and in AISI 4340 carbon steel [71] and Beta-C titanium [72] by Rosakis and Zehnder. In these experiments, data were obtained by focusing the infrared radiation emitted by cracks moving at different velocities into an indium–antimonide infrared detector. The temperature of the crack was then obtained using the assumption that the emission spectrum of a crack corresponds to a black body spectrum.

The assumption of a black body spectrum may be suspect. This assumption can be checked in molecular dynamic simulations of fracture in a crystalline material, where, at least in the immediate vicinity of the tip, it does not appear to be even approximately true. As will be shown in Section 6.6 the energy excited by a moving crack is taken up by discrete phonon frequencies and there is no sign that these modes are being rapidly thermalized.

Both the measurement of emitted heat and the local temperature of the crack tip can be correlated with the crack's velocity. The results of these measurements will be discussed in the next section.

3.5. Acoustic emissions of cracks

Measurement of acoustic emissions has long been used as a tool to detect either the onset or precursors to fracture, where the existence, frequency of events and event locations can be measured (see e.g. [73]). These techniques, however, have not been used extensively in dynamic fracture experiments since, generally, both the existence and location of a crack are determined

more accurately by other methods. On the other hand, monitoring the acoustic emissions of a moving crack is a sensitive method to determine whether changes in the stress field are occurring during fracture, because any rapid changes will invariably broadcast stress waves.

Most acoustic emissions used for flaw detection and fracture onset measurements have utilized arrays of resonant acoustic transducers since the advantage of their high relative sensitivity more than offsets the loss of information of the spectral content of the signal. In dynamic fracture, we shall see that the spectral content of the acoustic signal broadcast by a moving crack carries important information. Therefore, broadband transducers should be used together with relatively high amplification to offset the transducers' lack of sensitivity. Gross et al. [74] used calibrated NIST-type transducers [75] with a flat response from 0.1 to 1 MHz, and Boudet et al. [76,77] used relatively broadband "pinducer" probes to monitor acoustic emissions during rapid fracture, and correlate them with velocity and fracture surface measurements. In both experiments, although deflections of the two dimensional sample normal to its surface were measured, the probe was sensitive to both longitudinal and shear waves due to mode conversion [78]. In the experiments by Gross et al., the acoustic probes were calibrated for shear waves so that a quantitative estimate of the amount of acoustic energy released by the crack could be obtained.

4. Phenomenology of dynamic fracture

4.1. Comparisons of theory and experiment

How do the predictions of linear elastic fracture mechanics compare with experimental measurements? As long as the basic assumptions of fracture mechanics hold, the theory is quite successful in predicting both the motion of a crack and the behavior of the stress field throughout the medium. Once these assumptions break down, we will see that the linear theory loses its predictive power.

Fracture mechanics has been highly successful in predicting the value of the stress intensity factor at the tip of both stationary and moving cracks for both static and dynamically applied loads. An example is work by Kim [79] where the measured transient behavior of the stress intensity factor was compared quantitatively to the predictions of Eq. (112). In this experiment, step function loading was applied to the crack faces in a sheet of Homalite-100 that was large enough to approximate an infinite medium. The stress intensity factor was measured optically, using a method developed by Kim where the relation of the transmitted light through the crack tip to the stress intensity factor is used. Results of the experiment compared well with the calculated time dependence of the stress intensity factor [7].

Experiments on crack arrest by Vu et al. in polymethylmethacrylate (PMMA) [80] indicated similar agreement with theoretical predictions of the transient relaxation of the stress field within the medium. In these experiments, strain gauges, with a temporal resolution of $\sim 1\,\mu s$, were placed throughout the sample and were used to measure the temporal behavior of the stress field surrounding a crack at times immediately following crack arrest. As predicted by Freund [7], the stress field at a point directly ahead (behind) the crack was seen to reach its equilibrium value (to within a few percent) as soon as the shear (Rayleigh) wavefront passed.
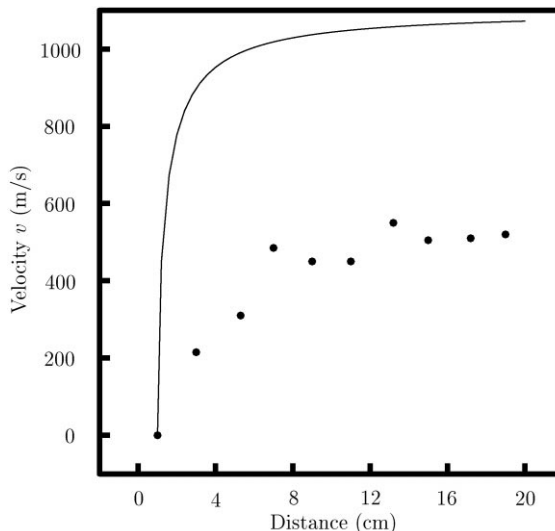
Fig. 11. Data of Kobayashi et al. [81] in PMMA. The data seem to indicate that cracks accelerate much more slowly than linear elastic theory predicts.

How do theory and experiment compare at high crack velocities? Experiments have often seemed to disagree with Eq. (147). One of the first experiments to test these predictions quantitatively was by Kobayashi et al. [81] in polymethylmethacrylate (PMMA). These data are reproduced in Fig. 11. Similar data have now been duplicated many times in a variety of brittle amorphous materials, with similar results.

Theory clearly predicts that if the fracture energy is not a strong function of velocity, a crack should smoothly accelerate from rest to the Rayleigh wave speed, c_R. As observed in the data of Kobayashi et al., although the crack initially accelerates rapidly, it becomes increasingly sluggish and finally reaches a final velocity well below the Rayleigh wave speed.

A brief look at Eq. (147) shows that there is a way out of this difficulty. One has only to suppose that the fracture energy Γ is a function of velocity. Specifying in Eq. (146) that l_0 is defined in terms of the minimal $\Gamma(0)$ at which crack propagation first occurs, one obtains instead of Eq. (147):

$$v = c_R(1 - \Gamma(v)l_0/\Gamma(0)l) . \tag{156}$$

By allowing the possibility that the fracture energy $\Gamma(v)$ increases rapidly as velocity increases, one can obtain almost any profile of velocity versus crack length desired. Indeed, one can view Eq. (156) as a way to extract the velocity dependence of fracture energy from experimental velocity measurements. On the other hand, if one is interested in the question of whether the theory is valid for all crack velocities, then this way out is rather unsatisfactory since it only demonstrates the theory's *plausibility*. Validation of the theory cannot be accomplished without an independent measurement of the fracture energy. Even with such validation, fracture mechanics provides no fundamental explanation of the *origin* of any measured velocity dependence of the fracture energy.

The first comparison of theory and experiment where the velocity dependence of fracture energy was explicitly taken into account was performed by Bergqvist [60]. He performed a series of beautiful experiments on crack arrest in PMMA which afforded direct comparison of calculated energy release rates with experiment for crack velocities below $0.2c_R$ ($< 200\,\text{m/s}$). In these experiments $50 \times 20\,\text{cm}$ samples were loaded by the application of constant stress on opposing boundaries. After fracture initiation, a high speed camera in streak mode was used to obtain a continuous record of the crack tip location with a temporal resolution of about $1\,\mu\text{s}$. To compare the velocity data to theory, Bergqvist used independent measurements of the fracture energy of PMMA as a function of the crack's velocity that were obtained in a strip geometry. By equating the measured value of the fracture energy to the calculated value of the energy release rate, he predicted values of the crack velocity. Comparison of the predicted and measured velocities showed agreement of the two to within 10%. As the main goal of the experiments was to investigate crack arrest, comparisons between theory and experiment for velocities higher than $0.2c_R$ were not attempted.

Sharon and Fineberg [82] have also performed such a comparison between theory and experiment for PMMA. To accomplish it, they first performed an independent measurement of the fracture energy of a crack by the use of the strip geometry. An additional series of experiments was then carried out in $40 \times 40\,\text{cm}$ samples, set up as in case 2 of Section 2.8.4. The velocity measurements in this set of experiments were then input into Eq. (156) and the derived values of $\Gamma(v)$ thus obtained were then compared to the direct measurements. The results of these experiments are shown in Fig. 12.

As in the experiments of Bergqvist, the data agree with Eq. (156) the theory for low velocities, less than about $400\,\text{m/s} \sim 0.4c_R$. Above this velocity there is a sharp divergence between observed and predicted values of $\Gamma(v)$. The reasons for this divergence, as we will see, are due to the growth of the process zone around the crack tip to a scale where it invalidates the assumptions of fracture mechanics in the samples used.
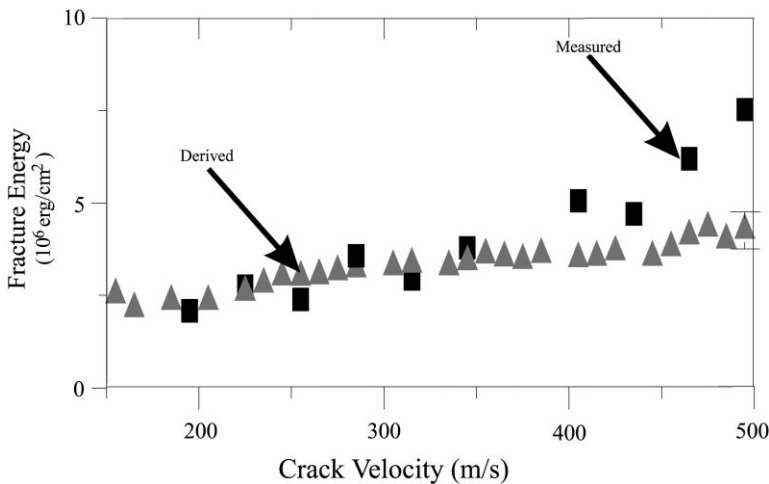

Fig. 12. A comparison of directly measured values of the velocity dependence of the fracture energy, $\Gamma(v)$, in PMMA with values predicted by fracture mechanics from Eq. (156), [83]. Note the good agreement until velocities of approximately $400\,\text{m/s} \sim 0.4c_R$.

Table 3
The maximal crack velocities observed in a number of brittle materials

Material	v_{max}/c_R
LiFl	0.63 [84]
Rolled tungsten	0.85 [85]
Single-crystal tungsten	0.88 [86]
MgO	0.88 [85]
Weak interface PMMA	0.9
Grooved PMMA	0.8
Glass	0.47–0.66
PMMA	0.58–0.62
Homalite	0.33–0.41

4.1.1. The limiting velocity of a crack

An additional, rather robust, theoretical prediction is that of the limiting velocity of a crack. Eq. (144) predicts that, barring divergent behavior of Γ as a function of v, a crack should accelerate until asymptotically arriving at the Rayleigh wave speed, c_R. As Table 3 indicates, in *amorphous* materials such as PMMA and glass, the maximal observed velocity of a crack barely exceeds about 1/2 of the predicted value. On the other hand, in strongly anisotropic materials such as LiF [84] tungsten [86,85] and MgO [85], a running crack indeed attains up to 90% of the predicted asymptotic velocity as cleavage through a weak plane occurs.

Is strong anisotropy necessary to attain the limiting velocity of a crack? An interesting experiment by Washabaugh and Knauss [87] indicates that this may indeed be the case. In this experiment, plates of PMMA were first fractured and then rehealed to form a preferred plane in the material that was substantially weaker than the material on either sides of it. Although the interface did weaken the PMMA, the re-healed material used still had between 40 and 70% of the strength of the virgin material. Fracture was performed by impulsively loading the faces of an initial "seed" crack by means of the electromagnetic loading technique first introduced by Ravi-Chandar and Knauss. Using an interferometer together with a high-speed rotating mirror camera, interferograms of the crack tip were recorded at 20 μs intervals. In this way, the crack's maximum velocity was determined and velocities of up to $0.9c_R$ were observed. Similar velocities were also observed in PMMA which was weakened by drilling a line of holes spaced 0.5 mm apart across the sample. The authors noted evidence of non-steady crack propagation suggestive of a "jerking accelerating-decelerating" process in both virgin PMMA and the re-healed material but with the severity of the uneven motion greatly reduced in the latter case.

In the experiments performed with the re-healed material, Washabaugh and Knauss noted that none of the cracks propagating along the weakened interfaces produced branches beyond the point of fracture initiation. The same type of behavior takes place in strongly anisotropic crystalline materials. Field et al. [85] noted that in experiments on MgO and rolled tungsten (where the rolling in the preparation of tungsten induces a preferred orientation in the material) branching of a crack is suppressed until very high velocities. Thus, in strongly anisotropic materials (either crystalline or artificially weakened materials), where microscopic crack branching is inhibited, cracks approach
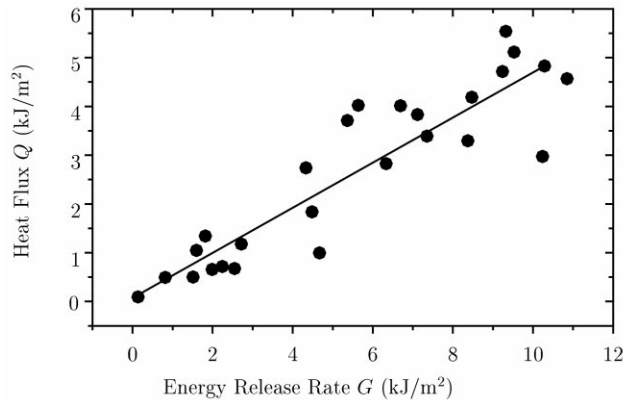
Fig. 13. A comparison of the energy release rate G, with the measured heat flux Q (from Doll [88]) in PMMA. 50–60% of the energy flowing into the tip of a crack in PMMA ends up as heat in the immediate region of the crack's tip.

the predicted limiting velocity. This fact is an important verification of claims we will later make about the consequences of dynamic instabilities for isotropic materials.

4.2. Phenomena outside of the theory

We will now briefly mention some of the phenomena that occur in fast fracture that lie outside the predictive power of linear elastic fracture mechanics.

4.2.1. The heat dissipated by fracture

We described in Section 3.4 the methods used to measure heat generated by a running crack. These heat flow measurements were then correlated with simultaneous velocity measurements in PMMA by Doll and Zimmerman et al. [67,69] in glass by Weichert et al. [68] and in steel by Zimmerman et al. [69]. Results of these experiments showed that heating accounted for most of the elastic energy driving the crack. The experiments of Doll and Weichert indicated that the measured heat flux accounts for 50–60% of the energy release, for crack velocities ranging from 0.1 to $0.6c_R$ (see Fig. 13). Later experiments by Zimmerman et al. for lower velocities 0.1 to $0.3c_R$ in both PMMA and steel estimated that the measured heat flux accounted for virtually the entire energy release.

Although these results indicate that nearly all of the elastic energy finds its way into the formation of heat, a central question is *where* this dissipation occurs within the sample. Is all of the energy converted to heat within the process zone or does the heating occur as elastic waves propagating away from the crack are attenuated within the sample? The answer to this question was obtained by real-time infrared visualization of the crack tip during propagation.

These experiments, first performed by Fuller et al. [70] on PMMA and polystyrene, indicated that temperatures at the crack tip in both materials were approximately constant as a function of the crack's velocity with a temperature rise of order 500 K. Similar temperature rises were recently measured in AISI 4340 carbon steel [71] and Beta-C titanium [72] by Zehnder et al. Besides the

large temperature rise (in PMMA and polystyrene the temperatures at the crack tip were well above the equilibrium melting temperature!) these experiments also established that, in PMMA, the *source* of the heating was within a few μm of the crack's path or well within the process zone, as defined by the material's yield stress. Thus, these experiments indicate that nearly all of the dissipation in the material occurs in the near vicinity of a crack. The mechanism for the heat release appears to be the extreme plastic deformation induced by the fracture process in the near vicinity of the tip.

The statement that nearly all of the dissipation occurs within the plastic zone is supported by the experiments of Kusy and Turner [89] in their investigation of the fracture energy of PMMA. These authors found that the fracture energy of high ($> 10^5$) molecular weight PMMA (the typical molecular weight of commercially available PMMA is order 10^6) can be over two orders of magnitude larger than the surface energy; i.e. the energy needed to break a unit area of bonds. This large increase in the fracture energy was explained in terms of plastic deformation of the polymer chains. Their model [89,90] predicts that below a molecular weight of about 10^5, no significant plastic deformation occurs in fracture and the fracture energy becomes comparable with the surface energy. These predictions were borne out by a series of careful experiments where long polymers were exposed to high energy radiation whose effect was to reduce systematically the mean molecular weight of the polymer as the exposure duration was increased. As a result of the radiation, the fracture energy of PMMA was observed to decrease by over two orders of magnitude as the molecular weight of the molecule was reduced from 10^5 to about 3×10^4.

How do the heat and temperature measurements of the process zone influence basic understanding of the fracture process? From the point of view of continuum fracture mechanics, the fracture energy is in any case an external input into the theory. Thus, neither the extreme temperature rise observed within the process zone nor the causes for this have any effect on the predictions of the theory. What is important for fracture theories is that the observed dissipation is *localized* within the process zone and not spread out throughout the medium. If the latter were to occur, the entire rationale behind the balance leading to Eq. (112) would be invalidated. In Section 5 we will demonstrate that in brittle amorphous materials the dissipation described above has a well-defined structure related to the dynamic behavior of a crack. Thus, although the fracture energy is a material dependent quantity which carries with it "baggage" such as plastic deformation within the process zone, the total fracture energy *observed* is related to the amount of microscopic surface actually created by the fracture process. The total surface created by the process will, in turn, be intimately related to instabilities that occur to a single crack as a function of the energy that it dissipates.

4.2.2. Analysis of fracture surfaces

There has been a great deal of work invested in the analysis of fracture surfaces, and the amount of literature on this subject is correspondingly large (see, for example, Ref. [91]). Much of the interest in this branch of engineering, called fractography, is concerned with the determination of the location of the onset of fracture of a given structure together with the probable cause for its failure. The visual inspection of a fracture surface is accomplished by using either optical or electron microscopes, depending on the scale needed for analysis. Although every fracture surface is different, the proven utility of fracture surface analysis in the determination of different fracture processes stems from the fact that, empirically, a close relation exists between the deterministic

dynamics of a crack and the fracture surface that it leaves behind. In many cases the *mechanisms* leading to characteristic surface features are not known, but the fact that these features are at all general is strong evidence that they are created by a deterministic process, independent of details of the loading or initial conditions (e.g. initial defect structure or distribution) of the object under study. It is one of the goals of the study of fracture to uncover these fundamental mechanisms and to understand their generality.

4.2.3. Profilometry

Besides the imaging of a fracture surface, it is often useful to measure its topography quantitatively. Depending on the required scale, there are various methods to perform measurements of the local fracture surface amplitude. For scales ranging from 1 to 100 μm commercial contact type scanning profilometers can be used to measure properties such as the rms roughness of a surface. Due to the tip size of the contact probe, however, surface features that are under 10 μm in size may not be properly resolved. To this end, specialized x–y contact [64,64] and optical [76] profilometers have been used. The study of fracture surfaces at submicron scales has recently been performed using both scanning tunneling and atomic force microscopy [92,93] where 1 nm resolution is attainable.

4.2.4. Mirror, mist, hackle

From many studies of fracture surfaces formed in brittle materials, it was found that the surface created by the process of dynamic fracture has a characteristic structure in brittle amorphous materials. This structure, called "mirror, mist, hackle", has been observed to occur in materials as diverse as glass and ceramics, noncrosslinked glassy polymers such as PMMA and crosslinked glassy polymers such as Homalite 100, polystyrene and epoxies. Inspection of the fracture surface in a given experiment shows that near the location of fracture onset, the fracture surface appears smooth and shiny, and is thereby called the "mirror" region. As a crack progresses further, the fracture surface becomes cloudy in appearance, and is referred to as "mist". As the "generic" crack progresses still further, its surface progressively roughens. When it becomes extremely rough, the fracture surface is said to be in the "hackle" region.

4.2.5. Microscopic crack branches

Is there any specific structure observed within these regions? In early studies of the fracture of glass rods, Johnson and Holloway [94], by progressive etching of the fracture surface in the "mist" region, demonstrated the existence of microscopic cracks that branch away from the main crack. Similar microscopic branched cracks ("micro-branches") were later observed by Hull [95] in polystyrene, and Ravi Chandar and Knauss [96] in Homalite 100 by visualizing the fracture surface in a direction normal to the faces of the fracture sample. Microscopic (< 100 μm) branched cracks have also been observed to result from the rapid fracture of brittle tool steel [97]. As we will discuss in Section 5, the formation and evolution of micro-branches are a major influence on the dynamics of a crack (Fig. 14).

4.2.6. Parabolic surface markings

In addition to the appearance of small branches in the mist regime, small parabolic markings as shown in Fig. 15 are commonly observed upon the fracture surface of amorphous materials. These
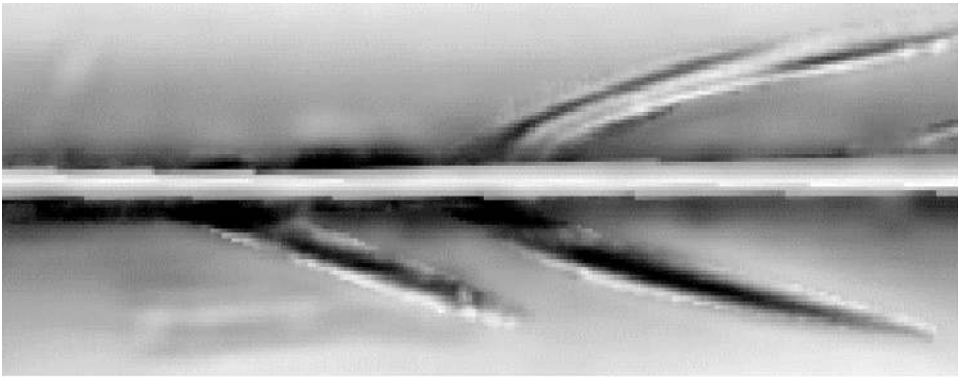
Fig. 14. A typical view of microscopic branches as observed in PMMA. The main crack has propagated from left to right along the center of the photograph. The arrow, indicating the propagation direction, is of length 125 μm.
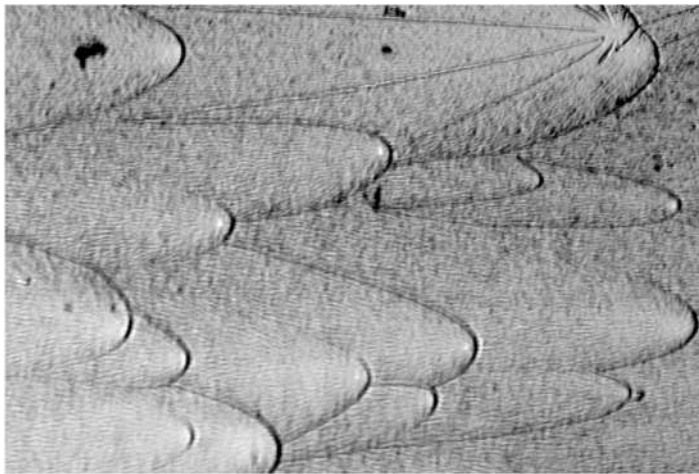

Fig. 15. Parabolic markings typically observed on the fracture surface of PMMA.

markings appear in all three fracture regimes and are interpreted as being the result of microscopic defects opening up ahead of the main crack front. To see how these markings come about, let us imagine a microscopic void situated directly ahead of a crack. The intense stress field, generated at the crack's tip, may cause the void to propagate some distance before the main crack catches up with it. The intersection of the main crack front with the front initiated by the void will then lead to the parabolic markings appearing on the fracture surface. As observed by Carlsson et al. [98], the number of the parabolic markings increases with the crack velocity. As the stress intensity factor increases with velocity, this observation is consistent with the above picture since an increasing
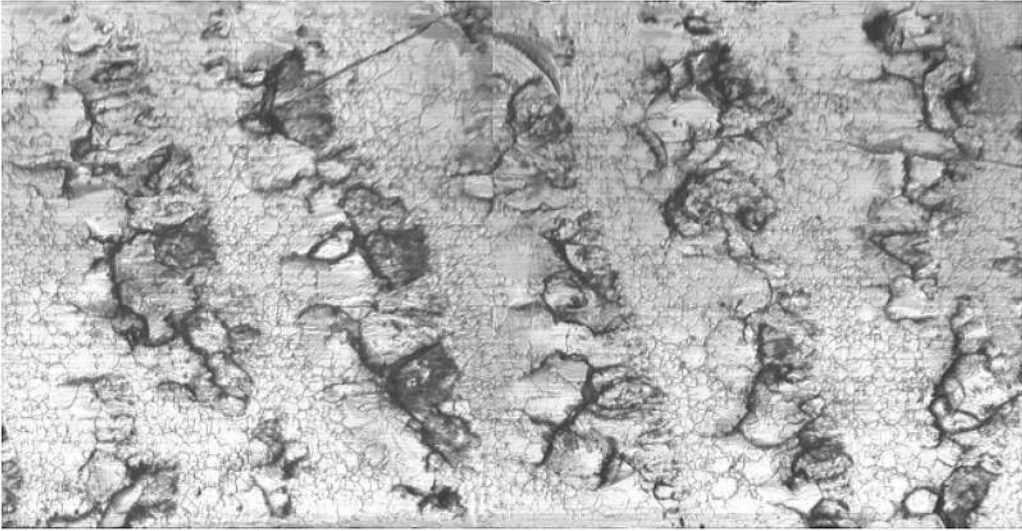
Fig. 16. A photograph of typical rib-like patterns observed on the fracture surface of PMMA. The distance between ribs is approximately 1 mm. On smaller scales parabolic markings can be discerned.

number of voids should be activated ahead of the crack tip as the stress at the tip increases. Shioya et al. found the depth of the parabolic markings in PMMA [99] to be approximately 1 μm and Gross [100] was able to measure small velocity fluctuations resulting from the interaction of the main crack with these voids (of order 10–25 m/s) in PMMA for velocities between 150 and 330 m/s which correlated with the increase in microvoid density observed by Carlsson et al. Ravi-Chandar et al. have recently completed a comprehensive study of the development of the parabolic markings as a function of the velocity of a crack for four polymers; PMMA, Homalite-100, Solithane-113 and polycarbonate [101]. As in the study by Carlsson, they find that the parabolic markings in all of these materials increase in density with increasing values of the stress intensity factor.

4.2.7. Patterns on the fracture surface

In the "mist" and "hackle" regions of many brittle polymers, rib-like patterns, as demonstrated in Fig. 16, on the fracture surface are commonly observed.

Similar patterns have been observed in polystyrene [95], PMMA [65], Solithane-113 and polycarbonate [101]. In these materials the typical distance between markings is on the order of 1 mm, so that they can easily be seen by eye.

In PMMA, where extensive work has been performed to characterize these patterns, the patterns initiate within the "mist" regime. Initially, the width of these structures is much less than the thickness of the sample, but the typical width of these structures increases with the crack velocity and eventually, within the "hackle" zone extend across the entire thickness of the sample [102]. These patterns are not smooth undulations along the fracture surface but, instead, are discrete bands of jagged cliff-like structures. As the crack velocity increases, these structures increase in height and exist up to the point where a crack undergoes macroscopic crack branching.

In PMMA, the spacing between ribs was found to be strongly related to the molecular weight of the monomers used to form the material. Kusy and Turner [89], by varying the exposure time to gamma-ray radiation, managed to control precisely the average molecular weight of their PMMA samples. The results of these experiments clearly showed that the rib spacing was a strongly increasing function of the mean molecular weight. The typical spacing was shown to increase by over two orders of magnitude as molecular weight was varied between 1×10^4 and 1×10^6. These authors also observed that the fracture energy is a strongly increasing function of the rib spacing.

4.2.8. Roughness of the fracture surface

Much recent effort has been directed to characterizing the fracture surface in terms of a "rough-ness" exponent. This idea was pioneered by Mandelbrot et al. [103] who measured the fracture surface of steel samples for a number of different heat treatments. They then demonstrated that the fracture surfaces obtained were scale-invariant objects with a self-affine character. Later studies [104–106] of aluminum alloys, steel, ceramics and concrete indicated that the local height, z, of the fracture surface scales as $z \sim l^\zeta$ where l is the scale of observation within the fracture "plane" and z the local height of the fracture surface. These studies indicated that for both quasistatic and dynamic fracture a "universal" roughness exponent of $\zeta \sim 0.8$ is obtained for values of l greater than a material-dependent scale, ξ_c [107,93]. For values of $l < \xi_c$, a different roughness exponent of $\zeta \sim 0.5$ is observed [92]. This latter has been interpreted as the result of crack front pinning by microscopic material inhomogeneities in very slow fracture [108].

In many of the experiments where the roughness of the fracture surface was measured, the typical scales where scaling behavior was observed were many orders of magnitude smaller that the typical sample size. For example, the largest scale observed in recent measurements performed on soda-lime glass [93] was order 0.1 μm (or well within the "mirror" regime). Thus, in the context of continuum dynamic fracture, this roughness does not constitute a departure from "straight-line" propagation. It is conceivable, though, that the scaling structure observed may effect the observed value of the fracture energy. To this date, no systematic measurements of how the roughness scales with the velocity of a crack (at velocities of interest to dynamic fracture) have been performed. Although it is known that the rms surface roughness increases with the velocity of a crack within the "mist" and "hackle" regions in PMMA [64,76], Homalite-100 [109], and crystals when cleaved at high velocities [85,110] it is not known whether the above scaling persists in this regime.

The scales at which self-affine behavior of the fracture surface has been measured in these experiments are, in general, well within the process zone. As a crack accelerates, however, the surface structure within the "mist" and "hackle" regimes may, depending on the overall system size, become larger than scales at which the singular contribution to the stress field in the medium is dominant. At this point the structure within the fracture surface may no longer be "swallowed up" within the process zone, and the description of the dynamics of a crack goes beyond the realm of linear fracture mechanics.

4.2.9. The velocity dependence of the fracture energy

The fracture energy, or the energy needed to create a unit fracture surface, is of tremendous practical and fundamental importance. For this reason, measurements of the fracture energy, Γ, as a function of the velocity of a crack have been performed for many different materials. The most common way to perform these measurements is by use of the method of caustics. In single crystals
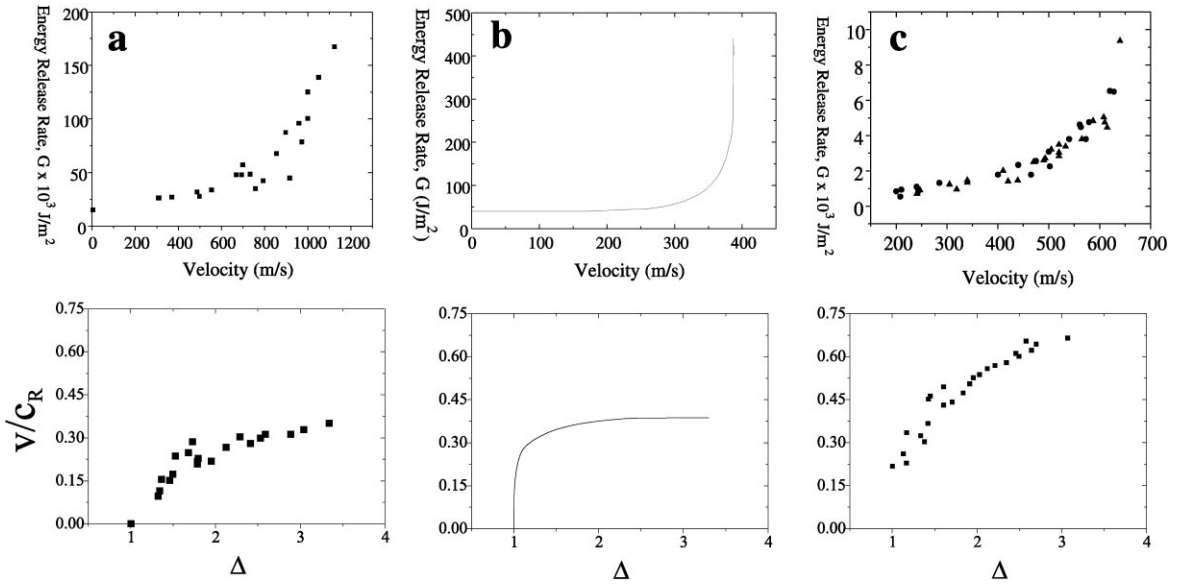
Fig. 17. The velocity dependence of the fracture energy, $\Gamma(v)$ for (a) AISI 4340 steel from [53], (b) Homalite-100 from [112], and (c) PMMA from [113]. The data are also shown in dimensionless form, with the velocity scaled by the shear wave speed displayed versus the dimensionless measure of loading $\Delta = K_{\mathrm{I}}/K_{\mathrm{c}}$.

measured values of the fracture energy necessary to initiate crystal cleavage agree well with theoretical predictions [20]. In amorphous or polycrystalline materials, however, experiments indicate that $\Gamma(v)$ is a sharply increasing function of a crack's velocity, whose form is only empirically known. Most of the fracture energy, as we have already seen, eventually ends up as heat within the process zone. Additional sinks for this energy are the acoustic energy radiated from the crack (i.e. the kinetic energy within the material) and "fracto-emission" or the emission of photons from excited molecules along the fracture surface [111].

In Fig. 17 we present some typical measurements of fracture energy Γ versus crack velocity v for PMMA, Homalite-100 and AISI 4340 steel. We also present the data in dimensionless form. The variable Δ is a dimensionless measure of loading, equal to $K_{\mathrm{I}}/K_{\mathrm{Ic}} = \sqrt{G/G_{\mathrm{c}}}$, the stress intensity factor divided by the critical value at which fracture first occurs. Velocity is made dimensionless by dividing through by the Rayleigh wave speed c_{R}. We will present relationships between fracture energy and velocity in this same dimensionless form throughout the rest of this paper; see Figs. 40, 42, 47 and 49. A common feature in all of these, quite different, materials is the sharp rise that occurs in Γ as the crack velocity increases. In the case of steels, the rise in fracture energy can be explained by modeling the process zone as a plastically deforming region, and calculating the change in plastic dissipation as a function of crack velocity. These calculations are described by Freund [7]. However, in brittle amorphous materials, such as PMMA and Homalite, dislocations are immobile, and there is no reason to believe that the classical theory of plasticity can be used to describe deformations near the crack tip. The origin of enhanced dissipation in these materials must therefore be sought in other mechanisms.
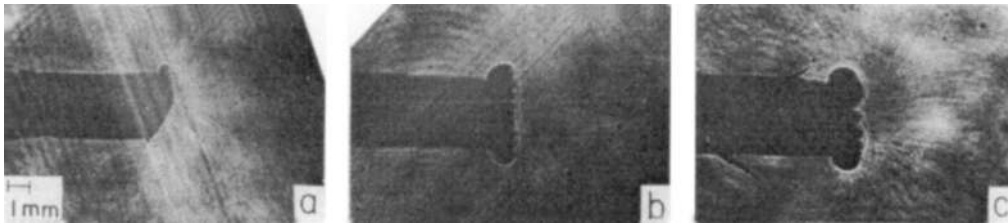
Fig. 18. High-speed photographs of the tip of a moving crack in Homalite 100 (from [109]). The photographs were taken in the (a) mirror, (b) mist and (c) hackle regimes. Note that in the mirror region a single crack tip develops. In the mist regime small caustics, indicative of multiple crack tips, develop at either side of the crack tip. In the hackle regime the strength of the multiple caustics increases, and small crack branches behind the crack tip are in evidence.

4.2.10. The observation of a multiple-crack front

A view of fracture, suggested by experiments performed by Ravi-Chandar and Knauss [109], is that dynamic fracture is not due to the propagation of a single crack but is due to the formation and coalescence of microscopic voids ahead of a crack front. This view is based on a series of experiments on Homalite-100. Fracture was induced via the electromagnetic loading technique described in 3.1.3 where a trapezoidal pressure profile with a 25 μs rise time and 150 μs duration was applied to the faces of a seed crack. The Homalite sheet used was large enough so that the first reflected waves from the sample boundaries would not interact with the crack throughout the 150 μs duration of the experiment. Within the mist and hackle regions, a front of multiple microscopic parallel cracks instead of a single crack was observed.

In the mirror region, as shown in Fig. 18, the authors noted that cracks tended to propagate within a single crack plane. As the crack propagated within the mist region (Fig. 18b) caustics due to the formation of multiple crack tips were observed. These increased in intensity within the hackle regime (Fig. 18c) as the secondary cracks increased in size. The authors then went on to show that the stress intensity factor, measured by means of the method of caustics, was correlated with the depth of the parabolic markings observed at the same spatial location (see Fig. 15). The authors interpreted the multiple micro-cracks, whose caustics were observed in the high speed photographs, as being due to the nucleation of microscopic material flaws, whose traces were indicated by the parabolic markings left on the fracture surface. These voids, as had been proposed earlier by Broberg [114], are nucleated by the high stresses ahead of the crack front. In this picture the motion of the crack is then dictated by the interactions between these growing flaws and the front.

4.2.11. Microscopic and macroscopic crack branching

The question of when a crack has branched is rather a subtle one. If a crack begins to emit branches that remain small enough relative to the size of the sample, they can simply be viewed as part of the process zone. As shown in Fig. 18, above a certain energy flux, cracks in the brittle plastic Homalite-100 are actually composed of multiple microscopic cracks propagating in unison. Section 4.2.2 shows that microscopic crack branches are observed in a variety of different materials within the "mist" and "hackle" zones. However, in samples of any given size, an increase in size of microbranches with energy release rate, G, must eventually bring the process zone to a size that invalidates the assumptions of fracture mechanics.

When the flow of energy to the tip of a crack increases sufficiently, the crack branches into two or more macroscopic cracks. Once a crack bifurcates, single crack models are, of course, no longer valid. Therefore, a theory describing a single crack can, at best, provide a criterion for when crack branching occurs. A number of such criteria for the onset of crack branching have been proposed. The criterion due to Yoffe and extremal energy density criteria have already been mentioned in Section 2.8.4. These criteria all suffer from the common problem that the velocities predicted for the onset of branching are much too high. Additional criteria such as postulating a critical value of the stress intensity factor, have not been consistent with experiments [41,115] since measurements at the point of branching show considerable variation of the stress intensity factor K_I. Eshelby [116] suggested that a crack should branch when the energy going into the creation of a single propagating crack is enough to support two single cracks. One problem with this criterion is that if Γ were not a strongly increasing function of v, once branching occurred, one would necessarily observe a large decrease in the branch velocities relative to the single crack velocity preceding the branching event. In glass, however, post branching velocities are either observed not to decrease at all [117] or at most undergo a decrease of $\sim 10\%$ [66]. If Γ is a strongly varying function of v, as presented in Fig. 17, the slight drops in velocity after branching would not necessarily present a problem. At any rate, the Eshelby criterion is certainly a necessary one for crack branching. The fact that a critical value for the stress intensity factor does not seem to work would preclude the use of the Eshelby criterion as a sufficient condition.

Experimentally, there seems to be no basis for a critical velocity for macroscopic crack branching, as predicted by the Yoffe criterion. For example, experiments in glass [97] have yielded branching velocities between 0.18 and $0.35c_R$. In PMMA [118] branching velocities are consistently about $0.78c_R$, and in Homalite branching velocities between 0.34 to $0.53c_R$ have been observed [115]. When using data on branching velocities to examine intrinsic properties, one must ensure that branching occurred in a given experiment at locations that are far enough away from the lateral boundaries to ensure that the system is effectively "infinite" in extent. Otherwise, studies by Ravi-Chandar and Knauss [119] have shown that branching can be induced by the arrival of waves generated at the onset of fracture and reflected at the lateral boundaries of the system back into the crack tip.

Although the existence of a well-defined criterion for the onset of branching is not apparent in experiments, the consistent values of branching angles that have been observed in many different materials suggest that there may be a degree of universality in the macroscopic branching process. The branching angles, as quoted in the literature, are generally determined by measurement of the tangent of a branched crack at distances of order a fraction of a millimeter from the crack tip. Angles of $10°$ in PMMA [118] and glass [94], $14°$ in Homalite, $15°$ in polycarbonate [41] and $\sim 18°$ in steel [97] have been reported for samples under pure uniaxial tension.

4.2.12. "Non-uniqueness" of the stress intensity factor

In an additional series of experiments on Homalite-100, Ravi-Chandar and Knauss [96] discovered another apparent discrepancy between theory and experiment. In these experiments, high-speed (5 µs between exposures) photographs of the caustic formed at the tip of a crack initiated by electromagnetic loading at high loading rates were performed. The velocity of the crack, as deduced from the position of the crack tip in the photographs, was then compared with the instantaneous value of the stress intensity factor, which was derived from the size of the caustic.

At low velocities (below $\sim 300\,\text{m/s} = 0.3c_{\text{R}}$) a change in the value of the stress intensity factor (e.g. as induced by a wave reflected from the boundaries) resulted in an "instantaneous" change in the crack's velocity, exactly as the theory predicts. On the other hand, at higher velocities (above $\sim 300\,\text{m/s}$) significant changes in the stress intensity factor produced no discernible corresponding change in the crack's velocity. These experiments have been interpreted as indicating that the stress intensity factor is not a unique function of crack velocity.

The puzzling questions that these experiments posed on the relation between fracture velocity and fracture energy interested us and many others in the field of dynamic fracture. In the next section we will provide an explanation for these questions that builds on this work.

5. Instabilities in isotropic amorphous materials

5.1. Introduction

Dally [112] spent many years studying dynamic fracture in amorphous polymers, and in steels. In summarizing these experiments, he concluded that

1. The proper way to characterize a dynamic fracture experiment is through two dimensionless numbers; the crack velocity divided by a wave speed, v/c, and the dynamic stress intensity factor divided by the stress intensity factor at onset, $K_{\text{I}}/K_{\text{Ic}}$, which is identical to the dimensionless parameter Δ used in characterizing our experiments and theories. The functional relation between these two numbers carries most of the dynamical information about fracture, and can be measured reproducibly for a wide variety of geometries and loading histories.
2. The energy needed for fracture of brittle amorphous materials increases sharply past a certain velocity, where the straight crack becomes unstable to frustrated branching events.

We will provide detailed experimental evidence for this point of view in what follows, and show that it allows one to bring together many apparently conflicting experimental and theoretical results.

When we began experiments on dynamic fracture of amorphous brittle materials there was a general perception that theory and experiment did not agree. Freund [7, pp. 37–38], specifically mentions in a short list of phenomena "not yet completely understood" the "apparent terminal crack speed well below the Rayleigh wave speed in glass and some other very brittle materials". In retrospect, the divergence between theory and experiment was not as great as it seemed. Unease with the results of theory arose from the expectation that motion of cracks should be predictable on the basis of linear elastic fracture mechanics alone. In a brittle material it seemed plausible that fracture energy should not vary much as a function of crack velocity, despite unambiguous experimental evidence that large variations in fact occurred. Thus, the apparent difficulty was that cracks did not accelerate to the expected limiting speed or obey expected equations of motion, while in fact the question needing an answer was why the fracture energy varied so strongly with crack velocity.

Besides the question of the terminal speed of a crack, we were bothered by the apparent lack of explanation of the many characteristics of brittle fracture, mentioned in the last section, which elastic fracture mechanics could not answer. No satisfactory answers were available for basic questions such as how and why structure arises on a fracture surface or why macroscopic
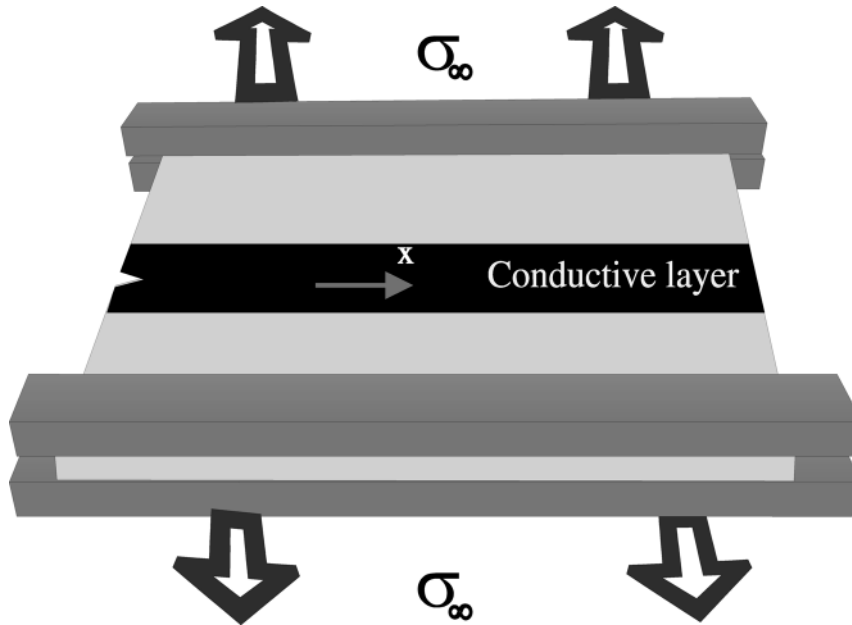
Fig. 19. A schematic view of a typical experimental system used for monitoring the velocity of a crack (from [102]). The center of the sample is coated with a thin ($\sim$ 30 nm wide) conductive coating. As a crack progresses across the sample, it cuts the conductive layer thereby increasing its resistance. The resistance change is converted to a voltage by means of a bridge circuit and the voltage is then digitized to 8–12 bit resolution at high rates (typically 10–20 MHz). This provides a "continuous" record of the position of the crack's tip with time.

branching occurs. We now have an answer to many of these questions which has arisen from experimental work on isotropic amorphous materials, and is complemented by theoretical and numerical work on crystals. The answer is incomplete since a compelling theory of amorphous materials is absent, as are decisive experiments in brittle crystals. However, many of the experimental and theoretical observations now fit neatly into a coherent scheme, which we now will endeavor to explain.

5.2. Experimental observations of instability in dynamic fracture

We began performing experiments in dynamic fracture [64] in the hopes of obtaining detailed dynamical records of crack motion, and correlating them with features left above and below the crack surface. We measured crack velocities using the conductive strip technique described in Section 3.3.2. A sketch of the experimental setup used in this type of velocity measurement is shown in Fig. 19.

With this measurement system it was possible to obtain high resolution measurements of the crack's velocity at $1/20 \, \mu s$ intervals for about 10 000 points throughout the duration of an experiment. The velocity resolutions obtained in the first experiments were order $\pm 25 \, m/s$. This resolution was later improved to about $\pm 5 \, m/s$ by analog differentiation of the signal [100,120] prior to digitization. Thus, it became possible to follow the long-time dynamics of a crack in
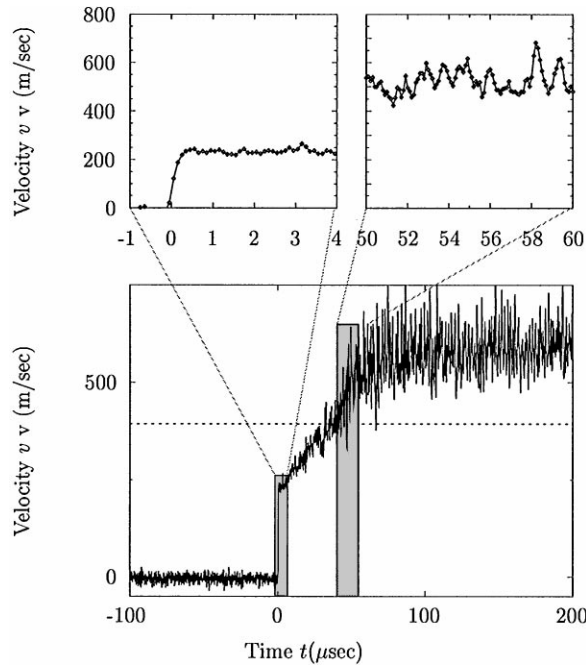
Fig. 20. A typical measurement of the velocity of a crack tip as a function of its length in PMMA. After an initial jump to about 150 m/s the crack accelerates smoothly up to a critical velocity v_c (dotted line). Beyond this velocity, strong oscillations in the instantaneous velocity of the crack develop and the mean acceleration of the crack slows.

considerable detail. In experiments on the fracture of PMMA a spatial resolution between measurements of order 0.2 mm was obtained [65,58]. An additional important advantage of this technique is that information can constantly be stored into buffers and discarded. The crack can be loaded very slowly, and when it finally moves, simply refrain from throwing away the contents of the buffer. Thus, the initial motion of a crack can be recorded, although it begins to move rapidly at an uncertain time.

These high-resolution measurements have yielded a rather different picture of a crack's dynamics than had previously been obtained. A typical measurement of a crack propagating in PMMA is shown in Fig. 20, where the velocity of a crack as a function of its length is presented. The figure highlights the following features of the crack's dynamics. The crack first accelerates abruptly, over a time of less than 1 μs, to a velocity on the order of 100–200 m/s. Beyond v_c the dynamics of the crack are no longer smooth, as rapid oscillations of the crack's velocity are apparent. As the crack's velocity increases, these oscillations increase in amplitude.

5.2.1. Initial velocity jump

It is natural to wonder whether the initial velocity jump seen in Fig. 20 is an intrinsic feature of the crack dynamics, or whether it is related to the initial conditions. The crack begins at rest, and the tip has ample time to become slightly blunted and make it difficult for the crack to begin moving. Hauch [121] performed experiments where the energy available per unit length decreased
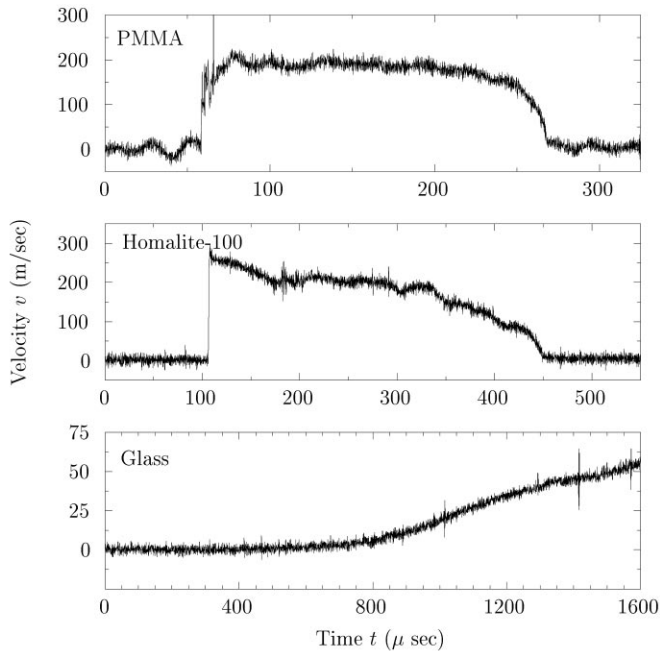
Fig. 21. Crack velocity versus time in geometries designed to produce gradual crack arrest. In PMMA and Homalite, cracks decelerate slowly towards zero velocity, on the scale of μs, while in glass, cracks are able to accelerate slowly from zero velocity, and travel stably at very low velocities. These data show that jumps in velocity from zero are not intrinsic properties of fracture dynamics in amorphous materials. Data of J. Hauch [121].

slowly through the length of the sample. We show some results from these experiments in Fig. 21. In both PMMA and Homalite-100, cracks decelerated gradually to zero velocity, strongly indicating that initial trapping rather than any intrinsic dynamical effect was responsible for the velocity jumps always seen when cracks begin to move. In the case of glass, it was possible to prepare very sharp seed cracks so that crack motion could initiate gradually, and the crack would then propagate steadily at velocities only a few percent of the Rayleigh wave speed. These data are also shown in Fig. 21.

5.2.2. Velocity oscillations beyond a critical velocity

Are the oscillations evident in Fig. 20 randomly fluctuating or periodic in time? A blow-up of a typical time series of velocity measurements of a crack moving within PMMA, after the onset of the oscillations, is shown in Fig. 22.

In the figure, it is apparent that, although the oscillations of the crack velocity are not perfectly periodic, a well-defined time scale exists. In PMMA the value of this scale is typically between 2 and 3 μs. Power spectra of experiments in which the crack accelerated throughout the experiment indicate that the location of the peak in the frequency domain is constant despite changes of up to 60% of the mean velocity [65].

Evidence for the existence of a *critical* velocity for the onset of the oscillations is presented in Figs. 23 and 24. The data presented in the figure were obtained by plotting the velocity at which the
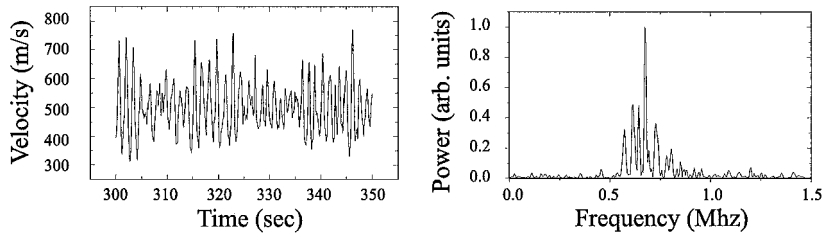
Fig. 22. Measurements of the velocity of a crack propagating in PMMA as a function of time (upper). The crack is propagating in steady-state above v_c. The corresponding power spectrum is shown in the lower plot. Note the existence of a well-defined time scale (from [122]).
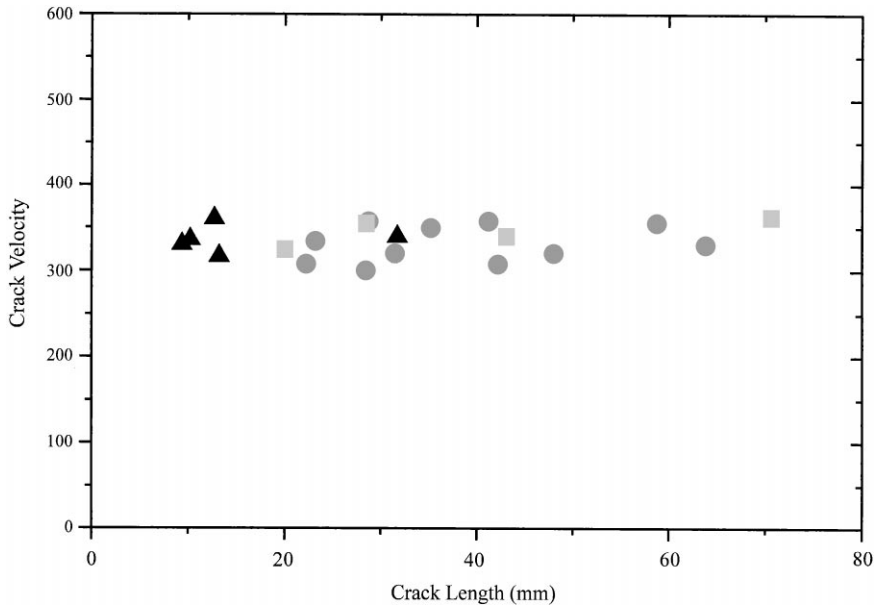

Fig. 23. Critical velocity as a function of the crack length at the moment of appearance of surface structure. Triangles, 1.6 mm wide extruded PMMA surrounded by air; circles, 3.2 mm wide cell-cast PMMA surrounded by air; squares, 3.2 mm wide cell-cast PMMA surrounded by helium gas (data from [65]).
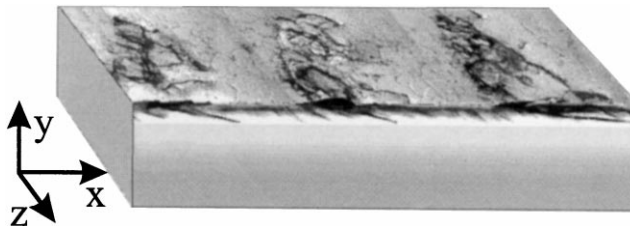

Fig. 24. Geometry of the fracture instability. The crack travels from left to right, creating a ribbed structure on the fracture surface, the x–z plane, and microbranches beneath it, in PMMA.
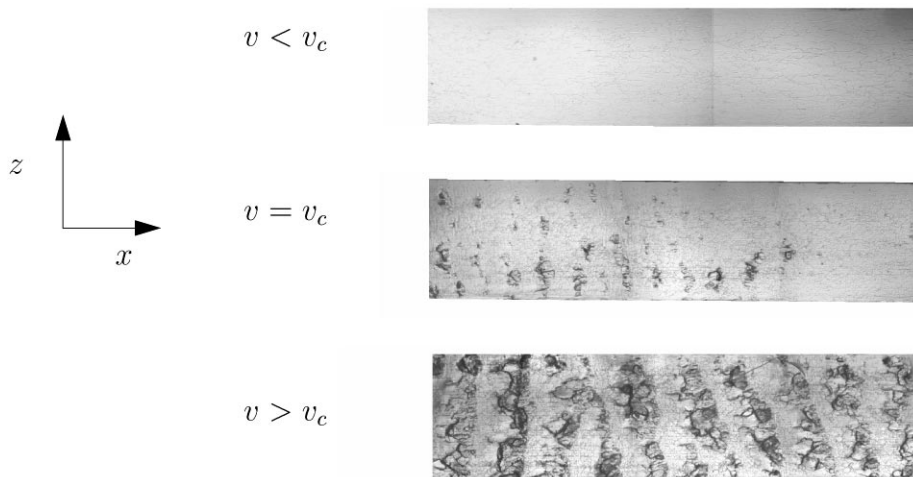
Fig. 25. Photographs of typical fracture surfaces in PMMA for $v < v_c$ (upper left), $v \sim v_c$ (upper right) and $v > v_c$ (lower figure). The photographs are all to scale where the width of the surfaces shown is 3 mm. Note that the pattern starts to develop in the vicinity of v_c (from [122]).

first deviation from a flat fracture surface was obtained [65]. As the value of v_c obtained for PMMA was suspiciously close to the speed of sound in air, experiments were also performed in helium gas (where the sound speed is $965 \, \text{m/s}$) where no discernible change in the value of v_c was obtained. Experiments have since indicated that v_c is independent of sample geometry, sample thickness, applied stress, and the acceleration rate of as the crack. Whenever, in PMMA, the critical steady-state velocity of $0.36c_R$ is surpassed, both oscillations in the crack velocity and an increase in the fracture surface area result.

5.2.3. The creation of surface structure via the instability

As mentioned previously, at high fracture velocities characteristic surface features are observed along the fracture surface of brittle polymers. At low velocities, on the other hand, the characteristic featureless "mirror" fracture surface is obtained. How does the fracture surface structure relate to the dynamical behavior of the crack that was described above? In Fig. 25 typical photographs of the fracture surface in PMMA are presented for values of $v < v_c$, $v \sim v_c$, and $v > v_c$. From the figure it is evident that the surface structure appears in the near vicinity of v_c. Profilometer [65] measurements were performed to map out the topology of the fracture surface. These were then correlated with measurements of the crack velocity taken when the fracture surfaces were formed. As Fig. 25 indicates, in the near vicinity of v_c structure starts to appear. Initially, the surface structure is apparent on only a relatively small amount of the fracture surface. In order to characterize the amplitude of this structure, the average height of the points *not* found in the mirror-like regions within the fracture surface was plotted as a function of the mean velocity of the crack. This plot is reproduced in Fig. 26. The following features are evident in the figure.
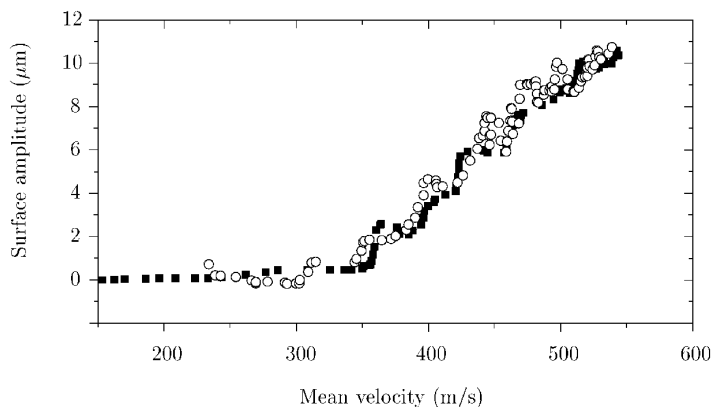
Fig. 26. The rms value of the surface height (obtained as explained in the text) as a function of the mean crack velocity in PMMA. The different symbols indicate experiments performed with different stresses and sample geometries (from Ref. [65]).

- At $v_c = 0.36c_R$, in PMMA, a sharp, well-defined transition occurs where surface structure is created.
- The surface structure formed is a well-defined, monotonically increasing function of the mean velocity of the crack.
- Both the transition point and functional form of the graph are independent of the details (e.g. initial and boundary conditions) used in the experiment, and are therefore *intrinsic* to the fracture process.

The dependence of the rms surface deviations with the mean velocity has also been measured over a larger range of velocities in PMMA by Boudet et al. [76,77]. These authors have measured the pure rms deviations of the surface (without accounting specially for the mirror-like regions as described above). Qualitatively, these latter measurements agree with those in Fig. 26 although, in the region of the transition the data look quantitatively different, although it is reasonable to assume that the difference is due to the fact that a pure rms calculation of the data gives little weight to the areas where the fracture surface is non-trivial, since, for $v \sim v_c$ the mirror-like regions dominate the fracture surface.

Fineberg et al. [64,65] also measured the cross-correlation between the local surface structure and the instantaneous measurements of the velocity. The two types of measurements were compared along the faces of the sample, where the local velocity of the crack was, in essence, measured. The cross-correlation function obtained revealed the temporal oscillations at the 2–3 µs scale observed in the velocity measurements, although the degree of correlation (about 0.3) was quite low. A higher degree of correlation (about 0.5–0.6) was later observed by Boudet et al. [77] between the fluctuating part of the velocity and acoustic emissions of a crack.

In summary, both the existence of a sharp critical velocity for the onset of oscillatory behavior of the crack together with the well-defined monotonic dependence of the surface structure created by the crack beyond v_c point to the existence of an instability of a moving crack beyond this critical velocity. The behavior of the system is not influenced either by the boundary or initial conditions

and is seen to be solely a function of the mean velocity of the crack, or, equivalently, the energy release rate. This indicates that the instability is intrinsic to the system and dynamical in nature. Although the quantitative measurements described above have been performed in PMMA, the similarities of the fracture surface formed in such diverse amorphous brittle materials as PMMA, glass and brittle ceramics suggest that the dynamical instability is not confined to this single material, but is a general instability of brittle fracture. In this section, we will describe additional experiments that will verify this conjecture. The following sections will describe both numerical calculations and analytical models where behavior bearing close resemblance to the experiments is observed.

5.2.4. Micro-branching as the instability mechanism

What is the mechanism that gives rise to the dynamic instability described above? An answer to this question was provided by experiments performed by Sharon et al. [58]. As detailed in Section 4.2.2, microscopic branches have been observed within the "mist" region in a variety of brittle materials ranging from PMMA to hardened steels. Sharon et al. analyzed these structures as a function of crack velocity. In Fig. 27 we show photographs of the transverse structure observed in PMMA for velocities prior to, at and beyond v_c.

As Fig. 27 indicates, below v_c no micro-branches are observed. At v_c, branches begin to appear and, as the mean velocity of the crack increases, the branches become both longer and more numerous. In Fig. 28 a the mean length of a microbranch is plotted as a function of the mean velocity of the crack. As in Fig. 26 we see that, although at a given crack length the size of micro-branches varies widely, the mean branch length of a micro-branch is a smooth, well-defined function of the mean velocity. As in the case of the surface amplitude, at $v = v_c$ there is a sharp transition from a state having no branches to a state where both the main crack and daughter branches are observed. As Fig. 29 indicates, the value of v_c can be measured quite reproducibly for a wide variety of initial conditions. Whether the experiment begins with a blunted seed crack that accelerates rapidly to high velocities, or with a long sharp crack that stabilizes at lower velocities, once v_c is attained, we find micro-branches appearing. Presumably, a critical energy flux to the tip is achieved at the same time as well, but we did not measure energy flux directly. The same value of v_c describes both the transition to micro-branches and the appearance of surface structure.

How does the appearance of micro-branches relate to the structure formed on the fracture surface? In Fig. 28 the mean microbranch length (a) as a function of the mean velocity is compared to the surface amplitude measurements (b). Although the two figures are markedly similar, the typical size of micro-branches, for a given velocity, is about 2 orders of magnitude larger than the scale of the surface structure. This indicates that the surface structure is a *result* of the micro-branching process. These measurements imply that the structure observed on the fracture surface is, essentially, the initial stage of a micro-branch which subsequently continues into the sample in a direction transverse to the fracture plane. This is illustrated in Fig. 24 where a section of the fracture surface is shown together with a cut that reveals the branched structure beneath it.

As Fig. 28c demonstrates, the increase in the size of the velocity fluctuations is also a direct result of the micro-branching instability. The fluctuations in the velocity can now be understood as follows. As a crack accelerates, the energy released from the potential energy that is stored in the surrounding material is channeled into the creation of new fracture surface (i.e. the two new faces created by the crack). When the velocity of the crack reaches v_c, the energy flowing into the crack
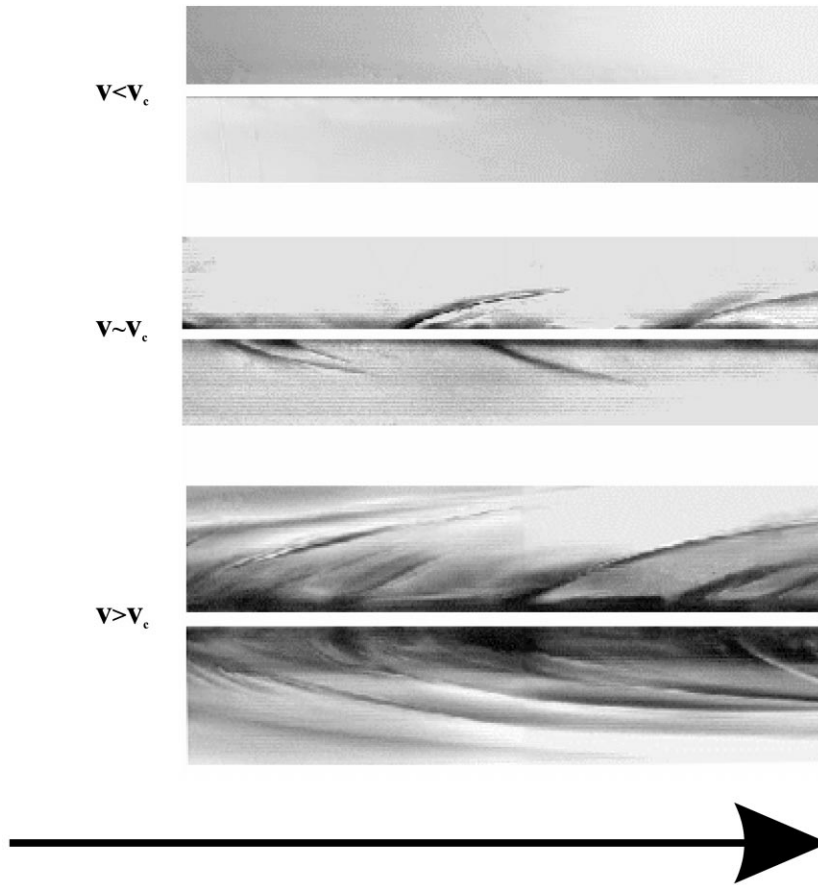
Fig. 27. Images of local crack branches in the x–y plane in PMMA. The arrow, of length 250 μm, indicates the direction of propagation. All figures are to scale with the path of the main crack in white. (top) $v < v_c$ (center) $v = 1.18v_c$ (bottom) $v = 1.45v_c$ (from [58]).

tip is now sub-divided between the main crack and its "daughters" which are formed by the branching events. As a result, less energy is directed into each crack and the velocity of the crack "ensemble" diminishes. The daughter cracks, which compete with the main crack, have a finite lifetime. This presumably occurs due to screening of the micro-branches by the main crack as it "outruns" them, because of its geometrical advantage of straight line propagation. The daughter cracks then die and the energy that had been diverted from the main crack now returns to it. This causes it to accelerate until, once again, the scenario repeats itself.

5.2.5. Micro-branch profiles

As Fig. 27 indicates, at a given mean velocity both the lengths and distances between consecutive micro-branches are broadly distributed. Sharon et al. [102] have shown that in PMMA, these quantities are characterized by log normal distributions whose mean and standard deviation values are linearly increasing functions of the mean crack velocity. As an example, the branch
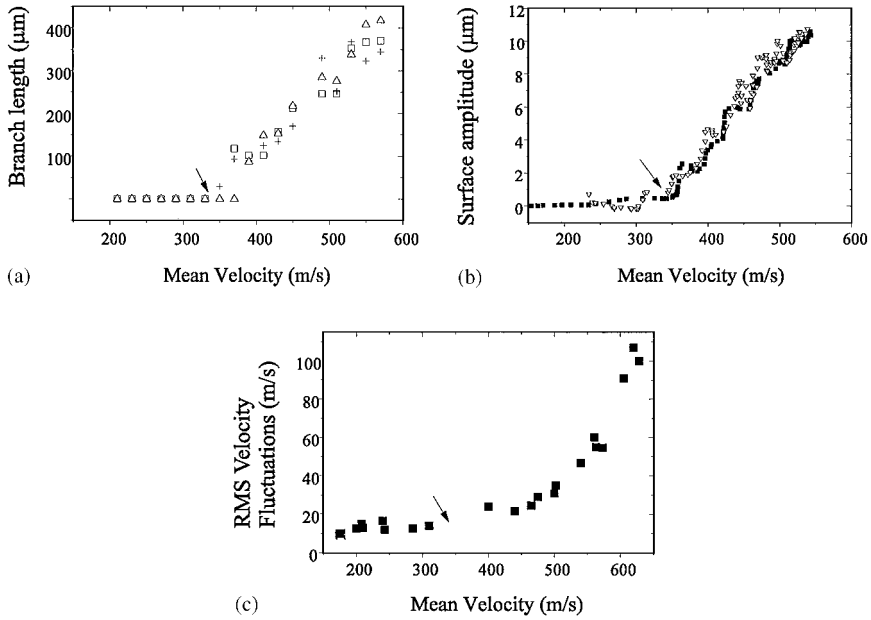
Fig. 28. (a) Mean branch length, (b) the rms value of the fracture surface amplitude, and (c) the rms velocity fluctuations as functions of the mean crack velocity, v, in PMMA. The arrows indicate the critical velocity of 340 m/s. The data in (a) and (b) were obtained by measurements of accelerating cracks in plates having different geometries and loading stresses. Note the nearly two order of magnitude difference in scales between the mean branch length and fracture surface amplitudes for the same values of v. The velocity fluctuation data were measured at steady-state velocities. Although velocity fluctuations are observed prior to v_c, a sharp rise in their amplitudes occurs beyond v_c (from [113,102]).
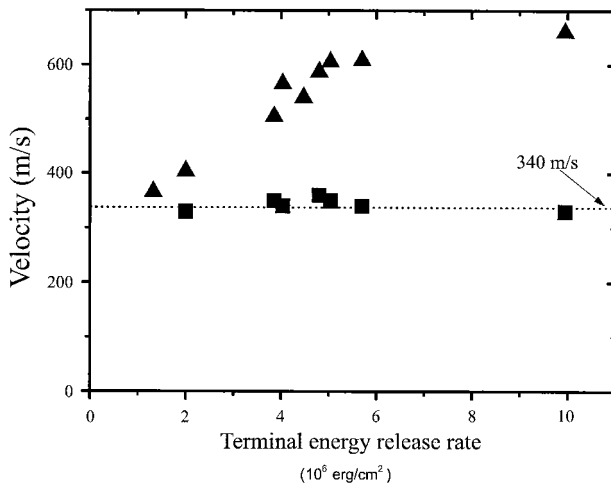

Fig. 29. The critical velocity for the appearance of micro-branches (squares) as a function of the energy density stored in the sample far to the right of the crack. For comparison, the terminal steady-state velocity (triangles) for the same experiments are shown. The data, taken from [102], are from experiments performed on PMMA in the strip geometry.
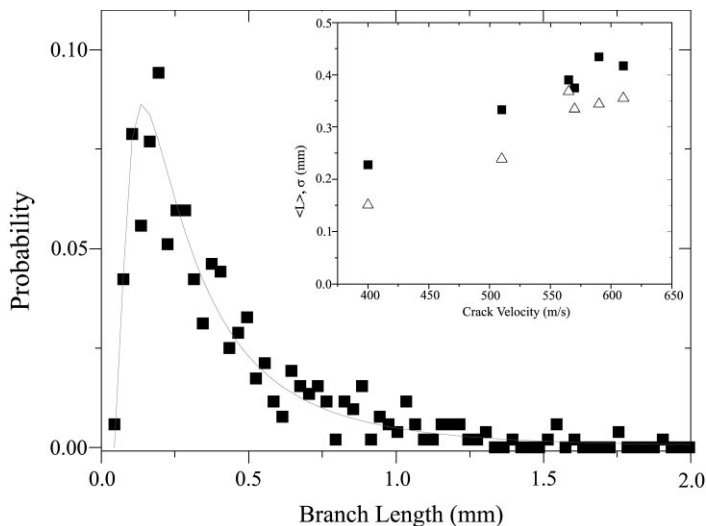
Fig. 30. A typical probability distribution of micro-branch lengths at a constant velocity of 585 m/s in PMMA. Note the fit to a log normal distribution (solid line) together with a minimum branch length of about 30 μm. (inset) the mean length, $\langle L \rangle$, (squares) and standard deviation (triangles) of the micro-branch length distributions in PMMA as a function of the mean crack velocity. Both increase linearly with the same 1 μs slope. Thus, the entire distribution scales linearly with the mean crack velocity (from [102]).

length distribution at a single velocity together with (inset) the dependence of the mean length and standard deviation of the length distributions with the mean crack velocity are shown in Fig. 30. Although it is obvious from the broad distributions above that the instantaneous lengths of micro-branches have a random character, one might want to look at the path that a given branch takes as it moves away from the main crack. Although a given branch may choose its length from a broad distribution, all micro-branches will propagate along an extremely well-defined trajectory. This is demonstrated in Fig. 31a, where the profiles of a number of micro-branches, formed at the same mean velocity, are superimposed and shown to trace out a well-defined function. Log–log plots of these trajectories in both PMMA and glass (Fig. 31b) show that the micro-branch profiles in both materials follow a power-law of the form

$$y = 0.2x^{0.7} \, , \tag{157}$$

where x and y are, respectively, the directions parallel and perpendicular to the direction of propagation of the main crack, and the origin is taken to be the point at which the micro-branch begins. Surprisingly, both glass and PMMA, two materials with greatly different microscopic structure, have nearly identical values for both the exponent and prefactor [83]. The nearly *identical* branch trajectories observed in Fig. 31 in such highly different materials suggests a universality of micro-branch profiles in brittle materials whose origin is dictated by the universal behavior of the stress field surrounding the crack tip. This conjecture is supported by the observations by Hull [95] of the same type of trajectory in polystyrene, where the micro-branch profiles were attributed to craze formation. Hull's analysis of these structures indicated that the branch profiles follow the trajectory of maximum tangential stress of the singular field created at
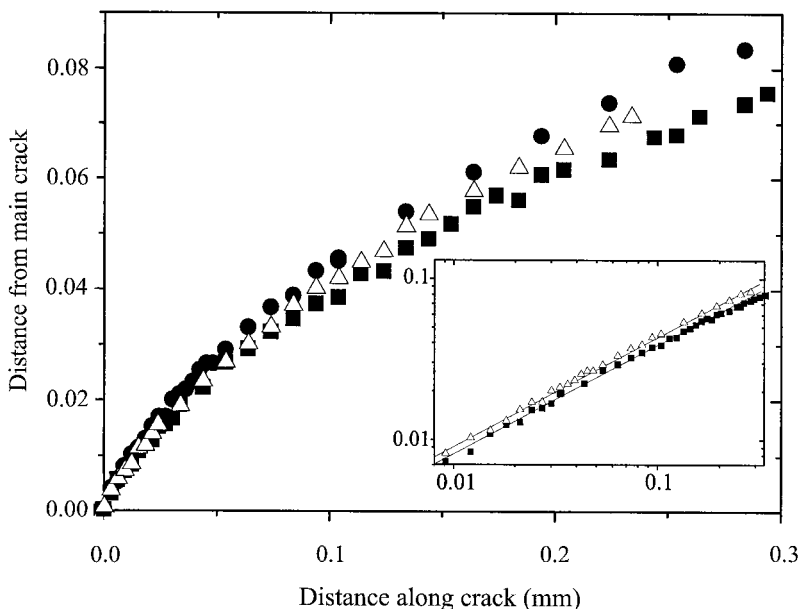
Fig. 31. Demonstration of the power-law scaling of micro-branch trajectories (from [102,83]). Shown are the mean micro-branch profile in PMMA for (squares) $v = 374\,\text{m/s}$ (triangles) $v = 407\,\text{m/s}$, and (circles) $v = 470\,\text{m/s}$. All profiles are described by the *same* function: $y = 0.2x^{0.7}$ where x and y are, respectively, the distance from the branching point, in mm, in the directions parallel and perpendicular to the direction of propagation of the main crack. (inset) log–log plot of micro-branch trajectories measured in PMMA (triangles) and glass (squares). Note that in both materials the micro-branch profiles are described by the same law.

the tip of the main crack. Using this criterion, this trajectory is also described by Parleton's [46] numerical calculation of the stress field of a single static crack.

How are micro-branches related to macroscopic branches? Let us examine the "branching angle" predicted by Eq. (157). The power-law form of Eq. (157) would predict a branching angle of $\pi/2$ as x approaches the point of branching. The maximum branching angle that has actually been observed was limited, experimentally, by diffraction. The largest angle observed by Sharon et al. [102] in PMMA was reported to be $30°$ at a $3\,\mu\text{m}$ distance from the bifurcation point. On the other hand, the values of the "branching angle" for *macroscopic* branching that are quoted in the literature are measured at distances typically of order $100–300\,\mu\text{m}$ from the branch onset. The angles that are tangent to the branch trajectory at these distances range from 15 to $11°$. This is in excellent agreement with the values of the branching angle (see Section 4.2.11) quoted in the literature for brittle materials ranging from polymers to hardened steel. These observations suggest that a smooth transition between microscopic and macroscopic crack branches occurs in brittle materials and that the characteristic features of crack branches exhibit, at these scales, a high degree of universality. If this picture is correct, the criterion for the formation of macroscopic crack branches simply coincides with the onset of the micro-branching instability.

5.2.6. The transition from 3D to 2D behavior

Although the origin of crack branching may now be understood to result from the micro-branching instability, a new question now arises: under what circumstances will a branched crack
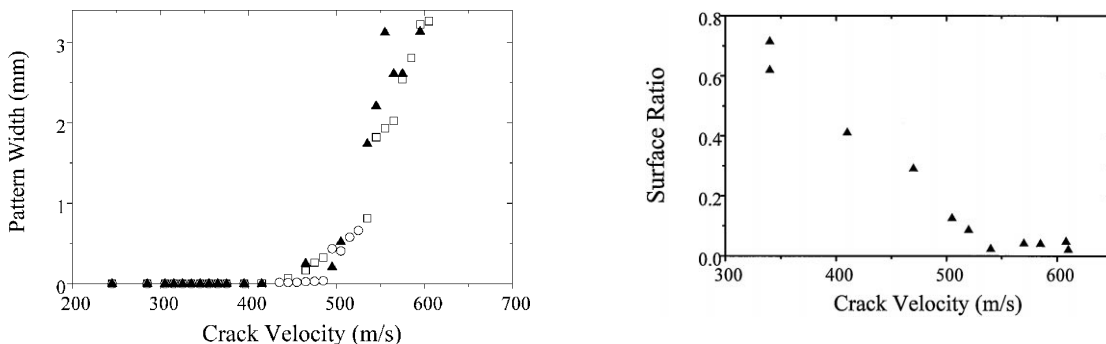
Fig. 32. The mean width of coherent zones on the fracture surface of PMMA as a function of the mean crack velocity. The data shown were obtained from both 0.8 mm wide (circles) and 3.0 mm wide (squares and triangles) samples. At $v = 550$ m/s the pattern width is on the order of the sample thickness, indicating a transition from a 3D to 2D state (from Ref. [102]).

Fig. 33. The surface ratio of a running crack as a function of its mean velocity, v. The surface ratio is defined as $(S_{out} - S_{in})/(S_{out} - S_{in})$ where S_{out} and S_{in} are, respectively, the surface areas created by micro-branches along the faces and center planes of the sample. The width of the PMMA sample used was 3 mm. At velocities above $1.65 v_c$, $S_{out} = S_{in}$ indicating a homogeneity of microcrack production across the entire width of the sample (from [102]).

survive and continue to propagate away from the main crack? A necessary condition for a micro-branch to develop into a macroscopic crack is the coherence of the micro-branch over the entire thickness of the sample. As shown in experiments on PMMA [102], near the instability onset, the width of a micro-branch is quite small (on the order of 100 μm). As the crack velocity increases beyond v_c, the branch width increases along with the branch length.

Sharon et al. [102] quantified the increase of the "coherence width" of the branches in two ways. The first method used was to study the width of the patterns formed by the branches along the fracture surface as a function of v. As can be seen in Fig. 25, the width of coherent "islands" formed along the fracture surface increases with v. The results of this analysis are reproduced in Fig. 32. From microscopic widths near v_c the pattern width increases sharply with the mean velocity of the crack, until, at a velocity of about $1.7 v_c$ the pattern becomes coherent across the entire thickness of the sample. Shortly above this velocity, macroscopic branching occurs.

An additional measure of this 3D to 2D transition can be seen in the micro-branch distribution across the sample width. Near the onset of the instability, the distribution of the micro-branches as a function of the distance away from the sample faces is very nonuniform. In PMMA the production of micro-branches near onset falls off sharply with the distance from the faces of the sample. To quantify this fall-off, Sharon et al. [102] measured the ratio of the amount of total fracture surface produced by the crack and branches located at the sample faces with that produced at the center of the sample (see Fig. 33). As Fig. 33 shows, the difference in surface production between the outer and center planes decreases continuously until, at $v = 1.65 v_c$, this difference vanishes, indicating a homogeneity of micro-branch production across the sample.

Curves similar in behavior to Fig. 32 have also been observed in studies of the rms surface amplitude and total sound emission of the crack by Boudet et al. [77]. In these experiments, the acoustic emission and rms surface amplitude of cracks propagating through PMMA were measured as a function of the crack's velocity. Both the sound emissions and surface roughness were

observed to diverge as the mean velocity approached $1.8v_c$ (600 m/s). These measurements, together with the divergent behavior of the pattern widths at nearly the same velocity, suggest that a second transition may be occurring at $v \sim 1.7v_c$. As the divergence of surface roughness observed by Boudet et al. [77] is indicative of macroscopic branching, the transition from 3D to 2D behavior described above may also be a *sufficient* condition for macroscopic branching to occur.

5.2.7. Energy dissipation by a crack

As we mentioned in Section 4.2.9, the fracture energy, Γ, increases sharply with the crack velocity in a variety of different brittle materials. In light of the micro-branching instability, can this sharp increase in the energy needed to form a crack be explained? In PMMA, as demonstrated in Fig. 17, the energy release rate increases by nearly an order of magnitude as the mean velocity of a crack surpasses v_c. Beyond v_c we know that the micro-branching instability occurs and, as a result the total amount of fracture surface created by the crack "front", must increase. This surface increase must thereby lead to an increase in Γ. Sharon et al. [113,102] quantified the amount of surface formed by the crack ensemble, by defining the *relative surface area* as the total area per unit crack width created by both the main crack and micro-branches, normalized by that which would be formed by a single crack. Their measurement, in PMMA, of the relative surface area as a function of the mean velocity of the crack is shown in Fig. 34. As only a single crack propagates prior to the instability the relative surface area is unity for $v < v_c$. Beyond this velocity, the total surface created indeed rises steeply with v, with the surface contribution due to micro-branches a factor of *six* greater than the surface contributed by a single crack at 600 m/s.

The data shown in Fig. 34 were obtained in experiments performed both in strip geometries, which yielded steady-state propagation, and large square aspect ratio samples where continuously accelerating cracks were observed. The velocity dependence of the relative surface area formed in both systems was the same, indicating the intrinsic character of the micro-branching instability.
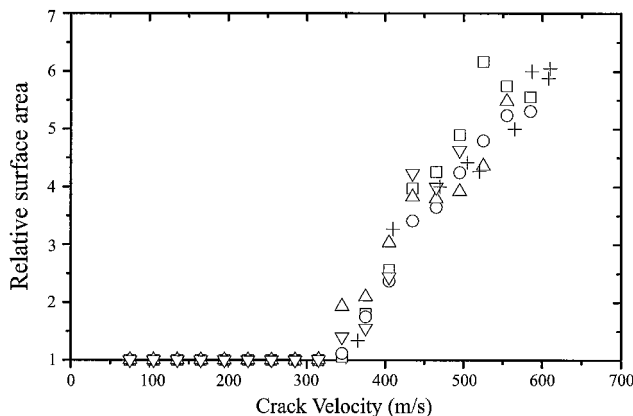
Fig. 34. The relative surface area (defined as the total area per unit width created by both the main crack and micro-branches normalized by that which would be created by a single crack) as a function of the mean crack velocity, v. The data in the figure were obtained from cracks moving at steady-state velocities in the strip configuration (crosses) as well as from accelerating cracks (other symbols) driven by stored energy densities varying between 3.2×10^6 to 5.1×10^6 erg/cm². Note that the total surface area at high velocities is many times greater than that created by the main crack (from Ref. [113]).
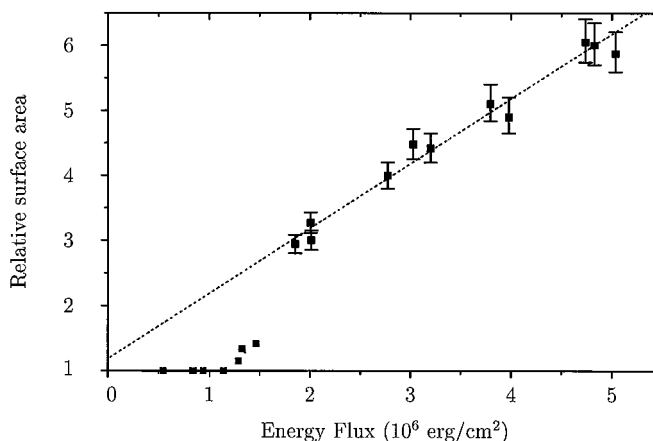
Fig. 35. The relative surface area as a function of the energy release rate, G, in PMMA. The data in the figure were obtained from experiments in the strip geometry, for steady-state mean crack velocities. After an initial jump (see text) the relative surface area is linearly dependent on G. The inverse slope of the graph leads to a constant energy cost per unit surface of 5×10^5 erg/cm^2. This is equal to the fracture energy immediately preceding the branching instability (from Ref. [113]).

In the experiments using the strip geometry, simultaneous measurements of the energy release rate, G, and the relative surface area were possible. The relationship between these quantities is shown in Fig. 35. The figure shows that after an initial jump which occurs at around $v > v_c$, the amount of surface area formed is a *linear* function of the energy release rate. This means that both before and after the instability onset, the fracture energy, given by the inverse slope of the curve, is nearly *constant*. The fracture energy "increase" observed in Fig. 17 and Fig. 13 in PMMA is thus explained entirely as a direct result of the micro-branching instability. The fracture energy effectively rises because increasingly more surface is created due to micro-branch formation. The cost, however, to create a unit fracture surface, remains constant and is close to the value of the fracture energy immediately preceding the instability onset. Although, at this writing, experiments verifying the constancy of Γ have only been performed in PMMA, it is conceivable that the universally observed increase in the fracture energy of brittle materials, demonstrated in Fig. 17, may be generally explained by this mechanism.

Some comments are in order. First, the micro-branching mechanism does not entirely explain the rise with crack velocity of the fracture energy. A close look at Fig. 17 reveals that even prior to the instability onset an increase in Γ with v is apparent. This increase, in itself, is not entirely surprising. PMMA is a polymer consisting of long, tangled molecular strands. In this material, the value of Γ may be determined by complex, rate-dependent processes which include plastic deformation of the material together with the heat dissipation involved in craze formation [90]. However, the micro-cracking instability contributes much more to changes in dissipation than these other processes.

An additional question arising from Fig. 35 is the origin of the jump in relative surface area that occurs at approximately the instability onset in PMMA. The "jump" in this figure would indicate that, initially, additional surface area is formed for "free", i.e. at a very small energy cost. We surmise that the reason for this jump is due to the size of the process zone surrounding the crack tip

in PMMA. As the vast majority of the fracture energy goes into the deformation of the area around the tip, the additional fracture energy contributed by a micro-branch within the process zone formed by the main crack would be negligible. Thus, the initial part of a micro-branch, whose additional area is counted in Fig. 35, dissipates nearly no additional energy. This conjecture is supported by the observations, in PMMA, of the non-zero minimum length of a micro-branch seen in Fig. 30 and that the minimum length is indeed consistent with estimates of the process zone size [102].

In light of these remarks, the long-standing puzzle of why a crack never seems to approach the Rayleigh wave speed in isotropic material, can now be answered. A crack does not need to dissipate increasing amounts of energy by accelerating, thereby increasing the amount of kinetic energy in the system. Beyond v_c a crack now has the option of dissipating energy by creating an increased amount of fracture surface at the expense of a reduction of the total kinetic energy throughout the system. As increasing amounts of energy flow to its tip, a crack forms a corresponding amount of surface via microscopic branching. As the energy flux to the crack tip increases further, the mean length of the micro-branches increases, as Fig. 28 shows. If G is increased still further, a second generation of micro-branches has been observed [102] to bifurcate off of the first generation of micro-branches. If this process continues, we see that the micro-branching instability may lead to a well-defined mechanism for the creation of a fractal structure. As in the Kolmogorov theory of turbulence, the smallest scale in this structure (analogous to the Kolmogorov or dissipation scale in turbulence) may be determined by the size of G.

5.2.8. Evidence for the universality of the instability

Most of our experimental work on the micro-branching instability has been performed in PMMA. An important question is whether the instability is a universal feature of dynamic fracture or is limited to some types of brittle polymers, such as PMMA. Both experimental data together with theoretical work, which will be described in later sections, indicate that the instability is indeed of a general nature in brittle fracture. As noted previously, patterns on the fracture surface, similar to those observed in PMMA, have been observed within the "mist" region in a number of brittle polymers such as polycarbonate and polystyrene. This observation would seem to, at least, suggest the existence of a similar, pattern-forming instability in brittle polymers.

To what extent is the micro-branch aspect of the instability is universal? As described in Section 4.2.2, microscopic branches have also been observed in all of the above materials. In addition, micro-branches were also seen within the mist region in both hardened steels, and glass as well as in brittle polymers. The claim for universality is also strengthened by the fact that micro-branches in both glass and PMMA develop nearly identical trajectories, as noted in Fig. 31. Additional experimental support for the universality of the functional form of micro-branches is given by the description of micro-branches, identified as "crazes" in early experiments in polystyrene [95]. As noted earlier, a universal trajectory for micro-branches would explain the consistent value of the macroscopic "branching angle" observed in a large variety of brittle materials.

Is the existence of a critical velocity for the instability also a universal aspect of brittle fracture? Irwin et al. [123], Ravi-Chandar and Knauss, 4.2.10) and Hauch and Marder [121] observed that microbranches are initiated in Homalite beyond $0.37v_R$, which is within 2% of the critical velocity observed in PMMA.

A critical velocity also exists in glass, but its value is different. Gross et al. [74], measured the acoustic emission of both glass and PMMA as a function of v for accelerating cracks. In these experiments, the acoustic spectra of these two very different materials were measured within windows centered at increasing velocities for both materials. The results of these experiments showed that the behavior of the acoustic spectra changed dramatically in both materials at values of $v/c_R = 0.36 = v_c$ in PMMA and $v/c_R = 0.42$ in soda lime glass. Below this value, the acoustic spectra were featureless whereas above the critical velocity, high intensity peaks in the acoustic emissions were observed. In PMMA, the frequency of these peaks was on the order of the characteristic time scale observed in the velocity oscillations (about 2–3 µs) and were Doppler-shifted as a function of v. The spectra in glass were higher in frequency (2–3 MHz) and had no observable Doppler shifts.

The lack of Doppler shifts in glass might be understood in light of work by Lund [124], who shows that the acoustic spectrum in glass is dominated by plate resonances. This prediction is plausible in glass, where acoustic attenuation is relatively small. In PMMA, where attenuation is much larger, the plate resonances are damped, and only the frequencies generated by moving crack tip are picked up by the transducers.

Experiments by Sharon et al. [83] have recently measured the first velocity at which micro-branches were observable in soda-lime glass, for both accelerating and steady-state cracks. As in PMMA, this velocity, in glass, is equal to the same value, $v = 0.42c_R$ that corresponds to the onset of acoustic emissions.

5.2.9. An unanswered question

Many features of the instability in PMMA show up as a rough oscillation with a frequency scale of 600 kHz. We believe that this frequency is closely connected with the distance a micro-branch travels before it is screened by the main crack and stops traveling; the characteristic crack speed of 500 m/s divided by the micro-branch length scale of 1 mm gives a frequency scale of 500 kHz. The oscillations observed in crack velocity as well as on the fracture surface are all reflections of the birth and death of micro-cracks However, we do not know why 1 mm is the characteristic distance the micro-cracks travel, so the origin of the 600 kHz oscillations is still unexplained.

6. Theories of the process zone

The experiments described in the previous section have established the existence and some of the characteristics of the micro-branching instability in the dynamic fracture of amorphous materials. In order to describe theoretical work related to this instability, it is necessary to introduce some of the concepts that have been used to describe the inner workings of the process zone. A huge fraction of this work has been devoted to metals, where the process zone involves plastic deformation. As our focus is upon brittle materials, we will not discuss this area.

6.1. Cohesive zone models

The stress fields of linear elastic fracture mechanics diverge as $1/\sqrt{r}$ approaching the crack tip. In reality stress cannot diverge. The actual phenomena in the process zone that limit the stress are

unquestionably complicated, so a variety of simple models has been proposed to show how the apparent elastic singularity actually joins smoothly onto a region around the crack tip where all fields are finite.

The cohesive zone of Barenblatt [125,126] and Dugdale [127] is the simplest possible view of the process zone. Assume that from the tip of the crack back to a distance Λ, a uniform stress σ_c acts between the crack surfaces, and then drops abruptly to zero at the point where the separation between the surfaces reaches a critical separation of s, as shown in Fig. 36. If the crack moves in a steady state so that the cohesive zone and all the elastic fields translate in the x direction without changing form, it is simple to find the energy absorbed by cohesive forces. Under these circumstances, the result of translating the crack by a distance δx is to increase by δx the length of material that has passed through the cohesive zone. To bring a length δx of material through the cohesive zone costs energy (per unit length along z)

$$\delta x \int_0^s \mathrm{d}y\, \sigma_c = \delta x s \sigma_c \ . \tag{158}$$

If all the energy going into the crack tip is dissipated by the cohesive forces, then the energy release rate G equals $s\sigma_c$. The idea of the cohesive zone models is to choose s and σ_c precisely so as to eliminate any singularities from the linear elastic problem. If any stress singularities remain after introduction of the cohesive zone, they will deliver a flux of energy into a mathematical point at the crack tip. Therefore, the condition

$$G = s\sigma_c \tag{159}$$

must coincide exactly with the condition for eliminating stress singularities. Using Eq. (81), it is possible to determine the length of the cohesive zone Λ. The cohesive zone can be viewed as a superposition of delta function stresses of the sort considered in that equation, but with tensile stresses σ_c, rather than the compressive stresses used before. The stress intensity factor due to this superposition is

$$K_{\mathrm{I}} = -\int_{-\Lambda}^0 \mathrm{d}l_0\, \sigma_c \sqrt{2/\pi l_0} = -\sigma_c \sqrt{8\Lambda/\pi} \ . \tag{160}$$

It is negative because the cohesive zone is pulling the crack faces together, and canceling out the positive stress intensity factor being produced by other forces outside the crack. According to Eq. (91), at distances from the crack tip very large compared to the cohesive zone size Λ, the energy release rate due to the apparently singular stress field is

$$G = \frac{1 - v^2}{E} A_{\mathrm{I}}(v) \sigma_c^2 \frac{8\Lambda}{\pi} \ , \tag{161}$$

which in combination with Eq. (159) determines Λ. As the velocity v of a crack approaches the Rayleigh wave speed, $A_{\mathrm{I}}(v)$ diverges, so the width of the cohesive zone, Λ, must drop to zero. The reason is that the crack opens more and more steeply as the crack speeds up, and reaches the critical separation s sooner and sooner.

Cohesive zones of this sort are frequently observed in the fracture of polymers, since behind the crack tip, there still are polymers arrayed in a "craze zone" stretching between the two crack faces
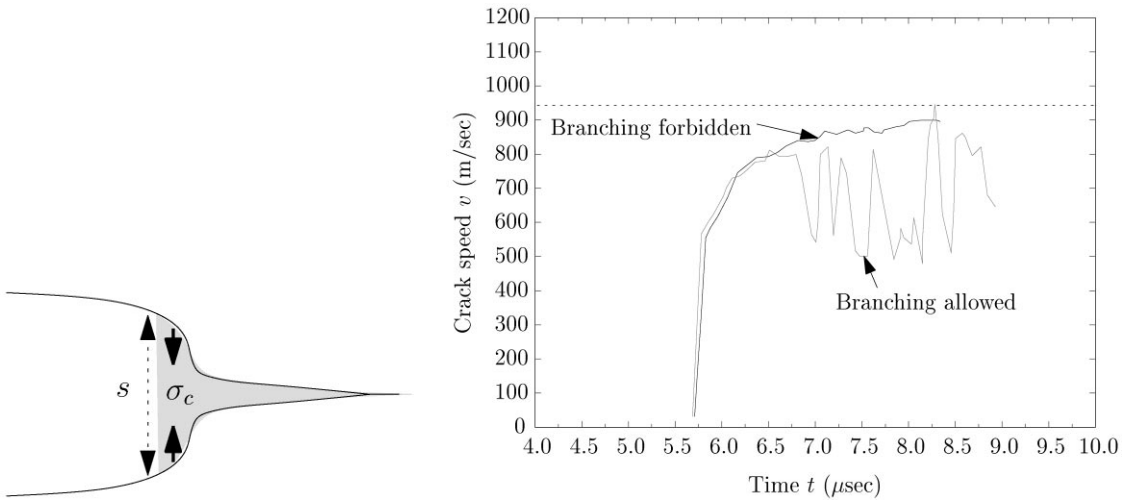
Fig. 36. Sketch of cohesive zone model of a crack tip. The faces of the crack are pulled together by a cohesive force σ_c hich acts until the faces are separated by a critical distance s. The crack is traveling from left to right, and the shaded region is the cohesive zone. Because the cohesive zone cancels out any externally generated stress intensity factor, the tip does not open up quadratically, and all stresses are finite.

Fig. 37. Crack velocities measured in finite element simulations of Xu and Needleman [129]. When the crack is allowed to branch, crack motion becomes unstable, and the mean velocity saturates at around half the Rayleigh wave speed. When branching is suppressed, the crack reaches speeds very close to the Rayleigh wave speed (dotted line).

and pulling them together. In the case of metals, the cohesive zone is viewed as a very simple representation of plastic flow around the crack tip.

In cases where the ingredients of the cohesive zone model have a clear physical interpretation, it provides a helpful way to describe the physics of the fracture energy. However, for the experimental phenomena we have described in the previous section, it is not obviously helpful. The phenomenological parameter Γ has been replaced by two phenomenological parameters σ_c and s, and one is no nearer than before to having a firm sense of how dissipation should vary with crack velocity. Cohesive zone models have played an important role in many attempts to understand brittle fracture instabilities from a continuum viewpoint, as we now describe.

6.2. Continuum studies

6.2.1. Finite element simulations

The closest correspondence with experiments in brittle amorphous materials has been obtained by Johnson [128], and Xu and Needleman [129], in finite element calculations. Both sets of authors observe frustrated branching, oscillations in crack velocities, and limiting velocities well below the Rayleigh wave speed.

Johnson [128] performed finite element calculations of fracture in an isotropic elastic material. He implements a model for the process zone intended to simulate material weakening around the crack that results from the nucleation of defects. In this model, the process zone is not a given size

but is adaptive, changing its size and character in accordance with the behavior of the crack. Cracks were driven by loading the crack faces with a number of different loads. These resulted in maximal crack velocities of 0.29, 0.44, and $0.55c_R$. At the lowest velocities (lowest driving), smooth acceleration of a crack was observed. As the loading of the crack faces was increased, multiple attempts at crack branching were observed. As in the experiments, the length of the attempted branches increased with the crack loading. These observations were not dependent on the details of the model. One of the goals of these simulations was to explore Ravi-Chandar and Knauss's observation that the stress intensity factor, beyond a certain crack velocity, is no longer a unique function of v. Similar behavior was indeed observed, and the cases where non-uniqueness of the stress intensity factor occurred were, as in the experiments, accompanied by attempted crack branching beyond a model-dependent threshold velocity.

Xu and Needleman also carried out finite element simulations, but with a different model of the process zone, and with more extensive results. To model the crack tip, Xu and Needleman implement a cohesive zone model similar to the one described in Section 6.1 which takes into account both tensile and shear stresses, and allows for the creation of new fracture surface with no additional dissipation added to the system. In order to permit cracks to branch off the main crack line, there is an underlying grid of lines on which material separation is permitted if a critical condition is obtained. Therefore, this code combines features of finite element models with lattice models to be described below, but is more realistic in many respects than the lattice models. The parameters used in the simulation were made to correspond to an isotropic elastic material with the properties of PMMA. Results of these simulations looked much like the experiments in PMMA. Beyond a critical velocity of $0.45c_R$, crack velocity oscillations together with attempted crack branching were observed. Branching angles of $29°$ were obtained, which are close to the maximal branching angles of $32°$ seen in experiment. Additional simulations were also conducted in a fashion that constrained the crack to move in a straight line. In this case, the crack accelerates to velocities close to c_R, just as in the experiments of Washabaugh and Knauss [87] that were discussed in Section 4.1. The crack velocities measured in the simulations are shown in Fig. 37. These computations come closer than any other approach to describing instabilities in the fracture of PMMA in a realistic fashion. However, they do not fully resolve the conceptual questions raised, for example, in Section 6.2.3.

6.2.2. Three-dimensional crack propagation

There is a number of calculations that explore the possibility that crack tip instabilities naturally result from a wiggly crack front moving through a heterogeneous medium. Rice et al. [130] analyzed the stability of a straight-line crack front in a scalar model of a crack propagating through such a heterogeneous solid. They found that although a single perturbation of the crack front was damped, the decay of a perturbation in this model was algebraic, decaying as $t^{-1/2}$ with time. Building on this result, Perrin and Rice [131,132] showed that the scalar model predicts that a crack propagating through a heterogeneous medium, where the crack front continually interacts with randomly distributed asperities, will *never* reach a statistically steady state. Instead, heterogeneities in the fracture energy lead to a logarithmic divergence of the rms deviations of an initially straight crack front. This result led to the suggestion that perhaps the roughness observed along a fracture surface may be the direct result of a continuous roughening of the surface that is driven by small inhomogeneities within the material. More recently Willis and Mochvan [133] calculated

the coupling of the energy release rate to random perturbations to the crack front in the case of planar perturbations to the crack in Mode I fracture. This analysis was recently extended by the same authors to out of plane perturbations [134].

Ramanathan and Fisher [135] used the Willis and Mochvan result to calculate the dynamics of planar perturbations to a tensile crack front. They found that, in contrast to the case of the scalar model where Perrin and Rice observed logarithmic instability of the crack front, in Mode I fracture weak heterogeneity of the medium can lead to a non-decaying unstable mode that propagates along the crack front. This propagating mode is predicted to occur in materials having $\partial \Gamma / \partial v \leq 0$, where a constant value of Γ is a marginal case. For $\partial \Gamma / \partial v > 0$, the propagating mode is predicted to decay. The propagation velocity of this new mode is predicted to be between 0.94–$1.0 c_R$. Numerical simulations of Mode I fracture in a three-dimensional medium with a constant Γ by Morrissey and Rice [136,137] support these results, indicating that the propagating mode is highly localized in space and indeed propagates at the predicted velocities.

Both Ramanathan et al. and Morrissey et al. show that these localized modes lead to *linear* growth of the rms deviations of an initially straight crack with its distance of propagation. This may, as the authors suggest, provide a new mechanism for the roughness produced by a propagating crack in materials where the fracture energy does not increase rapidly with the velocity of a crack. Both the calculations and simulations have been performed for in-plane disturbances to a crack front. Disturbances of this type cannot, of course, create the out-of-plane roughness typically observed along a fracture surface. It should be interesting to see whether fully three-dimensional perturbations to the crack front produce analogous effects.

6.2.3. Dynamic cohesive zone models

A large body of calculations has been carried out by Langer and collaborators on dynamic cohesive zone models. The cohesive zone is defined in a manner similar to that of Section 6.1, but cracks are not presumed to move at a constant rate, or always in a straight line, and the cohesive zone therefore becomes a dynamical entity, interacting with the crack in a complex fashion. The question posed by these authors is whether crack tip instabilities will emerge from such an analysis, and the results have been extremely puzzling.

In a first set of calculations, Barber et al. [138], Langer [139,140], and Ching [141] investigated the dynamics of cracks confined to straight lines. Such cracks always traveled in a stable fashion, consistent also with the results in Ref. [142], although there were various tantalizing hints of instabilities. Therefore, attention turned to the dynamics of cracks allowed to follow curvy, out of plane, paths [143–145]. Pathological short-wavelength instabilities of cracks now began to emerge from the analysis, for a reason that has a simple underlying explanation.

The logic of the principle of local symmetry says that bonds under the greatest tension break first, and therefore cracks loaded in Mode I move straight ahead, at least until the velocity identified by Yoffe when a crack is predicted to spontaneously break the symmetry inherent in straight-line propagation. This logic is called into question by a very simple calculation, first described by Rice [146].

Let us look at the ratio σ_{xx}/σ_{yy} right on the crack line. From Eq. (69) it is

$$\frac{\sigma_{xx}}{\sigma_{yy}} = \frac{(\beta^2 + 1)(1 + 2(\alpha^2 - \beta^2) - 4\alpha\beta}{4\alpha\beta - (1 + \beta^2)^2} \tag{162}$$

$$= \frac{2(\beta^2 + 1)(\alpha^2 - \beta^2)}{4\alpha\beta - (1 + \beta^2)^2} - 1 \; . \tag{163}$$

The Taylor expansion of Eq. (163) for low velocities v is

$$1 + \frac{v^2(c_t^4 + c_\ell^4)}{2c_\ell^2 c_t^2 (c_\ell - c_t)(c_\ell + c_t)} + \cdots \; , \tag{164}$$

and in fact Eq. (163) greater than unity for *all* v. This result is surprising because it states that, in fact, the greatest tensile forces are perpendicular to a crack tip and not parallel to it, as soon as the crack begins to move. Therefore, it is hard to understand why a crack is ever supposed to move in a straight line.

These remarks do not do justice to the calculations performed with the cohesive zone models. In their most elaborate versions, the crack is allowed to pursue an oscillating path, and the cohesive zone contains both tensile and shear components. In most, although not all of these models, crack propagation is violently unstable to very short-length oscillations of the tip.

A summary of this work has been provided by Langer and Lobchevsky [147]. They consider a large class of models, and correct subtle errors in previous analyses. They do find some models in which a crack undergoes a Hopf bifurcation to an oscillation at a critical velocity. However, their "general conclusion is that these cohesive-zone models are inherently unsatisfactory for use in dynamical studies. They are extremely difficult mathematically and they seem to be highly sensitive to details that ought to be physically unimportant."

One possibility is that cohesive zone models must be replaced by models in which plastic yielding is distributed across an area, and not restricted to a line. Dynamic elastic–plastic fracture has not, to our knowledge, considered cracks moving away from straight paths. Another possibility is that these calculations signal a failure of continuum theory, and that the resolution must be sought at the atomic or molecular scale. It is not possible right now to decide conclusively between these two possibilities. However, the experimental observation that the dynamic instabilities consist of repeated frustrated branching seems difficult to capture in a continuum description of the process zone.

6.3. Dynamic fracture of lattice in Mode I

In contrast to cohesive zone models, where the correct starting equations still are not yet known with certainty, and instabilities in qualitative accord with experiment are difficult to find, calculations in crystals provide a context where the starting point is unambiguous, and instabilities resembling those seen in experiment arise quite naturally. In this section we will record some theoretical results relating to the instability. We will first focus on a description of brittle fracture introduced by Slepyan [148], and Marder and Liu [149,120]. The aim of this approach to fracture is to find a case where it is possible to study the motion of a crack in a macroscopic sample, but describing the motion of every atom in detail. In this way, questions about the behavior of the process zone and the precise nature of crack motion can be resolved without any additional assumptions.

This task can be accomplished by arranging atoms in a crystal, and adopting a simple force law between them, one in which forces rise linearly up to a critical separation, and then abruptly drop to zero. We call a solid built of atoms of this type an *ideal brittle crystal*. A force law of this type is

not, of course, completely realistic, but has long been thought a sensible approximation in brittle ceramics [20]. It is more realistic in brittle materials than, for example, Lennard–Jones or Morse potentials. A surprising fact is that this force law makes it possible to obtain a large variety of analytical results for fracture in arbitrarily large systems. Furthermore, the qualitative lessons following from these calculations seem also to be quite general.

A summary of results from the ideal brittle crystal is

- *Lattice trapping*: For a range of loads above the Griffith point, a crack can be trapped by the crystal, and does not move, although it is energetically possible [150,10].
- *Steady-states*: Steady-state crack motion exists, and is a stable attractor for a range of energy flux.
- *Phonons*: Steadily moving cracks emit phonons whose frequencies can be computed from a simple conservation law.
- *Fracture energy* The relation between the fracture energy and velocity can be computed.
- *Velocity gap*: The slowest steady state runs at around 20% of the Rayleigh wave speed; no slower-moving steady-state crack exists.
- *Instability*: At an upper critical energy flux, steady-state cracks become unstable, and generate frustrated branching events in a fashion reminiscent of experiments in amorphous materials.

One may wonder about the motivation for formulating a theory for the dynamic behavior of a crack in a crystal. Is the lattice essential or can one make the underlying lattice go away by taking a continuum limit? So far as we know, all attempts to describe the process zone of brittle materials in a continuum framework have run into severe difficulties [147]. These problems do not arise in an atomic-scale description.

The simplicity of the ideal brittle crystal is somewhat misleading in a number of respects. Therefore, before introducing the mathematics, we will comment on a number of natural questions regarding the generality of the predictions it makes.

- *Does the simple force law employed between atoms neglect essential aspects of the dynamics?* We will demonstrate that the same qualitative results observed in the ideal brittle crystal occur in extensive molecular dynamic simulations using realistic potentials.
- *The calculations are in a strip. Is this geometry too restrictive?* To this question the general formalism of fracture mechanics provides an answer. Fracture mechanics tells us that as long as the conditions of small-scale yielding are satisfied, the behavior of a crack is entirely governed by the structure of the stress fields in the near vicinity of the crack tip. These fields are solely determined by the flux of energy to the crack tip. A given energy flux can be provided by an infinite number of different loading configurations, but the resultant dynamics of the crack will be the same. As a result, the specific geometry used to load the system is irrelevant and no generality is lost by the use of a specific loading configuration. This fact is borne out by the experimental work described in the previous section.
- *Have lattice trapping and the velocity gap ever been seen experimentally?* No, they have not, but appropriate experiments have not yet been performed. Molecular dynamics simulations indicate that lattice trapping disappears at room temperature. New experiments are needed to obtain a detailed description of dynamic fracture in crystals at low temperatures.
- *Are results in a crystal relevant for amorphous materials?* This is still an open question. However, the results of the lattice calculations seem to be remarkably robust. Adding quenched noise to

the crystal has little qualitative effect. The effects of topological disorder are not known. However, a certain amount is known about the effects of increasing temperature. When the temperature of a brittle crystal increases above zero, the velocity gap closes [151], and its behavior is reminiscent of that seen in experiments performed on amorphous materials.

Kulakhmetova et al. [152] first showed that it is possible to find exact analytical expressions for Mode I cracks moving in a square lattice. They found exact relationships between the energy flux to a crack tip and crack tip velocity. They also observed that phonons must be emitted by moving cracks, and calculated their frequencies and amplitudes. Later calculations extended these results to other crystal geometries, allowed for a general Poisson ratio, showed that there is a minimum allowed crack velocity, found when steady crack motion is linearly stable, calculated the point at which steady motion becomes unstable to a branching instability, and estimated the spacing between branches [120].

These calculations are extremely elaborate. The analytical expressions are too lengthy to fit easily on printed pages, and most of the results were obtained with the aid of symbolic algebra. For this reason, we will simply summarize some of the results, and then proceed to describe in detail how the calculations work in the case of anti-plane shear, Mode III, where the algebra is much less demanding but most of the ideas are the same.

6.3.1. Mode I equations

Let u_i describe the displacement of a mass point from its equilibrium location. Assume that the energy of the system is a sum of terms depending upon two particles at a time, and linearize the energy to lowest order in particle displacements. Translational invariance demands that the forces between particles 0 and 1 depend only upon $u_1 - u_0$, which will be defined to be $\mathscr{D}_1$. However, the force can be a general linear functional of $\mathscr{D}_1$. A way to write Figs. 38 and 39 such a general linear functional is to decompose the force between particles 0 and 1 into a component along $\hat{d}_{1\parallel}$, and a component that is along $\hat{d}_{1\perp}$. The first component corresponds to central forces between atoms, while the second component is a non-central force. Non-central forces between atoms are the rule
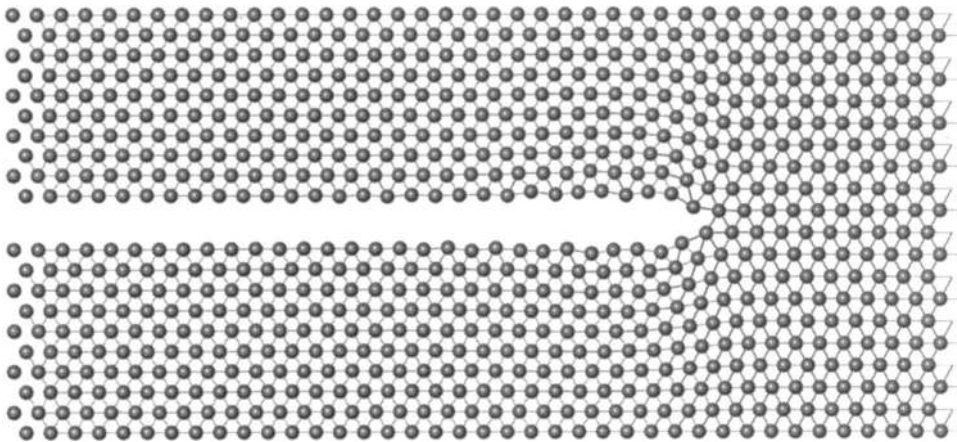

Fig. 38. A sketch showing steady-state motion of crack moving in an ideal brittle crystalline strip loaded in Mode I.
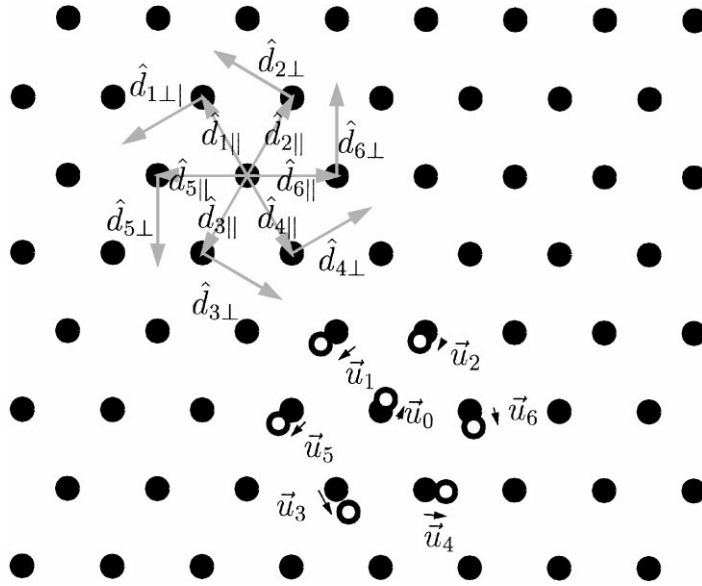
Fig. 39. The geometry of the lattice used for fracture calculations.

rather than the exception in real materials, as first appreciated by Born. Their quantum-mechanical origin is of no concern here, only the fact that they are not zero. Suppose that the restoring force parallel to the direction of equilibrium bonds is proportional to $\mathcal{K}_\parallel$, while that perpendicular to this direction is proportional to $\mathcal{K}_\perp$. The force due to the displacement of the particle along $\mathcal{D}_1 = \boldsymbol{u}_{i-1,j+1} - \boldsymbol{u}_{i,j}$ is

$$\mathcal{K}_\parallel \hat{d}_{\parallel 1}(\mathcal{D}_1 \cdot \hat{d}_{\parallel 1}) + \mathcal{K}_\perp \hat{d}_{\perp 1}(\mathcal{D}_1 \cdot \hat{d}_{\perp 1}) \tag{165}$$

$$= \mathcal{K}_\parallel \left(\frac{-1}{2}, \frac{\sqrt{3}}{2}\right)\left(\frac{-1}{2}\mathcal{D}_1^x, \frac{\sqrt{3}}{2}\mathcal{D}_1^y\right) + \mathcal{K}_\perp \left(\frac{\sqrt{3}}{2}, \frac{1}{2}\right)\left(\frac{\sqrt{3}}{2}\mathcal{D}_1^x, \frac{1}{2}\mathcal{D}_1^y\right). \tag{166}$$

Adding up contributions from other particles in this way we get for the force due to neighbors

$$\boldsymbol{F}(m,n) = \sum_{j=1}^{6} \sum_{q=\parallel,\perp} \mathcal{K}_q \hat{d}_{qj}(\mathcal{D}_j(m,n) \cdot \hat{d}_{qj}) . \tag{167}$$

By varying the constants $\mathcal{K}_\parallel$ and $\mathcal{K}_\perp$, one can obtain any desired values of shear and longitudinal wave speeds, which are given by

$$c_\ell^2 = \frac{3a^2}{8m}(\mathcal{K}_\perp + 3\mathcal{K}_\parallel) , \tag{168a}$$

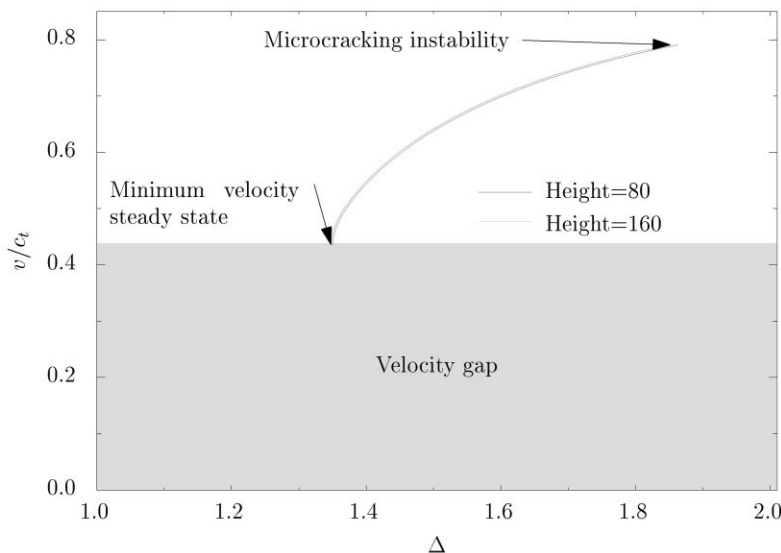$$c_t^2 = \frac{3a^2}{8m}(3\mathcal{K}_\perp + \mathcal{K}_\parallel) , \tag{168b}$$

Fig. 40. Crack velocity versus loading parameter $\Delta = K_{\mathrm{I}}/K_{\mathrm{Ic}}$ for strips 80 and 160 atoms high, in limit of vanishing dissipation, computed for Mode I crack by methods of following section. Δ will be defined precisely in Eq. (178). The spring constants have values $\mathscr{K}_{\parallel} = 2.6$ and $\mathscr{K}_{\perp} = 0.26$, so that the non-central forces are relatively small. The fact that the results have become independent of the height of the strip for such small numbers of atoms in the vertical direction suggests that relatively small molecular dynamics simulations can be used to obtain results appropriate for the macroscopic limit.

where m is the mass of each particle. In addition to forces between neighbors, it is possible to add complicated dissipative functions depending upon particle velocities. In Ref. [120], a term was added to the equations so as to reproduce the experimentally measured frequency dependence of sound attenuation in Plexiglas. There is a slight technical restriction in the calculations of Ref. [120]; right on the crack line, forces are required to be central. E. Gerde has found a way to overcome this technical limitation, and the results do not change noticeably.

There is no universal curve describing Mode I fracture. Many details in the relation between loading and crack velocity depend upon ratios of the sound speeds, and upon the frequency dependence of dissipation. In the limit of central forces, $\mathscr{K}_{\perp} = 0$, it turns out to be difficult but not impossible to have cracks in steady state. This means that the range of loads for which cracks can run in a stable fashion is small, and depends in detail upon the amount of dissipation. Crack motion is greatly stabilized by having nonzero $\mathscr{K}_{\perp}$. Fig. 40 displays a representative result with some implications for the design of molecular dynamics simulations. In the limit of vanishing dissipation, the relation between crack speed and dimensionless loading $\Delta = K_{\mathrm{I}}/K_{\mathrm{Ic}}$ becomes nearly independent of the number of vertical rows of atoms for strips around 40 rows high. The definition of Δ is that it describes the vertical displacement imposed upon the top and bottom of the strip, but scaled so that $\Delta = 1$ when these boundaries have been stretched just far enough apart so that the energy stored per length to the right of the crack tip just equals the energy cost per length of extending the crack. It is defined precisely by Eq. (178).

Rather than plunging into a series of graphs similar to Eq. (40), which would serve little purpose but to demonstrate that Mode I lattice fracture can indeed be solved analytically in a wide range of cases, we will move on to a simpler geometry in which the analytical methods can be displayed in full detail, and in which almost all the ideas needed to understand Mode I can be explored with much less elaborate algebra.

6.4. Dynamic fracture of a lattice in anti-plane shear, Mode III

6.4.1. Definition and energetics of the model

We now work in detail through some of the analytical results available for a crack moving through an ideal brittle crystal loaded in Mode III. The main results are the relation between loading and crack velocity, the prediction of a velocity gap, and the calculation of the point at which steady crack motion becomes unstable. Linear stability of the steady states will not be considered here; the result obtained in [120] is that the steady states, when they exist, are always linearly stable.

Consider a crack moving in a strip composed of $2(N + 1)$ rows of mass points, shown in Fig. 41. All of the bonds between lattice points are brittle–elastic, behaving as perfect linear springs until the instant they snap at a separation of $2u_f$, from which point on they exert no force. The location of each mass point is described by a single spatial coordinate $u(m,n)$, which can be interpreted as the height of mass point (m,n) into or out of the page. The force between adjacent masses is determined
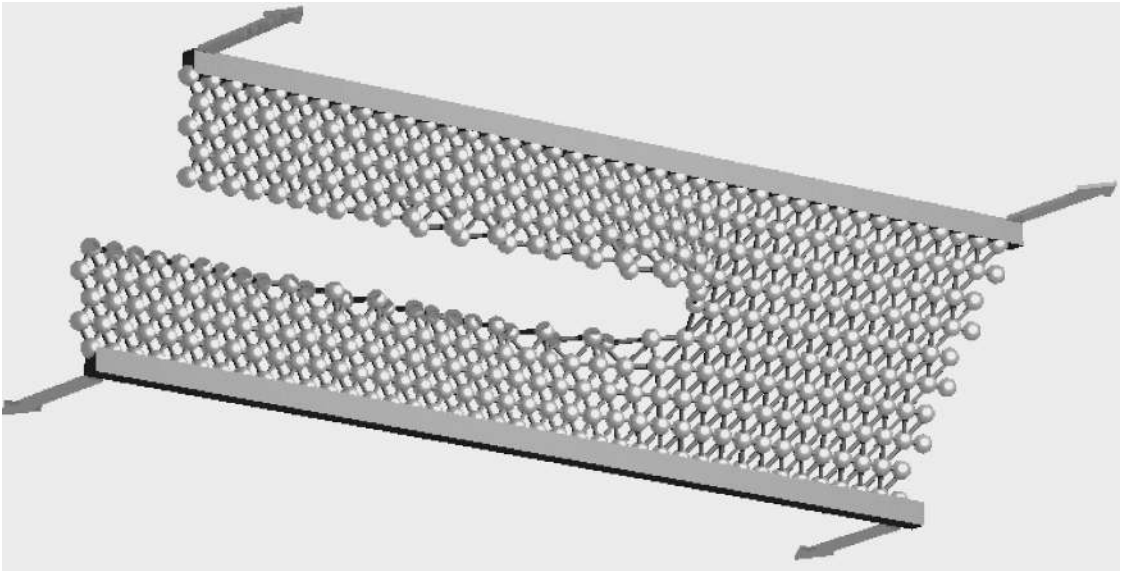
Fig. 41. Dynamic fracture of a triangular crystal in anti-plane shear. The crystal has $2(N + 1)$ rows of atoms, with $N = 4$, and $2N + 1$ rows of bonds. Heights of spheres indicate displacements $u(m,n)$ of mass points out of the page once displacements are imposed at the boundaries. The top line of spheres is displaced out of the page by amount $u(m,N + 1/2) = U_N = \Delta\sqrt{2N + 1}$, and the bottom line into the page by amount $u(m, -N - 1/2) = -U_N = -\Delta\sqrt{2N + 1}$. Lines connecting mass points indicate whether the displacement between them has exceeded the critical value of $2u_f$; see Eq. (169b).

by the difference in height between them. The index m takes integer values, while n takes values of the form $1/2, 3/2, \ldots, N + 1/2$. The model is described by the equation

$$\ddot{u}(m,n) = -b\dot{u} + \frac{1}{2} \sum_{\substack{\text{nearest } m',n' \\ \text{neighbors}}} \mathscr{F}[u(m',n') - u(m,n)] \,, \tag{169a}$$

with

$$\mathscr{F}(u) = u\theta(2u_f - |u|) \tag{169b}$$

describing ideal brittle springs, θ the step function, and b the coefficient of a small dissipative term. There is no difficulty involved in choosing alternative forms of the dissipation, if desired. The boundary condition which drives the motion of the crack is

$$u(m, \pm[N + 1/2]) = \pm U_N \,. \tag{169c}$$

It is important to find the value of U_N for which there is just enough energy stored per length to the right of the crack to snap the pair of bonds connected to each lattice site on the crack line. For $m \gg 0$ one has

$$u(m,n) = nU_N/(N + 1/2) \,, \tag{170}$$

and the height difference between mass points with adjacent values of n is

$$U_{\text{right}} = U_N/(N + 1/2) \,. \tag{171}$$

Therefore, the energy stored per unit length in the $2N + 1$ rows of bonds is

$$\tfrac{1}{2} \times [2 \text{ Upper Bonds/Site}] \times [\text{Rows}] \times [\text{Spring Constant}] \times U_{\text{right}}^2 \tag{172}$$

$$= \tfrac{1}{2} 2(2N + 1)\tfrac{1}{2}\left(\frac{U_N}{N + 1/2}\right)^2 \tag{173}$$

$$= 2Q_0(U_N)^2 \,, \tag{174}$$

with

$$Q_0 = 1/(2N + 1) \,. \tag{175}$$

The energy required to snap two bonds each time the crack advances by a unit length is

$$\tfrac{1}{2} \times [2 \text{ Bonds/Site}] \times [\text{Spring Constant}] \times [\text{Separation at fracture}]^2 \tag{176}$$

$$= \tfrac{1}{2} \times 2 \times \tfrac{1}{2} \times (2u_f)^2 = 2u_f^2 \,. \tag{177}$$

Therefore, equating Eqs. (174) and (177) the proper dimensionless measure of the external driving is

$$\Delta = U_N\sqrt{Q_0}/u_f \,, \tag{178}$$

a quantity which reaches 1 as soon as there is enough energy to the right of the crack to snap the bonds along the crack line, and which is linearly related to the displacements imposed at the edges of the strip.

6.4.2. The detailed solution

The techniques used to solve problems of this type were found by Slepyan [148,152]. There are differences between details of his solution and ours because Eq. (169) describes motion in a strip rather than an infinite plate, and in a triangular rather than a square lattice. The strip is preferable to the infinite plate when it comes time to compare with numerical simulations, while reducing to the simpler infinite plate results in certain natural limits. The velocity gap and nonlinear instabilities were first found in [149,120].

6.4.3. Symmetries

Assume that a crack moves in steady state, so that one by one, the bonds connecting $u(m,1/2)$ with $u(m + 1, -1/2)$ or $u(m, -1/2)$ break. They break because the distance between these points exceeds the limit set in Eq. (169b) and as a consequence of the driving force described by Eq. (169c). Assuming that the times at which bonds break are known, the original nonlinear problem is immediately transformed into a linear problem. However, one has to come back at the end of the calculation to verify that

1. *Bonds break at the time they are supposed to.* Imposing this condition determines a relation between crack velocity v and loading Δ.
2. *No bonds break when they are not supposed to.* Imposing this condition leads to the velocity gap on the low-velocity end, and to crack tip instabilities above a critical energy flux.

Steady states in a crystal are more complicated than steady states in a continuum. In a continuum, steady state acts as $u(x - vt)$. The closest one can come in a triangular crystal is by having the symmetry

$$u(m,n,t) = u(m + 1,n,t + 1/v) \tag{179a}$$

and also

$$u(m,n,t) = -u(m, -n,t - [1/2 - g_n]/v) \tag{179b}$$

which implies in particular that

$$u(m,1/2,t) = -u(m, -1/2,t - 1/2v) . \tag{179c}$$

We have defined

$$g_n = \begin{cases} 0 & \text{if } n = 1/2,5/2 \dots \\ 1 & \text{if } n = 3/2,7/2 \dots , \\ \text{mod}(n - 1/2,2) & \text{in general} . \end{cases} \tag{180}$$

6.4.4. Eliminating the spatial index m

Assuming that a crack is in steady state, we can therefore eliminate the variable m entirely from the equation of motion, by defining

$$u_n(t) = u(0,n,t) , \tag{181}$$

and write the equations of motion in steady state as

$$\ddot{u}_n(t) = \frac{1}{2}\left[\begin{array}{ll} + u_{n+1}(t - (g_{n+1} - 1)/v) & + u_{n+1}(t - g_{n+1}/v) \\ + u_n(t + 1/v) & - 6u_n(t) + u_n(t - 1/v) \\ + u_{n-1}(t - (g_{n-1} - 1)/v) & + u_{n-1}(t - g_{n-1}/v) \end{array}\right] - b\dot{u}_n \tag{182a}$$

if $n > 1/2$, and

$$\ddot{u}_{1/2}(t) = \frac{1}{2}\left[\begin{array}{ll} + u_{3/2}(t) & + u_{3/2}(t - 1/v) \\ + u_{1/2}(t + 1/v) - 4u_{1/2}(t) & + u_{1/2}(t - 1/v) \\ + [u_{-1/2}(t) - u_{1/2}(t)]\theta(-t) & + [u_{-1/2}(t - 1/v) - u_{1/2}(t)]\theta(1/(2v) - t) \end{array}\right] - b\dot{u}_{1/2} \tag{182b}$$

if $n = 1/2$.

The time at which the bond between $u(0,1/2,t)$ and $u(0, -1/2,t)$ breaks has been chosen to be $t = 0$, so that by symmetry the time the bond between $u(0,1/2,t)$ and $u(1, -1/2,t)$ breaks is $1/2v$.

6.4.5. Equations solved in terms of a single mass point on crack line

Above the crack line, the equations of motion (182a) are completely linear, so it is simple to find the motion of every atom with $n > 1/2$ in terms of the behavior of an atom with $n = 1/2$. Fourier transforming Eq. (182a) in time gives

$$-\omega^2 u_n(\omega) = \mathrm{i}b\omega + \left\{\begin{array}{l} \frac{1}{2}u_{n+1}(\omega)[\mathrm{e}^{\mathrm{i}\omega(g_{n+1} - 1)/v} + \mathrm{e}^{\mathrm{i}\omega(g_{n+1})/v}] \\ + \frac{1}{2}u_n(\omega)[\mathrm{e}^{\mathrm{i}\omega/v} - 6 + \mathrm{e}^{-\mathrm{i}\omega/v}] \\ + \frac{1}{2}u_{n-1}(\omega)[\mathrm{e}^{\mathrm{i}\omega(g_{n-1} - 1)/v} + \mathrm{e}^{\mathrm{i}\omega(g_{n-1})/v}] \end{array}\right\}. \tag{183}$$

Let

$$u_n(\omega) = u_{1/2}(\omega)\mathrm{e}^{k(n - 1/2) - \mathrm{i}\omega g_n/(2v)}. \tag{184}$$

Substituting Eq. (184) into Eq. (183), and noticing that $g_n + g_{n+1} = 1$ gives

$$-\omega^2 u_{1/2}(\omega) = \mathrm{i}b\omega u_{1/2}(\omega) + \left\{\begin{array}{l} \frac{1}{2}u_{1/2}(\omega)\mathrm{e}^k[\mathrm{e}^{\mathrm{i}\omega(g_{n+1} + g_{n-2})/(2v)} + \mathrm{e}^{\mathrm{i}\omega(g_{n+1} + g_n)/(2v)}] \\ + \frac{1}{2}u_{1/2}(\omega)[\mathrm{e}^{\mathrm{i}\omega/v} - 6 + \mathrm{e}^{-\mathrm{i}\omega/v}] \\ + \frac{1}{2}u_{1/2}(\omega)\mathrm{e}^{-k}[\mathrm{e}^{\mathrm{i}\omega(g_{n-1} + g_{n-2})/(2v)} + \mathrm{e}^{\mathrm{i}\omega(g_{n-1} + g_n)/(2v)}] \end{array}\right\} \tag{185}$$

$$\Rightarrow \omega^2 + \mathrm{i}b\omega + 2\cosh(k)\cos(\omega/(2v)) + \cos(\omega/v) - 3 = 0. \tag{186}$$

Defining

$$z = \frac{3 - \cos(\omega/v) - \omega^2 - \mathrm{i}b\omega}{2\cos(\omega/2v)}, \tag{187}$$

one has equivalently that

$$y = z + \sqrt{z^2 - 1}, \tag{188}$$

with

$$y = \mathrm{e}^k. \tag{189}$$

One can construct a solution which meets all the boundary conditions by writing

$$u_n(\omega) = u_{1/2}(\omega)\mathrm{e}^{-\mathrm{i}\omega g_n/2v}\left[\frac{y^{[N+1/2-n]} - y^{-[N+1/2-n]}}{y^N - y^{-N}}\right] + \frac{U_N(n-1/2)}{N}\frac{2\alpha}{\alpha^2 + \omega^2} . \tag{190}$$

This solution equals $u_{1/2}$ for $n = 1/2$, and equals $U_N 2\alpha/(\alpha^2 + \omega^2)$ for $n = N + 1/2$. The reason to introduce α is that for $n = N + 1/2$, $u(m,n,t) = U_N$. The Fourier transform of this boundary condition is a delta function, and hard to work with formally. To resolve uncertainties, it is better to use instead the boundary condition

$$u_{N+1/2}(t) = U_N \mathrm{e}^{-\alpha|t|} , \tag{191}$$

and send α to zero the end of the calculation. In what follows, frequent use will be made of the fact that α is small.

The most interesting variable is not $u_{1/2}$, but the distance between the bonds which will actually snap. For this reason define

$$U(t) = \frac{u_{1/2}(t) - u_{-1/2}(t)}{2} = \frac{u_{1/2}(t) + u_{1/2}(t + 1/2v)}{2} . \tag{192}$$

Rewrite Eq. (182b) as

$$\ddot{u}_{1/2}(t) = \frac{1}{2}\begin{bmatrix} + u_{3/2}(t) & + u_{3/2}(t - 1/v) \\ + u_{1/2}(t + 1/v) - 4 & u_{1/2}(t) + u_{1/2}(t - 1/v) \\ - 2U(t)\theta(-t) & - 2U(t - 1/2v)\theta(1/(2v) - t) \end{bmatrix} - b\dot{u}_{1/2} . \tag{193}$$

Fourier transforming this expression using Eq. (190) and defining

$$U^{\pm}(\omega) = \int_{-\infty}^{\infty} \mathrm{d}\omega \mathrm{e}^{\mathrm{i}\omega t} U(t)\theta(\pm t) , \tag{194}$$

now gives

$$u_{1/2}(\omega)F(\omega) - (1 + \mathrm{e}^{\mathrm{i}\omega/2v})U^{-}(\omega) = -\frac{U_N}{N}\frac{2\alpha}{\omega^2 + \alpha^2} , \tag{195}$$

with

$$F(\omega) = \left\{\frac{y^{[N-1]} - y^{-[N-1]}}{y^N - y^{-N}} - 2z\right\}\cos(\omega/2v) + 1 \tag{196}$$

Next, use Eq. (192) in the form

$$U(\omega) = \tfrac{1}{2}(1 + \mathrm{e}^{-\mathrm{i}\omega/2v})u_{1/2}(\omega) \tag{197}$$

to obtain

$$U(\omega)F(\omega) - 2(\cos^2\omega/4v)U^{-}(\omega) = -\frac{U_N}{N}\frac{2\alpha}{\omega^2 + \alpha^2} . \tag{198}$$

Writing

$$U(\omega) = U^{+}(\omega) + U^{-}(\omega) \tag{199}$$

finally gives

$$U^+(\omega)Q(\omega) + U^-(\omega) = U_N Q_0 \left\{ \frac{1}{\alpha + i\omega} + \frac{1}{\alpha - i\omega} \right\},$$ (200)

with

$$Q(\omega) = \frac{F(\omega)}{F(\omega) - 2\cos^2\omega/4v} \ .$$ (201)

To obtain the right hand side of Eq. (200), one uses the facts that $F(0) = -1/N$, and that α is very small, so that the right-hand side of Eq. (200) is a delta function.

The Wiener–Hopf technique [153] directs one to write

$$Q(\omega) = Q^-(\omega)/Q^+(\omega) \ ,$$ (202)

where Q^- is free of poles and zeroes in the lower complex ω plane and Q^+ is free of poles and zeroes in the upper complex plane. One can carry out this decomposition with the explicit formula

$$Q^\pm(\omega) = \exp\left[\lim_{\varepsilon \to 0} \int \frac{d\omega'}{2\pi} \frac{\ln Q(\omega')}{i\omega \mp \varepsilon - i\omega'} \right].$$ (203)

Now separate Eq. (200) into two pieces, one of which has poles only in the lower half plane, and one of which has poles only in the upper half plane:

$$\frac{U^+(\omega)}{Q^+(\omega)} - \frac{Q_0 U_N}{Q^-(0)} \frac{1}{(-i\omega + \alpha)} = \frac{Q_0 U_N}{Q^-(0)} \frac{1}{(i\omega + \alpha)} - \frac{U^-(\omega)}{Q^-(\omega)} \ .$$ (204)

Because the right- and left-hand sides of this equation have poles in opposite sections of the complex plane, they must separately equal a constant, $\mathscr{C}$. The constant must vanish, or U^- and U^+ will behave as a delta function near $t = 0$. So

$$U^-(\omega) = U_N \frac{Q_0 Q^-(\omega)}{Q^-(0)(\alpha + i\omega)}$$ (205a)

and

$$U^+(\omega) = U_N \frac{Q_0 Q^+(\omega)}{Q^-(0)(\alpha - i\omega)} \ .$$ (205b)

One now has an explicit solution for $U(\omega)$. Numerical evaluation of Eq. (203), and $U(t)$ from Eq. (205) is fairly straightforward, using fast Fourier transforms. However, in carrying out the numerical transforms, it is important to analyze the behavior of the functions for large values of ω. In cases where functions to be transformed decay as $1/i\omega$, this behavior is best subtracted off before the numerical transform is performed, with the appropriate step function added back analytically afterwards. Conversely, in cases where functions to be transformed have a step function discontinuity, it is best to subtract off the appropriate multiple of $e^{-t}\theta(t)$ before the transform, adding on the appropriate multiple of $1/(1 - i\omega)$ afterwards. A solution of Eq. (205) constructed in this manner appears in Fig. 43.

6.4.6. Relation between Δ and v

Recall that making the transition from the nonlinear problem originally posed in Eq. (169a) to the linear problem in Eq. (182) relies on supposing that bonds along the crack line snap at time

intervals of $1/2v$. Because of the symmetries in Eq. (179), it is sufficient to guarantee that

$$u(t) = u_f \quad \text{at } t = 0 . \tag{206}$$

All displacements are simply proportional to the boundary displacement U_N, so Eq. (206) fixes a unique value of U_N, and its dimensionless counterpart, Δ. Once one assumes that the crack moves in steady state at a velocity v, there is a unique Δ to make it possible.

To obtain Eq. (206), one needs to require that

$$\lim_{t \to 0^-} \int \frac{d\omega}{2\pi} e^{-i\omega t} U^-(\omega) = u_f . \tag{207}$$

This integral can be evaluated by inspection. One knows that for positive $t > 0$,

$$\int d\omega \exp[-i\omega t] U^-(\omega) = 0 , \tag{208}$$

and that any function whose behavior for large ω is $1/i\omega$ has a step function discontinuity at the origin. Therefore, Eqs. (207) and (205a) become

$$u_f = U_N Q_0 Q^-(\infty)/Q^-(0) . \tag{209}$$

Since from Eq. (201) it follows that $Q(\infty) = 1$, one sees from Eq. (203) that

$$Q^-(\infty) = Q^+(\infty) = 1 . \tag{210}$$

As a result, one has from Eq. (209) and the definition of Δ given in Eq. (178) that

$$\Delta = Q^-(0)/\sqrt{Q_0} . \tag{211}$$

To make this result more explicit, use Eq. (203) and the fact that $Q(-\omega) = \bar{Q}(\omega)$ to write

$$Q^-(0) = \exp\left[\int \frac{d\omega'}{2\pi}\frac{1}{2}\left[\frac{\ln Q(\omega')}{\varepsilon - i\omega'} + \frac{\ln Q(-\omega')}{\varepsilon + i\omega'}\right]\right] \tag{212}$$

$$= \exp\left[\int \frac{d\omega'}{2\pi}\left[\frac{1}{-2i\omega'}\ln\left\{\frac{Q(\omega')}{\bar{Q}(\omega')}\right\} + \frac{\varepsilon}{\varepsilon^2 + \omega'^2}\ln Q(0)\right]\right]$$

$$\Rightarrow Q^-(0) = \sqrt{Q_0}\exp\left[-\int \frac{d\omega'}{2\pi}\frac{1}{2i\omega'}\ln\left\{\frac{Q(\omega')}{\bar{Q}(\omega')}\right\}\right] . \tag{213}$$

Placing Eq. (213) into Eq. (211) gives

$$\Delta = \exp\left[-\int \frac{d\omega'}{2\pi}\frac{1}{2i\omega'}\ln\left\{\frac{Q(\omega')}{\bar{Q}(\omega')}\right\}\right] . \tag{214}$$

In order to record a final expression that is correct not only for the Mode III model considered here, but for more general cases, rewrite Eq. (214) as

$$\Delta = C\exp\left[-\int \frac{d\omega'}{2\pi}\frac{1}{2i\omega'}\{\ln Q(\omega') - \overline{\ln Q(\omega')}\}\right] , \tag{215}$$

where C is a constant of order unity that is determined by the geometry of the lattice, equaling 1 for the triangular lattice loaded in Mode III, but $2/\sqrt{3}$ for a triangular lattice loaded in Mode I [120]. When written in this form, Eq. (215) is suitable for numerical evaluation, since there is no uncertainty relating to the phase of the logarithm.

When b becomes sufficiently small, Q is real for real ω except in the small neighborhood of isolated roots and poles that sit near the real ω-axis. Let r_i^+ be the roots of Q with negative imaginary part (since they belong with Q^+), r_i^- the roots of Q with positive imaginary part, and similarly $p_i^\pm$ the poles of Q. Then one can rewrite Eq. (215) as

$$\Delta = C\sqrt{\prod r_i^- p_i^+ / r_i^+ p_i^-}, \quad \text{for } b \to 0 . \tag{216}$$

One may derive Eq. (216) as follows: away from a root or pole of Q, the integrand of Eq. (215) vanishes. Consider the neighborhood of a root r^+ of Q which falls to the real axis from the negative side as $b \to 0$. For the sake of argument, take the imaginary part of this root to be $-ib$. In the neighborhood of this root, say within a distance $\sqrt{b}$, the integral to compute for Eq. (215) is

$$-\frac{1}{2\pi} \int_{r^+ - \sqrt{b}}^{r^+ + \sqrt{b}} \frac{d\omega'}{2i\omega'} \left[\begin{array}{c} \ln(\omega' - (r^+ - ib)) \\ -\ln(\omega' - (r^+ + ib)) \end{array} \right] . \tag{217}$$

Defining $\omega'' = \omega' - r^+$, and integrating by parts gives

$$-\frac{1}{2\pi} \int_{-\sqrt{b}}^{\sqrt{b}} \frac{d\omega''}{2i} \ln[\omega'' + r^+] \frac{2ib}{\omega''^2 + b^2} \tag{218}$$

$$= -\tfrac{1}{2} \ln r^+ + \mathcal{O}\sqrt{b} . \tag{219}$$

Similar integrals over other roots and poles of Q finally produce Eq. (216).

Together with Eq. (205), Eqs. (215) and (216) constitute the formal solution of the model. Since Q is a function of the steady-state velocity v, Eq. (214) relates the external driving force on the system, Δ, to the velocity of the crack v. The results of a calculation appear in Fig. 42.

6.4.7. Phonon emission

Right at $\Delta = 1$ just enough energy is stored to the right of the crack tip to break all bonds along the crack line. However, all steady states occur for $\Delta > 1$, so not all energy stored to the right of the crack tip ends up devoted to snapping bonds. The fate of the remaining energy depends upon the amount of dissipation b, and the distance from the crack tip one inspects. In the limit of vanishing dissipation b, traveling waves leave the crack tip and carry energy off in its wake; the amount of energy they contain becomes independent of b. Such a state is depicted in Figs. 43 and 44, which shows a solution of Eq. (205) for $v = 0.5$, $N = 9$, and $b = 0.01$. For all nonzero b, these traveling waves will eventually decay, and the extra energy will have been absorbed by dissipation, but the value of b determines whether one views the process as microscopic or macroscopic.

The frequencies of the radiation emitted by the crack have a simple physical interpretation as Cherenkov radiation. Consider the motion of a particle through a lattice, in which the phonons are described by the dispersion
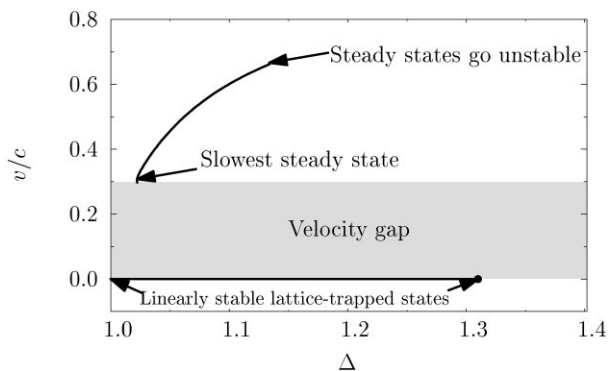
$$\omega_\alpha(\boldsymbol{k}) . \tag{220}$$

Fig. 42. The velocity of a crack v/c, scaled by the sound speed $c = \sqrt{3}/2$, is plotted as a function of the driving force Δ. The calculation is carried out using Eq. (216) for $N = 9$.

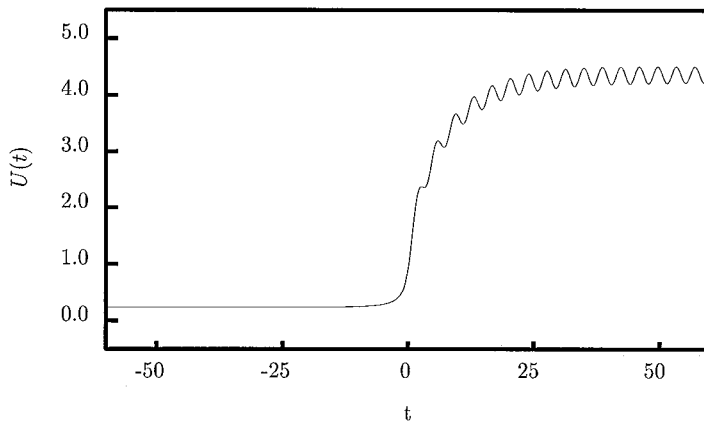Fig. 43. A plot of $U(t)$ for $v = 0.5$, $N = 9$, and $b = 0.01$, produced by direct evaluation of Eq. (205). Note that mass points are nearly motionless until just before the crack arrives, and that they oscillate afterwards for a time on the order of $1/b$.
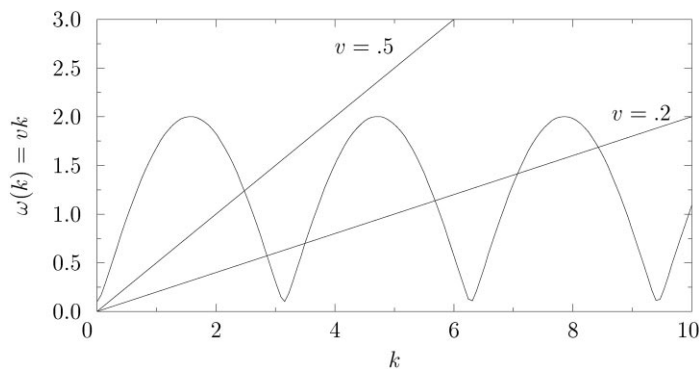

Fig. 44. Graphical solution of Eq. (223), showing that for low velocities, a large number of resonances may be excited by a moving crack.

If the particle moves with constant velocity v, and interacts with the various ions according to some function $\mathscr{I}$, then to linear order the motions of the ions can be described by a matrix D which describes their interactions with each other as

$$\ddot{u}_\mu^l = -\sum_{vl'} D_{\mu v}(\boldsymbol{R}^l - \boldsymbol{R}^{l'})u_v^{l'} + \sum_{l'} \mathscr{I}_\mu(\boldsymbol{R}^{l'} - \boldsymbol{v}t) . \tag{221}$$

Multiplying everywhere by $e^{i\boldsymbol{k}\cdot\boldsymbol{R}^l}$, summing over l, letting $\boldsymbol{K}$ be reciprocal lattice vectors, and letting Ω be the volume of a unit cell gives

$$m\ddot{u}_\mu(\boldsymbol{k}) = \sum_v D_{\mu v}(\boldsymbol{k})u_v(\boldsymbol{k}) + \frac{1}{\Omega}\sum_{\boldsymbol{K}} e^{i\boldsymbol{v}\cdot(\boldsymbol{k}+\boldsymbol{K})t}\mathscr{I}_\mu(\boldsymbol{k}+\boldsymbol{K}) . \tag{222}$$

Inspection shows that the lattice frequencies excited in this way are those which in the extended zone scheme [154] obey

$$\omega(\boldsymbol{k}) = \boldsymbol{v}\cdot\boldsymbol{k} . \tag{223}$$

Pretending that the crack is a particle, one can use Eq. (223) to predict the phonons that the crack emits.

There is another version of this argument that is both simpler and more general. The only way to transport radiation far from a crack tip is in traveling waves. However, in steady state, the traveling waves must obey symmetry (179a). In a general crystal with lattice vectors $\boldsymbol{R}$ and primitive vectors $\boldsymbol{a}$, applying this requirement to a traveling wave $\exp[i\boldsymbol{k}\cdot\boldsymbol{R} - i\omega t]$ gives

$$e^{[i\boldsymbol{k}\cdot(\boldsymbol{R}+n\boldsymbol{a}) - i\omega(\boldsymbol{k})(t+n\boldsymbol{a}/v)]} = e^{[i\boldsymbol{k}\cdot\boldsymbol{R} - i\omega(\boldsymbol{k})t]} . \tag{224}$$

Assuming $\boldsymbol{a}$ and $\boldsymbol{v}$ are parallel, Eq. (223) results again.

There are two phonon dispersion relations to consider. One gives the conditions for propagating radiation far behind the crack tip, and the other gives the conditions for propagating radiation far ahead of the crack tip. Far behind the crack tip, all the bonds are broken. Finding waves that can travel in this case is the same as repeating the calculation that led to Eq. (198), but with U^- set to zero, since all bonds are broken, and with $U_N = 0$, since phonons can propagate without any driving term. Examining Eq. (198), one sees that the condition for surface phonons to propagate far behind the crack tip is $F(\omega) = 0$. Similarly, far ahead of the crack tip no bonds are broken U^- should be set equal to U, and the condition for phonons is $F(\omega) - 2\cos^2\omega/4v = 0$. According to Eq. (201), the roots and poles of $Q(\omega)$ are therefore the phonon frequencies behind and ahead of the crack, and these are the quantities appearing in Eq. (216). We do not know if Eq. (216) is more than approximately correct for particle interactions more general than ideally brittle bonds.

6.4.8. Forbidden velocities

After making sure that bonds along the crack line break when they are supposed to, it is necessary to verify that they have not been stretched enough to break earlier. That is, not only must the bond between u_{0+} and u_{0-} reach length $2u_f$ at $t = 0$, but this must be the first time at which that bond stretches to a length greater than $2u_f$. For $0 < v < 0.3\ldots$ (the precise value of the upper limit varies with b and N) that condition is violated. The states have the unphysical character shown in Fig. 45. Masses rise above height u_f for t less than 0, the bond connecting them to the lower line of masses remaining however intact, and then they descend, whereupon the bond snaps.

Since the solution of Eq. (182) is unique, but does not in this case solve Eq. (169a), no solutions of Eq. (169a) exist at all at these velocities. Once the crack velocity has dropped below a lower critical value, all steady states one tries to compute have this character. This argument shows that no steady state in the sense of Eq. (179a) can exist. It is also possible to look analytically for solutions that are periodic, but travel two lattice spacings before repeating. No solutions of this type have yet been found. Numerically, one can verify that if a crack is allowed to propagate with Δ right above the critical threshold, and Δ is then very slowly lowered through the threshold, the crack stops propagating. It does not slow down noticeably; suddenly the moving crack emits a burst of radiation that carries off its kinetic energy, and stops in the space of an atom. That is why Fig. 45 shows a velocity gap.

6.4.9. Nonlinear instabilities

It was assumed in the calculations predicting steady states that the only bonds which break are those which lie on the crack path. From the numerical solutions of Eq. (205), one can test this assumption; it fails above a critical value of Δ. The sound speed c equals $\sqrt{3}/2$, and velocities will be scaled by this value. For $N = 9$, at a velocity of $v_c/c = 0.666 \ldots$, $\Delta_c = 1.158 \ldots$, the bond between $u(0,1/2)$ and $u(1,1/2)$ reaches a distance of $2u_f$ some short time after the bond between $u(0,1/2)$ and $u(0, -1/2)$ snaps. The steady-state solutions strained with larger values of Δ are inconsistent; only dynamical solutions more complicated than steady states, involving the breaking of bonds off the crack path, are possible. To investigate these states, one must return to Eq. (169) and numerically
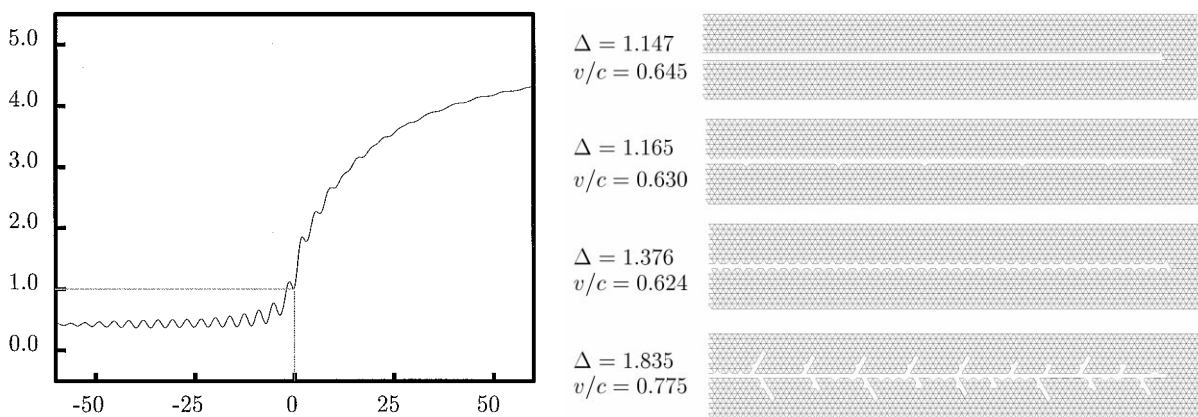

Fig. 45. Behavior of $U(t)$ for $v = 0.2$, $b = 0.05$, and $N = 9$. Notice that at $t = 0$, indicated by the dashed line, u is decreasing, and that it had already reached height 1 earlier. This state is not physical.

Fig. 46. Pictures of broken bonds left behind the crack tip at four different values of Δ. The top figure shows the simple pattern of bonds broken by a steady-state crack. At a value of Δ slightly above the critical one where horizontal bonds occasionally snap, the pattern is periodic. All velocities are measured relative to the sound speed $c = \sqrt{3}/2$. Notice that the average velocity can decrease relative to the steady state, although the external strain has increased. As the strain Δ increases further, other periodic states can be found, and finally states with complicated spatial structure. The simulations are carried out in a strip with half-width $N = 9$, of length 200 and $b = 0.01$. The front and back ends of the strip have short energy-absorbing regions to damp traveling waves. The simulation was performed by adding unbroken material to the front and lopping it off the back as the crack advanced.

solve the model directly. These simulations have been carried out [149,155] and some results are contained in Fig. 46.

The diagram shows patterns of broken bonds left behind the crack tip. Just above the threshold at which horizontal bonds begin to break, one expects the distance between these extra broken bonds to diverge. The reason is that breaking a horizontal bond takes energy from the crack and slows it below the critical value. The crack then tries once more to reach the steady state, and only in the last stages of the approach does another horizontal bond snap, beginning the process again. This scenario for instability is similar to that known as intermittency in the general framework of nonlinear dynamics [156]; the system spends most of its time trying to reach a fixed point which the motion of a control parameter has caused to disappear.

Here is a rough estimate of the distance between broken horizontal bonds. Let $u_h(t)$ be the length of an endangered horizontal bond as a function of time. Actually, one needs to view matters in a reference frame moving with the crack tip, so every time interval $1/v$, one shifts attention to a bond one lattice spacing to the right. When Δ is only slightly greater than Δ_c, the length of such a bond viewed in a moving frame should behave before it snaps, as

$$u_h \sim 2u_f + (\partial u_h/\partial \Delta)(\Delta - \Delta_c) - \delta u e^{-bt} . \tag{225}$$

Here $\partial u_h/\partial \Delta$ means that one should calculate the rate at which the steady-state length of u_h would change with Δ if this bond were *not* allowed to snap, and δu describes how much smaller than its steady-state value the bond ends up after the snapping event occurs. Ref. [120] shows that deviations from steady states die away at long times as $\exp[-bt]$. From this expression, one can estimate the time between snapping events by setting u_h to $2u_f$ and solving Eq. (225) for t. The result is that the frequency v with which horizontal bonds snap should scale above the critical strain Δ_c as

$$v \sim -b/\ln\left(\frac{1}{\delta u}\frac{\partial u_h}{\partial \Delta}[\Delta - \Delta_c]\right), \tag{226}$$

a result that is consistent with the numerics, but hard to check conclusively. One can calculate numerically that $\partial u_h/\partial \Delta = 5.5$ for the conditions of Fig. 46, but δu is hard to find independently. Assuming that Eq. (226) is correct, one finds from the second picture of Fig. 46 that $\delta u = 0.04$. Further increasing the external strain Δ makes a wide variety of complicated behavior possible, including dendritic patterns, in the lowest panel of Fig. 46 that are reminiscent of experiment.

6.4.10. The connection to the Yoffe instability

The basic reason for the branching instability seen above is the crystal analog of the Yoffe instability, working itself out on small scales. The Mode III calculation finds that the critical velocity for the instability to frustrated branching events is indeed close to the value of $0.6c_R$ predicted by Yoffe in the continuum. The critical velocity seen experimentally in amorphous materials is 1/3 of the wave speed, not 2/3. This discrepancy could be due to some combination of three factors.

1. The force law between atoms is actually much more complicated than ideal snapping bonds. Gao [157], has pointed out that the Rayleigh wave speed in the vicinity of a crack tip may be significantly lower than the value of c_R far away from the tip because material is being stretched beyond the range of validity of linear elasticity.
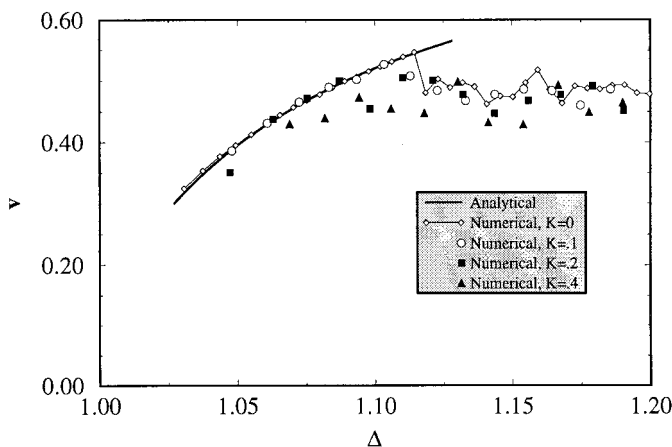
Fig. 47. The two lines, as indicated by the legend, compare analytical results for steady crack velocities in a strip 20 atoms high with simulation results in a strip 20 high and 60 wide. The symbols display the effect of random bond strengths on crack velocities. The springs all snap at the same extension, but have spring constants that vary randomly by the amounts indicated in the legend.

2. The experiments are at room temperature, while the calculations are at zero.
3. The experiments are in amorphous materials, while the calculations are in crystals.

6.5. The generality of the results in a ideal brittle crystal

It is easy to carry out numerical simulations that add various effects to the solvable model that are difficult to include analytically. For example, one can vary the interparticle potentials from the simple form given in Eq. (169b), one can make the bond strengths in the lattice vary randomly, or watch the crack propagate in a lattice maintained at nonzero temperature. A brief summary of these numerical searches would be that small changes in the basic model, Eq. (169) do not alter the qualitative conclusions obtained so far. For example, in Fig. 47, one can see the effect of making bond strengths random by varying amounts. The randomness is implemented by setting the spring constants between neighbors in Eq. (169) to $(1 + \mathscr{K}_{r_1 r_2})1/2$, where r_1 and r_2 are nearest neighbors, and $\mathscr{K}_{r_1 r_2}$ is a random variable ranging with uniform probability from $-K$ to K. The springs still snap at the extension of $2u_f$. The qualitative changes introduced by the randomness are that it becomes possible for the crack to jump up or down by a lattice spacing, as shown in Fig. 48, and it also becomes possible for the crack tip to encounter a particularly tough bond, and arrest prematurely. Fig. 47 was produced by obtaining a moving crack at $\Delta = 1.2$, and then very slowly ramping Δ down to 1, with velocities calculated by measuring the time needed for the crack to progress 20 lattice spacings. The fluctuations visible in Fig. 47 are to be understood as resulting from this procedure; if enough averaging were carried out, no fluctuations in velocity would be visible despite the presence of randomness.

We have also carried out studies of the effect of temperature. We later found in molecular dynamics simulations that three-dimensional calculations are quite different from two-dimensional ones, so we will not present the results here. There is a qualitative difference between static
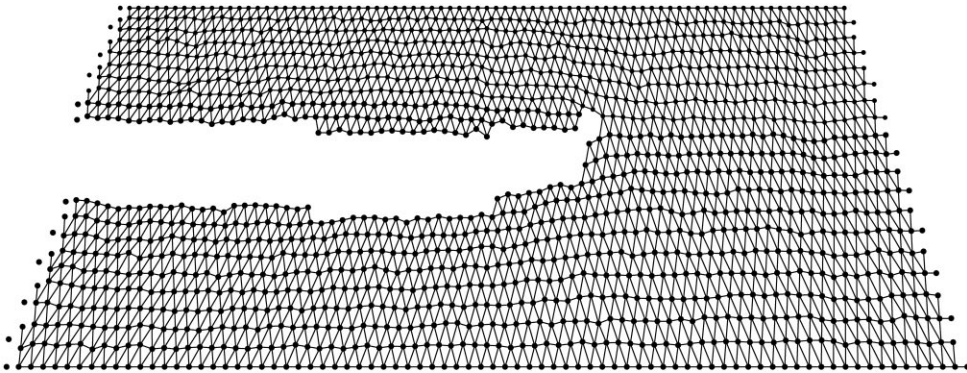
Fig. 48. In the presence of randomness, cracks no longer travel along straight-line paths. This simulation is carried out with $K = 0.2$, for a strip 20 atoms high and 80 long

randomness and thermal fluctuations that is quite important for fracture. If a crack encounters a tough spot in a material, it can halt and sit there forever. Thermal fluctuations might halt a crack temporarily, but are just as likely to take a static crack and give it energy to start moving. Lattice-trapped cracks are not completely static in the presence of thermal fluctuations; they creep ahead with some probability [158]. When the rate of creep rises to speeds on the order of the sound speed, the distinction between creeping and running cracks vanishes, and the velocity gap vanishes.

The robustness of the branching phenomena described in this model was further illustrated by recent numerical studies of Eq. (167) in the nonlinear regime, where micro-branches are observed. Hieno and Kaski [159] have investigated some effects of changing the model parameters governing Mode I fracture. A number of features similar to those observed in the experiments on amorphous materials were observed. Disorder of the perfect crystal lattice, for example, was introduced by imposing a random distribution of the local values of Young's moduli. The effect of the disorder was to disrupt the periodicity of the frustrated branching events, and thus broaden the otherwise sharp branching frequency spectrum. Additional numerical work in this model by Astrom and Timonen [160] observed power-law dependence of the micro-branch trajectories with the same 0.7 power observed in experiments in both PMMA and glass.

6.6. Molecular dynamics simulations

The fracture of brittle solids is a physical process which naturally connects large and small scales [7,8]. Stresses and strains which cause the fracture are applied on macroscopic scales, while the end result is the severing of bonds on an atomic scale. Therefore, it seems reasonable to assume that computer simulations of the fracture process that account for phenomena at the atomic level must be very large. Several such simulations are now being carried out, in systems involving as many as hundreds of millions of atoms [161–163].

6.6.1. Scalable molecular dynamics simulations

However, the goal in computer simulation should not be to build the largest simulation possible, but to build the smallest one capable of answering specific physical questions. Many features of

brittle fracture may profitably be studied in simulations that are comparatively small, involving only thousands of atoms. The essential problem facing the simulations is one of length and time scales. We are now in the midst of carrying out fracture experiments in silicon. The samples are several centimeters long, several high, a millimeter thick and contain about 10^{22} atoms. The duration of an experiment is around $50\,\mu s$. The largest simulations now being performed follow 10^8 atoms for around 10^{-9} s. Direct atomic simulation of our samples therefore requires a 10^{18}-fold increase in computer power over what we now have.

How then is comparison to be performed? A first thought is to merge atomistic and continuum simulations. Use atoms in the vicinity of the crack tip, and continuum elasticity everywhere else. This approach has the potential to solve the problem of length scales, but not the problem of time scales. We describe below what we believe to be a more elegant approach to the problem that takes care of length and time scales at once.

The basic idea is to make greatest possible use of the conceptual framework of fracture mechanics. Fracture mechanics allows the entire crack problem to be followed in the context of continuum mechanics if only one is supplied with a relationship between the fracture energy, Γ, and the velocity, v. The goal is therefore to obtain this relationship from an atomic simulation that is absolutely as small as possible. The results can then be employed as input to continuum simulations making all the macroscopic predictions desired. The analytical results of Sections 2 and 6.3 provide tremendous help in designing these simulations. The first suggestion of the theoretical framework is that one look for steady states: configurations obeying Eq. (179a). Since states of this sort repeat indefinitely, observation over finite time allows one to make predictions for an infinite time, solving the time scaling problem. The only question to be settled is how long it takes a numerical simulation to pass through transients and reach the steady state. In a strip of height L this time is proportional to the time needed for sound to travel from the crack tip to the top of the system and return. In practice, steady states establish themselves fully after about 100 such transit times. The taller a strip becomes, the longer this time, so one wants a strip that is as narrow as possible.

The analytical work is particularly useful in establishing the minimum height of a strip. Fig. 40 shows the relation between v and Δ for strips of height 80 and 160. Above a height of 50, the curves become almost indistinguishable. The differences are certainly not measurable in experiment. We conclude that for ideal brittle fracture in steady state, the relationship between v and Δ may be established in a strip 50 atoms high. We have performed our molecular dynamic simulation runs in strips 200 atoms high and 50 atoms high to make sure the results do not change. The number of atoms in the simulations ranges between 100 000 and 200 000.

In order to keep the simulation running for the times needed to achieve steady states, we put it on a conveyor belt [151]. Whenever the crack approaches within a certain distance (typically $100\,\text{Å}$) of the right end, we glue a slab of new unbroken material to that end, and chop an equal amount off the back. Finding the length needed in the x direction to obtain satisfactory results has been a matter of numerical trial and error: a total system length of $500\,\text{Å}$ makes the results independent of length. The final test consists in obtaining a steady state. The three dimensional system has spontaneously adopted a dynamical state with the periodicity of a unit cell (flat front) along the z direction, obeying the symmetry Eq. (179a) where the behavior of atoms near the top is independent of the length of the system along x, and the relationship between v and Δ is

independent of the height of the strip. Therefore, this steady state provides one point on the curves relating v and Δ, which we believe to be correct in the limit of infinite size systems and long times.

The particular solid on which we have focused so far for our numerical studies is silicon. The reason for this choice is that silicon single crystals with a variety of orientations are inexpensive, thus making numerical predictions amenable to experimental verification. Silicon is very brittle, the crystal structure is well known, and considerable effort has been expended in developing classical three-body potentials suitable for use in molecular dynamics. We employ Stillinger–Weber potentials, with a modified version of the three-body term, but keep an open mind as to whether some other potential might provide better results. Indeed, given the severely non-equilibrium nature of fracture, it is possible that no classical potentials provide a realistic account, and in view of the emission of electrons and light that is observed in the vicinity of the crack tip, it is entirely possible that density functional theory could fail as well. Only a detailed and patient comparison of theory and experiment, which has not yet been performed, will be able to settle such doubts.

Two additional points concerning the simulations:

1. In steady state, the energy consumed by the crack per unit length must equal the energy stored per unit length to the left. This claim remains true even for strains large enough that applicability of linear elasticity could be called into question. This claim relies on symmetry rather than the matched asymptotics of fracture mechanics.
2. The simulation contains a complete description of the process zone. As more energy is fed to the crack tip, as temperature increases, or as one moves to inhomogeneous or ductile materials, the size of the process zone increases, and the simulation size will have to increase accordingly. We do not expect molecular dynamics to provide easy predictions for materials where the process zone is on the order of microns, let alone millimeters. The amorphous polymers on which our experiments have focused provide a particularly great challenge.

6.6.2. Sample results in silicon

Simple predictions for the zero-temperature fracture of silicon on the (111) plane in the (110) direction appear in Fig. 49. Not only is there a velocity gap of 1500 m/s but there are also plateaus and hysteretic loops that are essentially unexplained. It is natural to wonder how much of this intricate structure should be preserved at room temperature. We have therefore performed simulations focusing on the first hysteresis loop at temperatures between 0 and 300 K. An interesting result of these simulations is that lattice trapping is predicted to *disappear* at a temperature of 150 K, and experiments will have to proceed to temperatures lower than this to see it. Although this result was obtained in silicon, it implies an explanation for why no lattice trapping has yet been observed experimentally in either crystalline or amorphous materials.

Cracks at zero temperature display a clear dynamic instability at a critical energy flux corresponding to $\Delta = 2$. Up until this point, phonons are able to carry away all excess energy. This instability does not take the form of a simple micro-branching instability, partly because bonds can easily rejoin above the main crack line in a single component solid with no environmental impurities available. Instabilities at room temperature have not yet been explored either numerically or analytically.
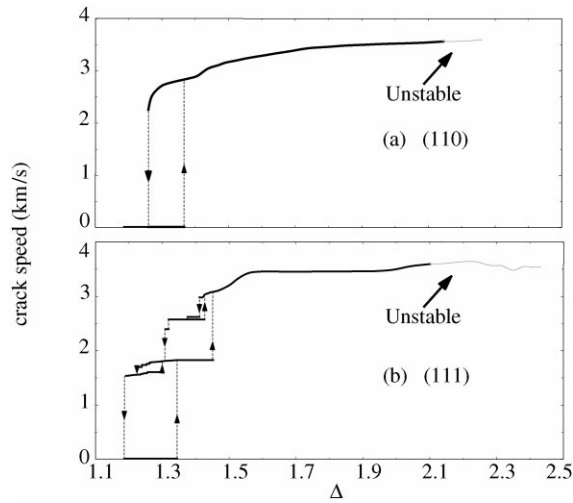
Fig. 49. Steady state crack velocities in silicon as a function of the dimensionless loading parameter Δ for fracture along (111) and (110) planes [151].

6.6.3. Large size molecular dynamic simulations

A number of very large-scale molecular dynamic simulations of dynamic fracture have been performed [161–164]. The first of these is the work by Abraham et al. where the dynamics of a crack were investigated within a 10^6 atom crystal, where the atoms are attached via a Lennard Jones 6–12 potential. Stress was applied to the system by displacing opposing boundaries of the system at a strain rate that is approximately equivalent to that obtained in explosive loading applied to crack faces. These conditions were necessary to achieve sufficient acceleration of the crack tip so as to achieve high enough crack velocities over the duration of the simulation to be able to detect the existence of instabilities of the crack's motion. The results of these simulations were surprisingly close to experimental observations in amorphous materials. The crack was observed to accelerate smoothly until reaching a velocity of $0.32c_R$. At velocities beyond this the instantaneous velocity of the crack tip was observed to become erratic, as large velocity fluctuations occurred. These fluctuations were coupled with a "zig-zag" motion of the crack tip, which formed in its wake a rough fracture surface. These interesting simulations highlight the robust and general nature of the instability.

The robust nature of the instability was further highlighted by the work of Zhou et al. [165] where crack propagation was investigated in a 400 000 atom crystal where the atoms were coupled via a Morse potential. By varying the applied strain rates the maximal velocity that a crack could achieve over the duration of a simulation was varied between 0.18 and $0.36c_R$, where the strain rates used corresponded, as in the Abraham et al. work, to explosive loading of the system. At a velocity of $0.36c_R$, instability of the crack was observed to occur by branching of the crack. The branching process was seen to be immediately preceded by the nucleation of a dislocation in the crystal together with a build up of the phonon field in the vicinity of the crack tip.

In both of the above large-scale simulations, the entire fracture process (from initiation to the instability onset) occurred over a time corresponding to approximately 1 ns. For this reason both

the strain rates used and the amount of strain in the material at the onset of fracture (approximately an order of magnitude larger than observed in real materials) had to be extremely large. Thus, the close correspondence of the results of the simulations with the laboratory results obtained in amorphous materials is rather surprising. The short time scales used in these simulations, of course, preclude examination of steady-state properties of the system. It should therefore be interesting to compare the results obtained in these experiments with steady-state results obtainable in the smaller simulations described in Section 6.6.1.

7. Conclusions

We began working in the field of fracture with the misconception that there was a problem with the terminal velocity of cracks needing to be explained. Gradually, we came to understand that the difficulty in explaining the terminal velocity of cracks had been so persistent because the problem had not been properly posed. The real question concerned the nature of dissipation near the crack tip.

In a sufficiently brittle material, it is surprising to need to consider dissipation. It seems natural to suppose that energy will mainly be consumed by the act of snapping bonds to create new surface, and that this process should depend only weakly upon crack velocity. It should have been obvious all along that this view cannot be correct. By loading cracks in differing fashions, greatly varying quantities of energy can be forced into the crack tip. The tip must find some mechanism for dealing with the energy not needed to break a minimal set of bonds, and once transfer into phonons and other tame mechanisms has been exhausted, the crack tip begins a sequence of dynamical instabilities, designed to digest energy by creating ramified networks of broken surface on small scales.

These ideas offer a detailed account of aspects of fracture that had been considered too complicated to describe quantitatively, or were simply ignored. There is no conflict with conventional fracture mechanics. One of the basic tenets of fracture mechanics is that if the system of interest is sufficiently large that the assumption of small-scale yielding is justified, all of the complex dissipative processes that go into creating a new fracture surface can be thrown together into a phenomenological function of velocity called the fracture energy. In large enough systems, the crack tip instabilities occur within the process zone, where the descriptive power of linear elastic fracture mechanics does not operate. Thus, from the viewpoint of conventional fracture mechanics, the instabilities simply redefine the value of Γ. On the other hand, without fundamental understanding of the structure of the process zone that yields Γ, the theory loses both its descriptive as well as its predictive power.

We have now achieved a good understanding of the structure and dynamics of mechanisms for dissipation within the near vicinity of the tip of a moving crack in a brittle material. We find that fracture in brittle materials is governed by a dynamic instability which leads to repeated attempted branching of the crack. The major features of this instability are summarized below.

1. There seems to be no material so brittle that the process zone always remains featureless. Once energy flux to the tip of a crack exceeds the maximum value that can safely be transported away by phonons or other dissipative mechanisms, the tip undergoes a progression of instabilities.

2. Beyond the instability threshold, an initial propagating crack changes its topology by creating short-lived microscopic crack branches. The micro-branching process give rise to oscillations of the velocity of the leading crack. In addition, the branching process forms the non-trivial surface structure that is observed on the fracture surface of amorphous materials.

3. Once the micro-branching instability occurs, the amount of energy dissipated by the system increases by an amount that is simply the total length formed by the micro-branches and main crack times the fracture energy of a single crack. Experimentally, this can increase the total crack length (and with it the dissipation) by up to an order of magnitude.

4. The mean length of the frustrated branches increases as a function of the energy flux into the crack. Eventually, the micro-branches evolve into macroscopic crack branches. The onset of the micro-branching instability therefore provides a well-defined criterion for the process that eventually culminates in macroscopic crack branching. There is evidence that a second transition may occur at velocities larger than v_c where the width of the micro-branches appears to diverge. This transition may be a sufficient condition for macroscopic crack branching to occur.

5. In crystalline materials, theory can account for the instability in some detail, and makes the added prediction that a forbidden band of velocities exists for cracks. A crack may only propagate stably above a finite minimum velocity. Molecular dynamics simulations of crystalline silicon indicate that this forbidden band of states may disappear by room temperature, but should be observable in low temperature experiments.

Thus the picture is still incomplete. The most detailed experiments are in amorphous materials at room temperature, while the most detailed theory applies only to crystals at very low temperatures. A theoretical description of fracture general enough to encompass the full range of brittle materials, or even to provide a precise description of what "brittle" means has not yet been obtained. Attempts to describe the process zone within some sort of continuum framework have not yet been successful, but the limitations in the atomic point of view provide ample motivation for continued effort along the continuum line.

Although the instability appears in dynamic finite element simulations, it has no analytical explanation in a continuum framework. In fact, many classical models of the process (cohesive) zone have been shown to be ill-posed in that they admit a continuum of possible states under identical conditions. Theories formulated on a lattice, on the other hand, do not exhibit these difficulties. It remains to be seen whether a simple continuum limit exists, or whether a crucial ingredient in understanding fracture is the discreteness of the underlying atoms.

References

[1] T.L. Anderson, Fracture Mechanics: Fundamentals and Applications, CRC Press, Boca Raton, FL, 1991.
[2] H.L. Ewalds, R.J.H. Wanhill, Fracture Mechanics, Edward Arnold, London, 1984.
[3] D. Broek, Elementary Engineering Fracture Mechanics, 2nd ed., Sijthoff and Noorhoff, Alphen aan den Rijn, 1978.
[4] J.F. Knott, Fundamentals of Fracture Mechanics, Butterworth, London, 1973.
[5] G.P. Cherepanov, Mechanics of Brittle Fracture, McGraw-Hill, New York, 1979.
[6] J.G. Williams, Fracture Mechanics of Polymers, Wiley, New York, 1984.
[7] L.B. Freund, Dynamic Fracture Mechanics, Cambridge University Press, Cambridge, 1990.

[8] M.F. Kanninen, C. Popelar, Advanced Fracture Mechanics, Oxford, New York, 1985.

[9] D. Broek The Practical Use of Fracture Mechanics, 3rd ed., Kluwer Academic Press, Dordrecht, 1994.

[10] R. Thomson, The Physics of fracture, Solid State Phys 39 (1986) 1–29.

[11] F.A McClintock, G.R. Irwin, Plasticity aspects of fracture mechanics, Symp. on Fracture Toughness Testing and its Applications, Special Technical Publication, vol. 381, American Society for Testing and Materials, 1965, pp. 84–113.

[12] B.L. Averbach, Some physical aspects of fracture, in: Fracture, an Advanced Treatise, vol. I, Academic Press, New York, 1968, pp. 441–471.

[13] I.S. Grigoriev, E.Z. Meilkhov (Eds.), Handbook of Physical Quantities, CRC Press, Boca Raton, FL, 1997.

[14] N. Mott, Brittle fracture in mild steel plates, Engineering 165 (1947) 16–18.

[15] E. Dulaney, W. Brace, Velocity behavior of a growing crack, J. Appl. Phys 31 (1960) 2233–2266.

[16] A. Stroh, A theory of the fracture of metals, Philos. Mag. 6 (1957) 418–465 (Suppl.) Adv. Phys.

[17] E.H. Yoffe, The moving Griffith crack, Philos. Mag 42 (1951) 739–750.

[18] G.R. Irwin, Fracture mechanics, in: J.N. Goodier, N.J. Hoff (Eds.), Structural Mechanics, Pergamon Press, Elmsford, NY, 1960, pp. 557–591.

[19] E. Orowan, Energy criteria of fracture, Weld. Res. Supp. 34 (1955) 157–160.

[20] B. Lawn, Fracture in Brittle Solids, 2nd ed., Cambridge University Press, Cambridge, MA, 1993.

[21] B. Cotterell, J.R. Rice, Slightly curved or kinked cracks, Int. J. Fract. 14 (1980) 155.

[22] G.R. Irwin, Fracture, Handbuch der Physik, vol. 6, Springer, Berlin, 1958, pp. 551.

[23] G.R. Irwin, Analysis of stresses and strains near the end of a crack traversing a plate, J. Appl. Mech. 24 (1957) 361–364.

[24] L.D. Landau, E.M. Lifshitz, Theory of Elasticity, 3rd ed., Pergamon Press, London, 1986.

[25] T. Nakamura, D.M. Parks, Three-dimensional stress field near the crack front of a thin elastic plate, J. Appl. Mech. 55 (1988) 805–813.

[26] N.I. Muskhelishvili, Some Basic Problems in the Mathematical Theory of Elasticity, Noordhoff, Groningen, 1952.

[27] A.A. Griffith, The phenomena of rupture and flow in solids, Mech. Eng. A 221 (1920) 163–198.

[28] J.D. Eshelby, The elastic field of a crack extending nonuniformly under general anti-plane loading, J. Mech. Phys. Solids 17 (1969) 177–199.

[29] B.V. Kostrov, Unsteady propagation of longitudinal shear cracks, Appl. Math. Mech. (Translation of PMM) 30 (1966) 1077–1087.

[30] B.V. Kostrov, Crack propagation with a variable velocity, Appl. Math. Mech. (Translation of PMM) 38 (1974) 551–600.

[31] J.R. Willis Elasticity: Mathematical Methods and Applications, Ch. Accelerating cracks and related problems, Halston Press, New york, 1990, pp. 397–409.

[32] R.V. Gol'dstein, R. Salganik, Brittle fracture of solids with arbitrary cracks, Int. J. Fract. 10 (1974) 507–523.

[33] J.A. Hodgdon, J.P. Sethna, Derivation of a general three-dimensional crack-propagation law: a generalization of the principle of local symmetry, Phys. Rev. B 47 (1993) 4831–4840.

[34] A. Yuse, M. Sano, Transition between crack patterns in quenched glass plates, Nature 362 (1993) 329–331.

[35] O. Ronsin, F. Heslot, B. Perrin, Experimental study of quasistatic brittle crack propagation, Phys. Rev. Lett 75 (1995) 2252–2255.

[36] M. Marder, Instability of a crack in a heated strip, Phys. Rev. E R51 (1994) 49–52.

[37] H.A. Bahr, A. Gerbatsch, U. Bahr, H.J. Weiss, Oscillatory instability in thermal cracking: a first-order phase-transition phenomenon, Phys. Rev. E 52 (1995) 240.

[38] M. Adda-Bedia, Y. Pomeau, Crack instabilities in a heated glass strip, Phys. Rev. E 52 (1995) 4105–4113.

[39] R.C. Ball, H. Larralde, Three-dimensional stability analysis of planar straight cracks propagating quasistatically under type I loading, Int. J. Fract. 71 (1995) 365–377.

[40] H. Larralde, R.C. Balle, The shape of slowly growing cracks, Europhys. Lett. 30 (1995) 87–92.

[41] M. Ramulu, A.S. Kobayashi, Mechanics of crack curving and branching – a dynamic fracture analysis, Int. J. Fract. 27 (1985) 187–201.

[42] P.S. Theocaris, H.G. Georgiadis, Bifurcation predictions for moving cracks by the T-criterion, Int. J. Fract. 29 (1985) 181–190.

[43] M. Ramulu, A.S. Kobayashi, Strain energy density criteria for dynamic fracture and dynamic crack branching, Theoret. Appl. Fract. Mech. 5 (1986) 117–123.

[44] G.C. Sih, Some basic problems in fracture mechanics and new concepts, Eng. Fract. Mech. 5 (1973) 365–377.

[45] M. Adda-Bedia, M.B. Amar, Stability of Quasiequillibrium cracks under uniaxial loading, Phys. Rev. Lett. 76 (1996) 1497–1500.

[46] L.G. Parleton, Determination of the growth of branched cracks by numerical methods, Eng. Fract. Mech. 11 (1979) 343–358.

[47] J.F. Kalthoff, On the propagation direction of bifurcated cracks, in: G.C. Sih (Ed.), Dynamic Crack Propagation, Noordhoof, Leydon, 1972, pp. 449–458.

[48] V. Prakash, R.J. Clifton, Experimental and analytical investigation of dynamic fracture under conditions of plane strain, in: H.A. Ernst, A. Saxena, D.L. McDowell (Eds.), Fracture Mechanics: 22nd Symp., vol. 1, American Society for Testing and Materials, Philadelphia, PA, 1992, pp. 412–444.

[49] K. Ravi-Chandar, W.G. Knauss, Dynamic crack-tip stress under utress wave loading – a comparison of theory and experiment, Int. J. Fract. 20 (1982) 209–222.

[50] P. Manogg, Investigation of the rupture of a plexiglass plate by means of an optical method involving high speed filming of the shadows originating around holes drilled in the plate, Int. J. Fract. 2 (1966) 604–613.

[51] P.S. Theocaris, E.E. Gdoutos, An optical method for determining opening-mode and edge sliding-mode stress-intensity factors, J. Appl. Mech. 39 (1972) 91.

[52] J.F. Kalthoff, The shadow optical method of caustics, in: A. Lagarde (Ed.), Static and Dynamic Photoelasticity and Caustics, Springer, Berlin, 1987, pp. 407–522.

[53] A.J. Rosakis, J. Duffy, L.B. Freund, The deterimination of dynamic fracture toughness of AISI 4340 steel by the shadow spot method, J. Mech. Phys. Solids 32 (1984) 443–460.

[54] A.J. Rosakis, L.B. Freund, The effect of crack tip plasticity on the determination of dynamic stress intensity factors by the optical method of caustics, J. Appl. Mech. 48 (1981) 302–308.

[55] A.S. Kobayashi, in: A.S. Kobayashi (Ed.), Handbook on Experimental Mechanics, American Society for Testing and Materials, Prentice-Hall, Englewood Cliffs, NJ, 1987.

[56] T. Kobayashi, J.W. Dally, Dynamic photoelastic determination of the $\dot{a} - K$ relation for 4340 steel, in: Crack Arrest Methodology and Applications, American Society for Testing Materials, Philadelphia, 1979, pp. 189–210.

[57] J.W. Dally, Dynamic photoelasticity and its application to stress wave propagation, fracture mechanics, and fracture control, in: A. Lagarde (Ed.), Static and Dynamic Photoelasticity and Caustics, Springer, Berlin, 1987, pp. 247–406.

[58] E. Sharon, S.P. Gross, J. Fineberg, Local crack branching as a mechanism for instability in dynamic fracture, Phys. Rev. Lett. 74 (1995) 5146–5154.

[59] A.K. Pratt, P.L. Green, Measurement of the dynamic fracture toughness of polymethylmethacrylate by high-speed photography, Eng. Fract. Mech. 6 (1974) 71–80.

[60] H. Bergkvist, Some experiments on crack motion and arrest in polymethylmethacrylate, Eng. Fract. Mech. 6 (1974) 621–626.

[61] W. Doll, A molecular weight dependent transition in polymethymethacrylate, J. Mater. Sci. 10 (1975) 935–942.

[62] J. Congleton, B.K. Denton, ASTM-STP 627 (1977) 336–358.

[63] B. Brickstad, F. Nilsson, Numerical evaluation by FEM of crack propagation experiments, Int. J. Fract. 16 (1980) 71–84.

[64] J. Fineberg, S.P. Gross, M. Marder, H.L. Swinney, Instability in Dynamic Fracture, Phys. Rev. Lett. 67 (1991) 457–460.

[65] J. Fineberg, S.P. Gross, M. Marder, H.L. Swinney, Instability in the propagation of fast cracks, Phys. Rev. B 45 (1992) 5146–5154.

[66] F. Kerkhof, Wave fractographic investigations of brittle fracture dynamics, in: G.C. Sih (Ed.), Dynamic Crack Propagation, Noordhoff International Publishing, Leyden, 1973, pp. 3–29.

[67] W. Doll, An experimental study of the heat generated in the plastic region of a running crack in different polymeric materials, Eng. Fract. Mech. 5 (1973) 259–268.

[68] R. Weichert, K. Schonert, On the temperature at the tip of a fast running crack, J. Mech. Phys. Solids 22 (1974) 127–133.

[69] C. Zimmerman, W. Klemm, K. Schonert, Dynamic energy release rate and fracture heat in polymethylmethac-rylate (pmma) and a high strength steel, Eng. Fract. Mech. 20 (1984) 777–782.

[70] K.N.G. Fuller, P.G. Fox, J.E. Field, The temperature rise at the tip of fast-moving cracks in glassy polymers, Proc. Roy. Soc. Lond. A 341 (1975) 537–557.

[71] A.T. Zehnder, A.J. Rosakis, On the temperature distribution at the vicinity of dynamically propagating cracks in 4340 steel, J. Mech. Phys. Solids 29 (1991) 385–415.

[72] J. Kallivayalil, A.T. Zehnder, A method for thermo-mechanical analysis of steady state dynamic crack growth, Int. J. Fract. 66 (1994) 99–120.

[73] I.G. Scott, Basic Acoustic Emission, Nondestructive Testing Monographs and Tracts, vol. 6, Gordon and Breach, New York, 1991.

[74] S.P. Gross, J. Fineberg, M. Marder, W.D. McCormick, H.L. Swinney, Acoustic emissions from rapidly moving cracks, Phys. Rev. Lett. 71 (19) (1993) 3162–3165.

[75] J.T. Proctor, An improved piezoelectric acoustic emission transducer, J. Acoust. Soc. Amer 71 (1982) 1163–1168.

[76] J.F. Boudet, S. Ciliberto, V. Steinberg, Experimental study of the instability of crack propagation in brittle materials, Europhys. Lett. 30 (1995) 337–342.

[77] J.F. Boudet, S. Ciliberto, V. Steinberg, Dynamics of crack propagation in brittle materials, J. Phys. II France 6 (1996) 1493–1516.

[78] H. Kolsky, Stress Waves in Solids, Oxford, London, 1953.

[79] K.S. Kim, Dynamic fracture under normal impact loading of the crack faces, J. Appl. Mech. 52 (1985) 585–592.

[80] B.Q. Vu, V.K. Kinra, Brittle fracture of plates in tension:static field radiated by a suddenly stopping crack, Eng. Fract. Mech. 15 (1981) 107–114.

[81] A. Kobayashi, N. Ohtani, T. Sato, Phenomenological aspects of viscoelastic crack propagation, J. Appl. Poly. Sci. 18 (1974) 1625–1638.

[82] E. Sharon J. Fineberg, On massless cracks and the continuum theory of fracture, Nature (January 1999), to be published.

[83] E. Sharon, J. Fineberg, Universal features of the micro-branching instability in dynamic fracture, Philos. Mag. B 78 (1998) 243–251.

[84] J.J. Gilman, C. Knudsen, W.P. Walsh, Cleavage cracks and dislocations in LiF crystals, J. Appl. Phys. 6 (1958) 601–607.

[85] J.E. Field, Brittle fracture: its study and application, Contemp. Phys 12 (1971) 1–31.

[86] D. Hull, P. Beardmore, Velocity of propagation of cleavage cracks in tungsten, Int. J. Fract. Mech 2 (1966) 468–487.

[87] P.D. Washabaugh, W.G. Knauss, A reconciliation of dynamic crack velocity and Rayleigh wave speed in isotropic brittle solids, Int. J. Fract. 65 (1994) 97–114.

[88] W. Doll, Kinetics of crack tip craze zone before and during fracture, Polym. Eng. Sci. 24 (1984) 798–808.

[89] R.P. Kusy, D.T. Turner, Influence of the molecular weight of PMMA on fracture surface energy in notched tension, Polymer 17 (1975) 161–166.

[90] R.P. Kusy, M.J. Katz, Generalized theory of the total fracture energy for glassy organic polyers, Polymer 19 (1978) 1345–1357.

[91] D. Broek, Some contribution of electron fractography to the theory of fracture, Int. Met. Rev. 185 (1974) 135–181.

[92] V.Y. Milman, Fracture surfaces: a critical review of fractal studies and a novel morphological analysis of scanning unneling microscopy measurements, Prog. Mater. Sci. 38 (1994) 425–474.

[93] P. Daguier, B. Nghiem, E. Bouchaud, F. Creuzet, Pinning and depinning of crack fronts in heterogeneous materials, Phys. Rev. Lett 78 (1997) 1062–1064.

[94] J.W. Holloway, D.G. Johnson, Microstructure of the mist zone on glass fracture surfaces, Philos. Mag. 17 (1968) 899–910.

[95] D. Hull, Effect of Crazes on the propagation of cracks in polystyrene, J. Mater. Sci 5 (1970) 357–363.

[96] K. Ravi-Chandar, W.G. Knauss, An experimental investigation into dynamic fracture: III. On steady-state crack propagation and crack branching, Int. J. Fract 26 (1984) 141–154.

[97] J.B.C.S.R. Anthony, J.B. Chubb, J. Congleton, The crack-branching velocity, Philos. Mag 22 (1970) 1201–1216.

[98] J. Carlsson, L. Dahlberg, F. Nilsson, Experimental studies of the unstable phase of crack propagation in metals and polymers, in: G.C. Sih (Ed.), Dynamic Crack Propagation, Noordhoof, Leydon, 1972, p. 3.

[99] T. Shioya, R. Ishida, Microscopic fracture modes of brittle polymers in dynamic crack propagation, in: H.P. Rossmanith, A.J. Rosakis (Eds.), Dynamic Failure of Materials, Elsevier Applied Science, Essex, 1991, pp. 351.

[100] S. Gross, Dynamics of fast fracture, Ph.D. Thesis, University of Texas, Austin, 1995.

[101] K. Ravi-Chandar, B. Yang, On the role of microcracks in the dynamic fracture of brittle materials, J. Mech. Phys. Solids 45 (1997) 535–563.

[102] E. Sharon, J. Fineberg, Microbranching instability and the dynamic fracture of brittle materials, Phys. Rev. B 54 (10) (1996) 7128–7139.

[103] B.B. Mandelbrot, D.E. Passoja, A.J. Paullay, Fractal character of fracture surfaces of metals, Nature 308 (1984) 721–722.

[104] E. Bouchaud, G. Lapasset, J. Planès, Fractal dimension of fractured surfaces: a universal value?, Europhys. Lett. 13 (1990) 73–79.

[105] E. Bouchaud, L. de Arcangelis, G. Lapasset, J. Planès, Fractals Breakage Mater. La Recherche (Paris) 22 (1991) 808.

[106] K.J. Maloy, A. Hansen, E.L. Hinrichsen, S. Roux, Experimental measurements of the roughness of brittle cracks, Phys. Rev. Lett. 68 (1992) 213–215.

[107] P. Daguier, S. Henaux, E. Bouchaud, F. Creuzet, Quantitative analysis of a fracture surface by atomic force microscopy, Phys. Rev. E 53 (1996) 5637–5642.

[108] O. Narayan, D. Fisher, Dynamics of sliding charge-density waves in 4-ε dimensions, Phys. Rev. Lett. 68 (1992) 3615–3618.

[109] K. Ravi-Chandar, W.G. Knauss, An experimental investigation into dynamic fracture: II. Microstructural aspects, Int. J. Fract. 26 (1984) 65–80.

[110] J. Reidle, P. Gumbsch, H.F. Fischmeister, V.G. Glebovsky, V.N. Semenov, Fracture studies of tungsten single crystals, Mater. Lett. 20 (1994) 311–317.

[111] J.T. Dickenson, Fracto-emission, in: J. Summerscales (Ed.), Non-Destructive Testing of Fibre-Reinforced Plastics Composites, vol. 2, Ch. 10, Elsevier, London, 1990.

[112] J.W. Dally, Dynamic photoelastic studies of fracture, Exp. Mech. 19 (1979) 349–361.

[113] E. Sharon, S.P. Gross, J. Fineberg, Energy dissipation in dynamic fracture, Phys. Rev. Lett. 76 (12) (1996) 2117–2120.

[114] K.B. Broberg, On the behaviour of the process region at a fast running crack tip, in: K. Kawata, J. Shioiri (Eds.), High Velocity Deformation of Solids, Springer, Berlin, 1979, pp. 182–193.

[115] K. Arakawa, K. Takahashi, Branching of a fast crack in polymers, Int. J. Fract. 48 (1991) 245–254.

[116] J.D. Eshelby, Fracture mechanics, Sci. Prog. 59 (1971) 161–179.

[117] H. Schardin, Velocity effects in fracture, in: B.L. Averbach (Ed.), Fracture, MIT Press, Cambridge, MA, 1959, pp. 297–330.

[118] B. Cotterell, Velocity effects in fracture propagation, Appl. Mater. Res. 4 (1965) 227–232.

[119] K. Ravi-Chandar, W.G. Knauss, An experimental investigation into dynamic fracture: IV. On the interaction of stress waves with propagating cracks, Int. J. Fract. 26 (1984) 189–200.

[120] M. Marder, S.P. Gross, Origin of crack tip instabilities, J. Mech. Phys. Solids 43 (1995) 1–48.

[121] J. Hauch, M. Marder, Energy balance in dynamic fracture, investigated by the potential drop technique, Int. J. Fract. (1999), to be published.

[122] J. Fineberg, S.P. Gross, E. Sharon, Micro-branching as an instability in dynamic fracture, in: J.R. Willis (Ed.), Nonlinear Analysis of Fracture, Kluwer Academic, Dordrecht, 1997, pp. 177–189.

[123] G.R. Irwin, J.W. Dally, T. Kobayashi, W.L. Fourney, M.J. Etheridge, H.P. Rossmanith, On the determination of the $\dot{a}$-K relationship for Birefringent polymers, Exp. Mech. 19 (4) (1979) 121–128.

[124] F. Lund, Elastic forces that do no work and the dynamics of fast cracks, Phys. Rev. Lett. 76 (1996) 2742–2745.

[125] G.I. Barenblatt, The formation of equilibrium cracks during brittle fracture: general ideas and hypothesis, axially symmetric cracks, Appl. Math. Mech. (Translation of PMM) 23 (1959) 622–636.

[126] G.I. Barenblatt, Concerning equilibrium cracks forming during brittle fracture: the stability of isolated cracks, relationship with energetic theories, Appl. Math. Mech. (Translation of PMM) 23 (1959) 622–636.

[127] D.C. Dugdale, Yielding of steel sheets containing slits, J. Mech. Phys. Solids 8 (1960) 100–104.
[128] E. Johnson, Process region changes for rapidly propagating cracks, Int. J. Fract. 55 (1992) 47–63.
[129] X.P. Xu, A. Needleman, Numerical simulations of fast crack growth in brittle solids, J. Mech. Phys. Solids 42 (1994) 1397–1434.
[130] J.R. Rice, Y. Ben-Zion, K.S. Kim, Three dimensional perturbation solution for a dynamic planar crack moving unsteadily in a model elastic solid, J. Mech. Phys. Solids 42 (1994) 813–843.
[131] G. Perrin, J.R. Rice, Disordering of a dynamic planar crack in a model elastic medium of randomly variable toughness, J. Mech. Phys. Solids 42 (1994) 1047–1064.
[132] Y. Ben-Zion, J.W. Morrissey, A simple re-derivation of logarithmic disordering of a dynamic planar crack due to small random heterogeneities, J. Mech. Phys. Solids 43 (1995) 1363–1368.
[133] J.R. Willis, A.B. Mochvan, Dynamic weight functions for a moving crack. I. Mode I loading, J. Mech. Phys. Solids 43 (1995) 319–341.
[134] J.R. Willis, A.B. Mochvan, Three dimensional dynamic perturbation of a propagating crack, J. Mech. Phys. Solids 45 (1997) 591–610.
[135] S. Ramanathan, D.S. Fisher, Dynamics and instabilities of planar tensile cracks in heterogeneous media, Phys. Rev. Lett. 79 (1997) 877–880.
[136] J.W. Morrissey, J.R. Rice, 3D elastodynamics of cracking through heterogeneous solids: crack front waves and the growth of fluctuations, EOS, Trans. Amer. Geophys. Union 77 (1996) F485.
[137] J.W. Morrissey, J.R. Rice, Crack front waves, J. Mech. Phys. Solids 46 (1998) 467–487.
[138] M. Barber, J. Donley, J.S. Langer, Steady-state propagation of a crack in a viscoelastic strip, Phys. Rev. A 40 (1989) 366.
[139] J.S. Langer, Models of crack propagation, Phys. Rev. A 46 (1992) 3123–3131.
[140] J.S. Langer, Dynamic model of onset and propagation of fracture, Phys. Rev. Lett. 70 (1993) 3592–3594.
[141] E.S.C. Ching, Dynamic stresses at a moving crack tip in a model of fracture propagation, Phys. Rev. E 49 (1994) 3382–3388.
[142] M. Marder, New dynamical equation for cracks, Phys. Rev. Lett. 66 (1991) 2484–2487.
[143] E.S.C. Ching, J.S. Langer, H. Nakanishi, Linear stability analysis for propagating fracture, Phys. Rev. E 53 (1996) 2864–2880.
[144] E.S.C. Ching, J.S. Langer, H. Nakanishi, Dynamic instabilities in fracture, Phys. Rev. Lett. 76 (1996) 1087–1090.
[145] E.S.C. Ching, J.S. Langer, H. Nakanishi, Model study of fracture propagation-solutions of steady-state propagation and their stability, Physica A 221 (1996) 134–142.
[146] J.R. Rice, Fracture, vol. 2, Ch. 3, Academic Press, New York, 1968, pp. 191–311.
[147] J.S. Langer, A.E. Lobkovsky, Critical examination of cohesive-zone models in the theory of dynamic fracture, J. Mech. Solids 46 (1998) 1521–1556.
[148] L. Slepyan, Dynamics of a crack in a lattice, Sov. Phys. Dokl. 26 (1981) 538–540.
[149] M. Marder, X. Liu, Instability in lattice fracture, Phys. Rev. Lett. 71 (1993) 2417–2420.
[150] R. Thomson, C. Hsieh, V. Rana, Lattice trapping of fracture cracks, J. Appl. Phys. 42 (8) (1971) 3154–3160.
[151] D. Holland, M. Marder, Ideal brittle fracture of silicon studied with molecular dynamics, Phys. Rev. Lett. 80 (1998) 746–749.
[152] S.A. Kulakhmetova, V.A. Saraikin, L.I. Slepyan, Plane problem of a crack in a lattice, Mech. Solids 19 (1984) 102–108.
[153] B. Noble, Methods Based on the Wiener–Hopf Technique for the Solution of Partial Differential Equations, Pergamon, New York, 1958.
[154] N. Ashcroft, N.D. Mermin, Solid State Physics, Saunders, London, 1976.
[155] X. Liu Dynamics of fracture propagation, Ph.D. Thesis, University of Texas, Austin, 1993.
[156] P. Manneville, Dissipative Structures and Weak Turbulence, Academic Press, Boston, 1990.
[157] H. Gao, Surface roughening and branching instabilities in dynamic fracture, J. Mech. Phys. Solids 41 (1993) 457–486.
[158] M. Marder, Statistical mechanics of cracks, Phys. Rev. E 54 (1996) 3442–3454.
[159] P. Heino, K. Kaski, Mesoscopic model of crack branching, Phys. Rev. B 54 (1996) 6150–6154.
[160] J. Astrom, J. Timomen, Crack bifurcations in a strained lattice, Phys. Rev. B 54 (1996) 9585–9588.

[161] F.F. Abraham, D. Brodbeck, R.A. Rafey, W.E. Rudge, Instability dynamics of fracture: a computer simulation investigation, Phys. Rev. Lett. 73 (2) (1994) 272–275.

[162] A. Omeltchenko, J. Yu, R.K. Kalia, P. Vashishta, Crack front propagation and fracture in a graphite sheet: a molecular-dynamics study on parallel computers, Phys. Rev. Lett. 78 (1997) 2148–2151.

[163] P. Gumbsch, S.J. Zhou, B.L. Holian, Molecular dynamics investigation of dynamic crack stability, Phys. Rev. B 55 (1997) 3445–3455.

[164] B.L. Holian, R. Ravelo, Fracture simulations using large-scale molecular dynamics, Phys. Rev. B 51 (1995) 11275–11288.

[165] S.J. Zhou, P.S. Lomdahl, R. Thomson, B.L. Holian, Dynamic crack processes via molecular dynamics, Phys. Rev. Lett. 76 (1996) 2318–2321.